Controlling Light with Photon Subtraction via the Single-Photon Raman Interaction

by

Abdolreza Pasharavesh

A thesis
presented to the University of Waterloo
in fulfillment of the
thesis requirement for the degree of
Doctor of Philosophy
in
Electrical and Computer Engineering

Waterloo, Ontario, Canada, 2025

© Abdolreza Pasharavesh 2025

Examining Committee Membership

The following served on the Examining Committee for this thesis. The decision of the Examining Committee is by majority vote.

External Examiner:	Darrick Chang Professor, ICFO - Institute of Photonic Sciences, The Barcelona Institute of Science and Technology
Supervisor:	Michal Bajcsy Associate Professor, Dept. of Electrical and Computer Engineering, University of Waterloo
Internal Member:	Na Young Kim Associate Professor, Dept. of Electrical and Computer Engineering, University of Waterloo
Internal Member:	Chris Wilson Professor, Dept. of Electrical and Computer Engineering, University of Waterloo
Internal-External Member:	Thomas Jennewein Professor, Dept. of Physics and Astronomy, University of Waterloo

Author's Declaration

I hereby declare that I am the sole author of this thesis. This is a true copy of the thesis, including any required final revisions, as accepted by my examiners.

I understand that my thesis may be made electronically available to the public.

Abstract

This dissertation leverages deterministic photon subtraction based on the single-photon Raman interaction (SPRINT) to engineer multiphoton quantum fields and design quantum optical platforms for applications ranging from non-Gaussian quantum light generation to photon-number-resolving (PNR) detection and photon number splitting (PNS) attacks on quantum key distribution (QKD). The work is structured into four main parts.

In the first part (Chapter 2), we evaluate the performance of the subtraction scheme using system parameters that are technologically accessible according to the current state of the art. We analyze the photon subtraction process in a configuration where the transitions of a Λ-type emitter are selectively coupled to the stationary modes of a bimodal cavity, which are in turn coupled to distinct waveguide modes. Using the input-output formalism of quantum optics and quantum trajectory methods, we investigate single- and multi-photon transport in the system. The results indicate that success rates approaching unity are achievable with currently reported coupling rates for cold atoms trapped in crossed optical-fiber cavities as well as for solid-state platforms based on quantum dots.

In the second part (Chapter 3), we explore the capability of the photon subtraction scheme to generate non-Gaussianity in initially Gaussian input fields. Using a photon subtractor with the emitter directly coupled to a chiral waveguide, we show that for both squeezed vacuum and coherent light input pulses, the Wigner function of the output field clearly reveals its non-Gaussian character following photon subtraction. Furthermore, we propose a measurement-based scheme on the subtracted photon which can lead to conditional generation of quantum states resembling Schrodinger's kitten state directly from coherent input light with fidelities above 99%. This result is particularly noteworthy, as coherent pulses, unlike the squeezed vacuum inputs commonly used in previous studies, are readily available experimentally.

The last two parts of the dissertation explore the possibilities arising from cascading multiple photon subtractors. In the third part (Chapter 4), we investigate the operation of a PNR detector composed of a cascade of waveguide-coupled Λ-type emitters, which deterministically demultiplexes incoming photons among single-photon detectors. We present a closed-form expression for the detector's precision in the linear regime and predict how correlations generated by nonlinear photon-photon interactions influence this precision. We compare the performance of the proposed PNR detector with that of a conventional PNR scheme based on spatial demultiplexing via beamsplitters. Our results indicate that the proposed scheme can outperform conventional detectors under realistic conditions, making it a promising candidate for next-generation PNR detection.

In the fourth part (Chapter 5), we present a specialized photon subtraction scheme that enables the deterministic extraction of single photons from multiphoton states while leaving input single-photon states unaltered. The proposed device consists of a two-way cascade of two Λ-type emitters coupled via a chiral waveguide. We analyze the interaction of this system with traveling few-photon pulses of coherent light and use these results to highlight how this two-emitter extension improves the original deterministic single-photon subtraction when it comes to implementing undetectable PNS attack on a QKD channel. Finally, in Chapter 6, we demonstrate how this two-emitter approach can be extended to an n-emitter cascade, resulting in a photon subtractor that selectively extracts photons from an input light stream based on their arrival time sequence. We show that this photon subtractor enables the generation of high-fidelity and modal purity multiphoton Fock states. The application of these Fock-state pulses in optical interferometry is investigated, highlighting their potential for quantum metrology at the Heisenberg limit. These results introduce novel applications of SPRINT-based photon subtraction in areas ranging from non-Gaussian photonics, to PNR detection, QKD, and quantum metrology.

Acknowledgements

First and foremost, I would like to express my deepest gratitude to my supervisor, Professor Michal Bajcsy, for his unwavering support, insightful guidance, and continuous encouragement throughout my Ph.D. journey. I am grateful for the opportunity he gave me to explore the fascinating field of quantum information as a member of the Nanophotonics and Quantum Optics (NPQO) Lab at the Institute for Quantum Computing (IQC). His profound expertise in quantum physics and experimental optics, combined with his patient mentorship, played a pivotal role in shaping my academic development and research direction.

I would also like to extend my sincere appreciation to my group members for fostering a collaborative and intellectually stimulating environment. I am especially grateful for the many in-depth and thought-provoking scientific discussions we shared, which greatly deepened and enriched our understanding of the subject.

Finally, I would like to thank my family who have supported and encouraged me throughout my academic journey. Their belief in me has been a constant source of motivation and strength, especially during challenging times.

Dedication

This thesis is dedicated to my family for their unconditional love, support, and encouragement throughout my entire life.

List of Publications

Journal Publications and Preprints

1. Abdolreza Pasharavesh and Michal Bajcsy. "Multi-Photon Fock State Generation via Selective Single Photon Subtraction in a Cascaded Waveguide QED System." *Advanced Quantum Technologies* 8, no. 9 (2025): 2400616.

2. Abdolreza Pasharavesh and Michal Bajcsy. "Photon Transport in Bimodal Atom-Cavity Systems with Waveguide Coupling: Application to Deterministic Photon Subtraction." *Physical Review Research* 7.1 (2025): 013018.

3. Abdolreza Pasharavesh and Michal Bajcsy. "Generation of Non-Gaussian States of Light Using Deterministic Photon Subtraction." *New Journal of Physics* 26.11 (2024): 113022.

4. Abdolreza Pasharavesh and Michal Bajcsy. "Deterministic Single Photon Subtraction with a Cascade of Waveguide-Coupled Atoms." *Optics Express* 32.15 (2024): 26740–26750.

5. Abdolreza Pasharavesh, Sai Sreesh Venuturumilli, and Michal Bajcsy. "Photon-Number-Resolving Detector Based on a Cascade of Waveguide-Coupled Quantum Emitters." *arXiv:2507.09034* (2025).

Conference Publications and Presentations

1. Abdolreza Pasharavesh, Sai Sreesh Venuturumilli, and Michal Bajcsy. "Photon Number Resolution via Multi-Photon Subtraction in a Waveguide-QED Setting." *European Quantum Electronics Conference*. Optica Publishing Group, 2025.

2. Abdolreza Pasharavesh, Sai Sreesh Venuturumilli, and Michal Bajcsy. "Quantum Light Generation and Characterization via Cascaded Single-Photon Raman Interactions." *Photonics for Quantum 2025. Vol. 13563.* SPIE, 2025.

3. Abdolreza Pasharavesh, and Michal Bajcsy. "Deterministic Photon Subtraction as a Tool for Non-Classical Light Generation." *Quantum Days*, 2025.

4. Abdolreza Pasharavesh, Sai Sreesh Venuturumilli, Supratik Sarkar, and Michal Bajcsy. "Creating Non-Classical States of Light through Photon Arithmetic with Single Emitters and Atomic Ensembles." *Quantum Sensing, Imaging, and Precision Metrology III. Vol. 13392.* SPIE, 2025.

5. Abdolreza Pasharavesh, and Michal Bajcsy. "Photon Culling: A New Photon Subtraction Approach with Application to Non-Classical Light Generation." *Quantum Computing, Communication, and Simulation V. Vol. 13391.* SPIE, 2025.

6. Abdolreza Pasharavesh, and Michal Bajcsy. "Efficient Non-Classical Light Sources Based on Deterministic Photon Subtraction." *Quantum Sensing, Imaging, and Precision Metrology III. Vol. 13392.* SPIE, 2025.

7. Abdolreza Pasharavesh, and Michal Bajcsy. "Generating Schrödinger's Kitten State from Coherent Pulses via Deterministic Photon Subtraction." *Conference on Lasers and Electro-Optics/Pacific Rim, Optica Publishing Group*, 2024.

8. Abdolreza Pasharavesh, and Michal Bajcsy. "A SPRINT-Based Single Photon Subtractor for PNS Attacks on QKD." *Photonics North (PN), IEEE*, 2024.

9. Abdolreza Pasharavesh, and Michal Bajcsy. "Deterministic Single Photon Subtraction: Implementation, Characterization, and Potential Applications." *Toronto Ultracold Atom Network (TUCAN)*, 2024.

10. Abdolreza Pasharavesh, and Michal Bajcsy. "Deterministic Single-Photon Subtraction Based on Bi-Exciton Transitions of a Quantum Dot." *Photonics North (PN), IEEE*, 2022.

Table of Contents

Examining Committee ii

Author's Declaration iii

Abstract iv

Acknowledgements vi

Dedication vii

List of Publications viii

List of Figures xiii

1 Introduction 1

1.1 Single-Photon Subtraction 3

1.1.1 Probabilistic approach 3

1.1.2 Deterministic approach 5

1.2 Theoretical Background 8

1.2.1 Input-output formalism of quantum optics 8

1.2.2 SLH framework for modeling networked quantum systems 10

1.3 Research Objectives and Thesis Outline 13

2 Deterministic Photon Subtraction in a Coupled Cavity–Waveguide Setting **14**
2.1 Single-Photon Transport Analysis . . . 14
2.1.1 Modeling and formulation . . . 14
2.1.2 Results and discussion . . . 20
2.2 Numerical Simulations and Results . . . 26
2.3 Feasibility Study . . . 30

3 Non-Gaussian State Generation via Deterministic Photon Subtraction **32**
3.1 System Description and Input–Output Formulation . . . 33
3.2 First-Order Coherence Analysis and Temporal Mode Decomposition . . . 34
3.3 Calculation of the Output Quantum State . . . 40
3.4 Generating Single-Mode Non-Gaussian States . . . 42
3.5 Current State of Chiral Waveguide–Emitter Coupling . . . 48

4 One-Way Multi-Emitter Cascade for Photon-Number-Resolving Detection **49**
4.1 Modeling and Formulation . . . 50
4.1.1 Cascaded photon subtraction scheme . . . 50
4.1.2 Scattering matrix calculation . . . 52
4.1.3 Equivalent input-output network model . . . 56
4.2 Results and Discussion . . . 57
4.2.1 Linear analysis . . . 58
4.2.2 Nonlinear analysis . . . 60
4.3 Comparison with Conventional PNR Detection Scheme . . . 67

5 Two-Way Two-Emitter Cascade for Selective Single-Photon Subtraction **70**
5.1 Description of the Proposed Scheme . . . 70
5.2 Theoretical Modeling . . . 73
5.3 Simulation Results and Discussion . . . 74

6 Multi-Photon Fock State Generation via a Generalized Selective Photon Subtractor **81**

6.1 Photon Culling: Mathematical Modeling 82

6.2 Proposed Scheme 89

6.2.1 Operational principle 89

6.2.2 Input-output formulation 91

6.3 Simulation Results and Discussion 93

7 Conclusions **101**

7.1 Future Directions and Outlook 103

References **105**

APPENDICES **120**

A Derivation of the Optical Bloch Equations **121**

B Derivation of First Autocorrelation Matrix **124**

B.1 Squeezed vacuum input 124

B.2 Coherent input 125

C Scattering Matrices for Two and Three Photon Inputs **127**

List of Figures

1.1 (a) Beam-splitter-based photon subtractor (HT-BS: high-transmission beam-splitter) [83]. (b) Schematic of the experimental setup used in Ref. [108] for mode-tunable photon subtraction. 4

1.2 (a) Extraction of a single photon by a Λ-atom coupled to photons of opposite polarizations [125]. (b) A schematic view of the setup used by Rosenblum et al. [118]. 7

1.3 Two cascaded single-port cavities interacting through a uni-directional bosonic field [24]. 10

1.4 Using virtual cavities for representation of different modes. (a) single-mode input and output, and (b) multi-mode input and output [63]. 12

2.1 (a) The proposed atom–cavity scheme for deterministic single-photon subtraction from a light pulse incident on the input mode b_{in}; (b) A crossed nanobeam cavity structure as a potential physical implementation of the scheme. 16

2.2 Probability of successful photon subtraction ($P_2 = |t_k|^2$) with respect to the angular frequency of the arriving photon, illustrating (a) the effect of the ratio of coupling strengths of different modes ($\kappa_b/g_b = \kappa_r/g_r = 0.5$), and (b) the effect of the cavities' decay rate ($g_r/g_b = 1$ and $\kappa_b/g_b = \kappa_r/g_r = \kappa$). . . 21

2.3 Effect of spontaneous decay of the emitter on the probability of successful photon subtraction ($g_r = g_b$, $\kappa_b/g_b = \kappa_r/g_r = 0.5$, $\Gamma_{13}/g_b = \Gamma_{23}/g_r = \Gamma$). . . 23

2.4 Probability of successful photon subtraction from pulsed input light: (a) Gaussian input ($\kappa = 0.5$), (b) Gaussian input ($g_r/g_b = 1$), (c) rectangular input ($\kappa = 0.5$), and (d) rectangular input ($g_r/g_b = 1$). 24

2.5 Probability of successful photon subtraction from detuned pulsed input light: (a) Gaussian input, and (b) rectangular input ($g_r = g_b$, $\kappa_b/g_b = \kappa_r/g_r = 0.5$, $\Gamma_{13}/g_b = \Gamma_{23}/g_b = 0.02$). 25

2.6 Comparison of analytical and numerical solutions to the system's response in the pulsed regime: (a) Gaussian pulse, and (b) Rectangular pulse ($g_r = g_b$, $\kappa_b/g_b = \kappa_r/g_r = 0.5$, $\Gamma_{13}/g_b = \Gamma_{23}/g_b = 0.02$). 27

2.7 Probability of successful photon subtraction from light pulses containing different number of photons ($g_r = g_b$, $\kappa_b/g_b = \kappa_r/g_r = 0.5$, $\Gamma_{13}/g_b = \Gamma_{23}/g_b = 0.02$). 28

2.8 Effect of (a) coupling strength ratio ($\kappa_b/g_b = \kappa_r/g_r = 0.5$, $\Gamma_{13}/g_b = \Gamma_{23}/g_b = 0.02$), (b) decay rate of cavities ($g_r = g_b$, $\kappa_b/g_b = \kappa_r/g_r = \kappa$, $\Gamma_{13}/g_b = \Gamma_{23}/g_b = 0.02$), and (c) ratio of decay rates in different modes ($g_r = g_b$, $\kappa_b/g_b = 0.5$, $\Gamma_{13}/g_b = \Gamma_{23}/g_b = 0.02$) on photon subtraction probability from pulses with different number of photons. 29

2.9 Probability of successful photon subtraction as a function of the coupling strength-to-cavity decay rate ratio and the coupling strength-to-atomic decay rate ratio. The two modes are assumed to be symmetric with equal parameters ($g_r = g_b = g$, $\kappa_b = \kappa_r = \kappa$, $\Gamma_{13} = \Gamma_{23} = \Gamma$). The markers indicate where different systems described in the text fall on the performance diagram, with their corresponding success probabilities denoted in the legend. 30

3.1 Schematic view of a Λ-type atom coupled to a chiral waveguide. The input pulse is sent to the right-propagating (green) mode, the subtracted photon is reflected to the left-propagating (red) mode, while the remaining pulse leaves the waveguide from the same mode's output. 34

3.2 System output with a single-photon Fock state as input ($\tau = 1/\gamma_g$), showing (a) modal decomposition of the right (r_{out}) output mode, (b) modal decomposition of the left (l_{out}) output mode, and (c) temporal distribution of photons in input and output pulses. 38

3.3 System output with a two-photon Fock state as input ($\tau = 100/\gamma_g$), showing (a) modal decomposition of the right (r_{out}) output mode, (b) modal decomposition of the left (l_{out}) output mode, and (c) temporal distribution of photons in input and output pulses. 38

3.4 System output with a squeezed vacuum state with $\bar{n} = 0.1$ photons as input ($\tau = 100/\gamma_g$), showing (a) modal decomposition of the right (r_{out}) output mode, (b) modal decomposition of the left (l_{out}) output mode, and (c) temporal distribution of photons in input and output pulses. 39

3.5 System output with a coherent state with $\bar{n} = 1$ photon as input ($\tau = 100/\gamma_g$), showing (a) modal decomposition of the right (r_{out}) output mode, (b) modal decomposition of the left (l_{out}) output mode, and (c) temporal distribution of photons in input and output pulses. 40

3.6 Quantum network comprising one input and two output cavities interacting with the emitter in a cascade manner. The couplings of the output cavities are adjusted so that they absorb the main wavepacket at each output pulse. 41

3.7 Proposed configurations for generation of single-mode non-Gaussian states from pulsed Gaussian input light: (a) configuration with one demultiplexer and two detectors used for squeezed vacuum input pulses, and (b) configuration with two demultiplexers and four detectors used for coherent input pulses. 43

3.8 Photon subtraction results for a squeezed vacuum input $|\zeta\rangle$ with a mean photon number of $\bar{n} = 0.1$. The plots show the Wigner functions for (a) $\hat{a}\,|\zeta\rangle$, (b) $\hat{s}\,|\zeta\rangle$, (c) generated state by the proposed subtractor with no measurement performed by D1, and (d) generated state by the proposed subtractor where both D1 and D2 are used for measurements according to the described scenario. 44

3.9 Photon subtraction results for a squeezed vacuum input $|\zeta\rangle$ with a mean photon number of $\bar{n} = 0.2$. The plots show the Wigner functions for (a) $\hat{a}\,|\zeta\rangle$, (b) $\hat{s}\,|\zeta\rangle$, (c) generated state by the proposed subtractor with no measurement performed by D1, and (d) generated state by the proposed subtractor where both D1 and D2 are used for measurements according to the described scenario. 44

3.10 Fidelity between the generated states (obtained by applying different photon subtraction methods, as indicated in the plot legend) and odd Schrödinger's cat states of amplitude α. The input $|\zeta\rangle$ is a squeezed vacuum state with mean photon numbers: (a) $\bar{n} = 0.1$, and (b) $\bar{n} = 0.2$. 45

3.11 Photon subtraction results for a coherent input with a mean photon number of $\bar{n} = 1$. The plots show the Wigner functions for (a) generated output state when the subtracted photon in detected in 1st mode, (b) generated output state when the subtracted photon in detected in 2nd mode, (c) generated output state when the subtracted photon in detected in 3rd mode, and (d) a displaced cat state with parameters $\alpha = 0.60$, $\beta = 3.90$, and $\gamma = 0.07$. . 47

3.12 Photon subtraction results for a coherent input with a mean photon number of $\bar{n} = 3$. The plots show the Wigner functions for (a) generated output state when the subtracted photon in detected in 1st mode, (b) generated output state when the subtracted photon in detected in 2nd mode, (c) generated output state when the subtracted photon in detected in 3rd mode, and (d) a displaced cat state with parameters $\alpha = 0.47$, $\beta = 3.83$, and $\gamma = 0.56$. . . 47

4.1 (a) Schematic of the photon subtractor as a three-port quantum optics device consisting of a Λ-type emitter coupled to two chiral (one-way) waveguide modes, and (b) A cascade of n photon subtractors forming a PNR detector capable of resolving up to $n + 1$ photons. 51

4.2 (a) Probability of successfully subtracting a single photon by a cascade of λ emitters, based on equation 4.16, (b) Relative error of a PNR detector with a cascade of $n = 4$ emitters, for input pulses with different photon numbers N, and (c) Relative error of a PNR detector as a function of the input photon number N and the number of emitters n for $\delta\gamma_g = 0.5$. . . . 59

4.3 (a) Second-order correlation of the output photons at the $a_{out,1}$ mode of a single-emitter photon subtractor, shown for various values of $\delta\gamma_g$. The first row corresponds to a two-photon input with no photon subtracted, the second row to a three-photon input with no photon subtracted, and the third row to a three-photon input where the third photon is subtracted. (b) Same results as in (a), obtained using the Monte-Carlo method by averaging across 50,000 trajectories. (c) Zero-delay single-time correlation function $g^{(2)}(0)$ as a function of $\delta\gamma_g$ for the three cases mentioned above, represented by the blue, red, and yellow curves, respectively. 61

4.4 (a, b, c) Probabilities of subtracting no photon, the first photon, and the second photon from a two-photon input, respectively. (d, e, f, g) Probabilities of subtracting no photon, the first photon, the second photon, and the third photon from a three-photon input, respectively. The solid and dashed lines represent the nonlinear and linear analytical solutions, respectively, while the circle markers denote the numerical solutions obtained using the quantum trajectory method, averaged across 2000 trajectories. 62

4.5 Probabilities of subtracting no photon (first column), the first arriving photon (second column), and the second arriving photon (third column) from two overlapping photons as a function of their separation time. First, second, and third row correspond to the weak interaction ($\delta\gamma_g = 0.1$), intermediate interaction ($\delta\gamma_g = 1$), and strong interaction ($\delta\gamma_g = 10$) regimes, respectively. Solid lines represent analytical results, while dots indicate numerical results obtained using the Monte Carlo method, averaged over 10,000 trajectories. Dashed lines correspond to linear solutions. 64

4.6 (a) Second-order correlation of the output photons at the $a_{out,1}$ mode of a single-emitter photon subtractor, shown for various values of $\delta\gamma_g$. The first and second rows corresponds to a bunched and anti-bunched two-photon input with amplitudes given in equations 4.25.a and 4.25.b, respectively. (b) Same results as in (a), obtained using the Monte-Carlo method by averaging across 50,000 trajectories. (c) Zero-delay single-time correlation function $g^{(2)}(0)$ of the output light as a function of $\delta\gamma_g$ for these two correlated input states, along with the uncorrelated input, as described in equation 4.15. (d) Left to right: probability of successfully subtracting a single photon, the first arriving photon, and the second arriving photon, respectively. The circle markers denote the numerical solutions obtained using the quantum trajectory method, averaged across 1,000 trajectories. 65

4.7 (a) Relative error of a PNR detector consisting of a cascade of $n = 4$ quantum emitters when subjected to Gaussian input pulses with different photon numbers. (b) Relative error of PNR detectors with cascades of $n = 2$ to $n = 5$ quantum emitters when subjected to Gaussian input pulses with $N = 3$ photons. The dash-dotted lines indicate the results from the linear analysis, while the dots represent nonlinear results calculated using the quantum trajectory method, averaged across 5,000 trajectories. 66

4.8 (a) Schematic of a conventional PNR detector, which spatially distributes input photons among multiple single-photon detectors using a cascade of beamsplitters. (b) Performance comparison between the conventional scheme achievable with $n = 4$ beamsplitters and the photon-subtraction-based scheme with a cascade of $n = 4$ quantum emitters, shown for different values of the parameter $\delta\gamma_g$. The results for the proposed scheme are calculated using the quantum trajectory method, averaged across 5,000 trajectories. 68

5.1 Diagram of the proposed photon subtraction system based on two identical three-level quantum emitters coupled to a chiral waveguide. The initial state of the two emitters is also shown. 71

5.2 Conceptual diagram illustrating a potential implementation of the proposed device, integrating solid-state quantum emitters coupled to a nanophotonic chiral waveguide and a ring resonator drop filter, to subtract a single photon and divert it to a different pathway. 72

5.3 Quantum input-output network block diagram for the proposed scheme. . 74

5.4 Photon subtraction from pulsed Fock state ($\tau = 100/\gamma_g$). 75

5.5 (a) Effect of pulse duration on transmissivity and reflectivity of the device for a single photon input. (b) Probability of successful photon subtraction from different multi-photon Fock states at the input. 76

5.6 Photon subtraction from pulsed coherent state containing different mean number of photons. (a) $\bar{n}_{in} = 0.1$, (b) $\bar{n}_{in} = 1$, and (c) $\bar{n}_{in} = 2$ ($\tau = 100/\gamma_g$). 77

5.7 Ratio of communicated qubits successfully eavesdropped by Eve as a function of mean number of photons in the input coherent pulse ($\tau = 100/\gamma_g$). 78

5.8 (a) Simpler scheme using a photon subtractor made of a single Λ-type emitter, and (b) relative change in average number of photons received by Bob for the two different schemes ($\tau = 100/\gamma_g$). 79

6.1 Schematic of a selective photon subtractor (photon culler), represented as a four-port quantum optics device with one input port and three output ports. 83

6.2 Two photon cullers integrated into a Mach-Zehnder interferometer (MZI) for phase measurement. 87

6.3 (a) The proposed scheme consisting of n three-level emitters coupled to a chiral waveguide, along with their initial states. (b) A potential realization of the scheme in part a, using a chiral photonic crystal waveguide with an acousto-optical switch at the output. 90

6.4 (a) Pulse shape of the subtracted photon in a selective photon subtractor subtracting the 4^{th} arriving photon, for Gaussian coherent inputs with different mean photon numbers $\bar{n}$. (b) Dominant mode shape of the output 3-photon pulse for different values of the time interval width Δ ($\bar{n} = 5$). . 94

6.5 Probability of successful Fock state generation (P), Single-modedness of the generated pulse (S), Photon number standard deviation of the first mode (σ), and Fidelity of the quantum state contained in the first mode with an n-photon Fock state (F) for (a) 2-photon Fock state, and (b) 3-photon Fock state. 95

6.6 Wigner functions of the generated (a) 2-photon, and (b) 3-photon Fock states using the cascaded QED scheme shown in Figure 6.3. The generation probability (P), single-mode purity (S), and fidelity (F) of the produced states are indicated in the plot ($\bar{n} = 5$, $\Delta = \tau/8$, $\gamma\tau = 10^3$) 96

6.7 Effect of (a) photon number n, and (b) post-selection interval Δ, on the Fisher information content of the output light of the interferometer for 3-photon input pulses generated via selective photon subtraction. 97

6.8 Conditional probability $P(q|\,\phi)$ vs. phase shift ϕ for 3-photon Fock state inputs when (a) No post-selection applied ($\Delta \to \infty$), and (b) post selection applied with $\Delta = \tau/32$. 98

6.10 Conditional probability $P(q|\,\phi)$ vs. phase shift ϕ for 2-photon Fock state inputs and no post-selection ($\Delta \to \infty$). Dotted lines are analytical results for the ideal photon culler, circle markers are Monte-Carlo simulation results for the proposed emitter cascade scheme. 99

Chapter 1

Introduction

Quantum mechanics presents a remarkable richness compared to classical physics, thanks to concepts like superposition and entanglement. These unique characteristics allow systems to exist in quantum states that exhibit physical behaviors beyond the reach of classical systems. One prominent application of this richness is in the field of quantum information, where the encoding of information in quantum states becomes feasible, unlocking new possibilities in computation, cryptography, and communication. Among the various approaches to quantum information technology, quantum optics stands out, as it enables the realization of both quantum computing [127] and long-distance communication [86] on a single platform, facilitating the development of quantum information networks.

Discrete Variable (DV) and Continuous Variable (CV) regimes represent distinct approaches in quantum optical information processing. These two regimes are primarily characterized by the Hilbert spaces employed for the representation of quantum states of light. Within the DV approach, quantum states are typically illustrated in a finite-dimensional space, commonly associated with the polarization or path of single or multiple photons. Conversely, in the CV approach, individual spatiotemporal modes of light are treated as single harmonic oscillators. Information is encoded in the quadrature components of multi-photon quantum states within these modes, which occupy an infinite-dimensional Hilbert space and thereby offer enhanced versatility and a broader range of applications [12,39,135,144]. Both of these approaches have evolved over time and demonstrated their inherent potential in various applications of quantum technologies including quantum communication [147], computing [22], and metrology [154]. The development of single-photon sources and single-photon detectors enabled experimental studies of quantum light sources at the single-photon level, and such sources have proved a critical tool in a variety of applications, such as quantum communication [26], information [25,145], sens-

ing [25] and imaging [18]. However, experimental access to the rich space of non-classical states in the CV regime requires the development of techniques for the generation and robust detection of multi-photon quantum light pulses.

The quantum states used in CV regime are classified into two categories, called Gaussian and non-Gaussian, based on the shape of the probability distribution they exhibit in the optical phase space. The first group either occurs in nature, such as vacuum and thermal states, or can be experimentally generated on-demand, like coherent and squeezed states. On the other hand, the generation of non-Gaussian states of light with high fidelities remains experimentally challenging [80]. At the same time, a variety of applications in CV quantum optics explicitly require non-Gaussian states and non-Gaussian operators, as they provide a rich resource for a wide range of quantum technologies [34, 43, 79]. For instance, a no-go theorem demonstrates that achieving fault-tolerant quantum computing is not possible solely with Gaussian states and operations [89]. In another example, it has been shown that leveraging Schrödinger's cat state as a resource enables the realization of quantum error correction [79]. Similarly, non-Gaussian operators can enable CV entanglement distillation [133], which is impossible in Gaussian regime based on another no-go theorem [33]. Additionally, non-Gaussian states find applications in long-distance communication using quantum repeaters and teleportation via entangled cat states [43], as well as in interfacing discrete-continuous regimes [61].

The quantum states mentioned above are superpositions or mixtures of Fock states, which are the eigenstates of the harmonic oscillator with well-defined photon numbers. This concept leads to the idea of photon arithmetic, involving the addition and subtraction of single photons to light fields as a means of manipulating their quantum state [5]. Traditionally, this has been done through application of creation and annihilation operators [50]. The schemes for implementation of these operators were probabilistic in nature and relied on detection events to herald the successful completion of the process [146, 152]. Using these ladder operators, it is possible to transition from one eigenstate to another. As a result, any arbitrary quantum operation in this case can be represented as a combination of photon creation and annihilation operators [94]. When combined with Gaussian operations such as displacement and squeezing, it is possible to generate any quantum state by utilizing either the creation or annihilation operator. Dakna et al. [27] demonstrated that starting from the vacuum state, any single-mode state of light can be generated through the alternate application of photon creation and displacement operators. Similarly, Fiurasek et al. [37] showed that the same level of control can be achieved using the photon annihilation operator in combination with displacement and squeezing operations.

The manipulation of quantum states of light by subtracting photons from them has been a topic of interest for a long time [28]. The generated states have found applications

in continuous variable quantum communication [92] and computation [42]. In addition to quantum state engineering, this operation can also be utilized in other applications such as entanglement distillation [153], probing fundamental principles of quantum optics [9, 151], and the realization of photon number resolving (PNR) detectors [129]. PNR detection is required to characterize and diagnose many-photon states of light by measuring their photon-number distributions. Furthermore, generalized detection schemes composed of such detectors can lend access to novel forms of quantum tomography. In particular, characterizing complex, correlated many-photon states [30,57,87,95,107] can help to reveal dynamics of many-body quantum systems.

1.1 Single-Photon Subtraction

1.1.1 Probabilistic approach

In the conventional scheme for non-deterministic single photon subtraction, a low-reflectivity beamsplitter is utilized to extract a small fraction (ideally one photon) of the input light. This method was first successfully implemented experimentally by Wenger et al. in 2004 [146]. The beamsplitter operator can be written as $B = \exp[-\theta(\hat{a}^\dagger \hat{b} - \hat{a}\hat{b}^\dagger)]$ where $\hat{a}$ and $\hat{b}$ are annihilation operators of the respective modes (See Figure 1.1.(a)) and the reflectivity of mode a is related to the parameter θ as $R = \sin^2\theta$. Assuming that the input light $|\psi\rangle$ is applied to mode a, while input b is in vacuum state, the output state can be written as follows in the limit of small reflectivity:

$$|\psi_{out}\rangle \approx \left[1 - \theta\left(\hat{a}^\dagger \hat{b} - \hat{a}\hat{b}^\dagger\right)\right] |\psi\rangle_a |0\rangle_b \approx |\psi\rangle_a |0\rangle_b + \theta \hat{a} |\psi\rangle_a |1\rangle_b \tag{1.1}$$

According to the above expression, the successful application of the annihilation operator to the input field occurs only when a single photon is detected at the output mode b, and the process therefore relies on detection events to herald its successful completion. To minimize the occurrence of multi-photon subtraction, the reflectivity parameter θ needs to be small, resulting in a low success probability for the process. It is also important to note that as $\hat{a} = \sum_{n>0} \sqrt{n}\, |n-1\rangle \langle n|$, this success probability is not constant but rather dependent on the average number of photons at the input. Furthermore, in a cascade of non-deterministic photon subtractors, the success probability decreases rapidly, thereby limiting the number of photons that can be subtracted.

Schrödinger's kitten states, as well as other low-photon-number states, have been successfully generated using this type of photon subtraction [10,93]. Using pulses of squeezed

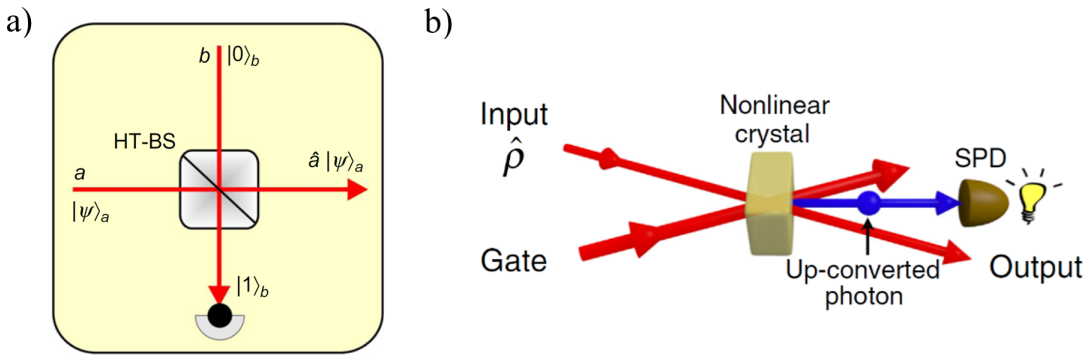


Figure 1.1: (a) Beam-splitter-based photon subtractor (HT-BS: high-transmission beam-splitter) [83]. (b) Schematic of the experimental setup used in Ref. [108] for mode-tunable photon subtraction.

light as the input to the above-described photon subtractor, the non-Gaussian statistics of the output light has been clearly demonstrated by reconstruction of the Wigner function from the experimental data in the work of Wenger et al. [146]. Later in 2007, Ourjoumtsev et al. carried out the same experiment with an optimized homodyne detection and were able to observe Wigner functions with negative values, resembling the Schrodinger's kitten state [93].

When the initial number of photons in the light field is precisely known, or equivalently, when the field is in a Fock state, annihilation and creation operators decreases or increases the photon number exactly by one. This behavior aligns with the classical expectation of subtracting or adding a single photon. Consequently, these operators are conventionally referred to as photon subtraction and addition [94]. However, the situation becomes considerably different when the light field is in a superposition or mixture of Fock states. These operators when applied to superposition states lead to substantial reshaping of the photon number distribution at the output, rather than simply shifting it up or down by one [83]. In such cases, the results may entirely contradict classical expectations. For example, when subtracting a photon from a thermal state, the result is a doubling of the number of photons, which is a highly counterintuitive outcome [83]. However, this non-intuitive behavior can be understood when considering that these processes of photon subtraction and addition are inherently non-deterministic. This arises from the fact that the annihilation and creation operators do not preserve the trace of the density matrix and, as a result, cannot be implemented in a system that evolves under a deterministic Hamiltonian [68]. Therefore, the only way these operators can be implemented is through probabilistic methods.

In the scheme described above, when the input light consists multiple temporal modes, a single photon is subtracted from all modes, resulting in the loss of coherence among them. Consequently, the output state is a mixed state. To address this limitation, Ra et al. proposed a method that enables selective subtraction of photons from individual input modes or their superposition, providing greater control over the subtraction process [108]. Their scheme works based on sum-frequency generation in a nonlinear crystal through interaction of the input light with a strong gate beam. As depicted in Figure 1.1.(b), the successful subtraction of a single photon from the input is heralded by the detection of an up-converted photon in their experimental setup. Additionally, the specific input mode from which the photon is subtracted is determined by the modal composition of the gate beam.

Another method for non-deterministic extraction of single photons from the incident light is through the use of a two-level atom. In this approach, the input light excites the atom, resulting in the backscattering of single photons. The number of subtracted photons is primarily influenced by the photon arrival rate in the incident light and the coupling strength between the atom and light modes. In a recent study by Koch et al., they employed this approach to extract single photons from a continuous-wave coherent light source [65]. The output light exhibited the expected super-Poissonian statistics. To implement this technique, silicon-vacancy centers coupled to laser-written waveguides in diamond were used to create an on-chip platform for photon subtraction.

1.1.2 Deterministic approach

The photon subtraction techniques discussed above suffer from two major drawbacks, as outlined in the previous section. First, they are inherently non-deterministic processes, meaning that only a very small fraction of attempts results in a subtracted photon. Second, their success probability depends on the number of photons present at the input. This has led to the concept of deterministic photon subtraction, which aims to subtract exactly one photon from the input light regardless of the photon number and arrival rate at the input. Recently, approaches for deterministic photon and phonon arithmetic have been proposed and successfully demonstrated across various quantum mechanical platforms, including single-atom cavity QED [118], circuit QED [66], trapped ions [141], and Rydberg superatoms [129]. These implementations operate as self-terminating processes, where the subtraction of the first arriving photon renders the system transparent, preventing the subtraction of any additional photons [31].

Unlike the conditional approach, a deterministic single-photon subtractor, represented by the operator $\hat{s} = \sum_{n>0} |n-1\rangle \langle n|$, is capable of precisely subtracting one photon from

the input light. Consequently, assuming the probability of vacuum is negligible, the photon number probability distribution at the output is identical to that of the input, but shifted down exactly by one photon. The application of this operator to a state with a Gaussian distribution can result in the creation of a non-Gaussian state [53]. Therefore, deterministic photon subtraction holds the potential for engineering quantum states of light, similar to conventional non-deterministic photon addition and subtraction. Additionally, this type of photon subtractor can find other applications due to its unconditional outcome. For example, it can be utilized in the realization PNR detectors and the implementation of a photon number splitting (PNS) attack on quantum key distribution (QKD), among other potential applications [53, 118].

In 2011, Honer et al. proposed that the Rydberg blockade effect in an artificial superatom provides a high-fidelity single photon absorber and can be used for deterministic subtraction of single photons from the incident light field [53]. This effect arises from the strong dipole-dipole interaction between Rydberg-excited atoms, which leads to an energy shift in nearby atoms. Consequently, the simultaneous excitation of neighboring atoms to Rydberg states is prevented, resulting in a blockade of their excitation. Therefore, the excited state will be a coherent superposition with a single excitation shared between all the N atoms in the blockade radius r_B, providing an enhanced coupling $\sqrt{N}$ times larger compared to an individual scatterer. Furthermore, the coupling between this collective excited state with $N-1$ dark states can scale the probability to absorb a single photon as $N/(N+1)$. This idea was experimentally realized by Tresp et al. in 2016 based on a cold atomic cloud of optically trapped ^{87}Rb atoms [138]. By cascading such photon subtractors, deterministic subtraction of multiple photons from the input light has also been recently reported [129].

Another deterministic photon subtractor in the literature operates based on the single photon Raman interaction (SPRINT) method [118]. It was originally proposed by Pinotsi and Imamoglu as a means for absorption of single photon pulses with probability approaching unity [105]. In this type of interaction, population transfer occurs in a three-level Λ-type atom between its two ground levels by simultaneously absorbing a single photon and emitting another photon [119]. In the ideal limit, where both ground-excited transitions are coupled to the respective light modes with the same coupling strength, this population transfer can occur directly without populating the intermediate excited state.

Figure 1.2.(a) shows how this photon subtraction scenario works for a Λ-type emitter interacting with a waveguide where different transitions are coupled to different propagation directions of light. Suppose that the emitter is initially at $|g_1\rangle$. If a weak resonant probe is sent from left, the $|g_1\rangle - |e\rangle$ transition dipole starts oscillating and radiates an electromagnetic field in the same direction as the probe. In resonance the emitted field lags

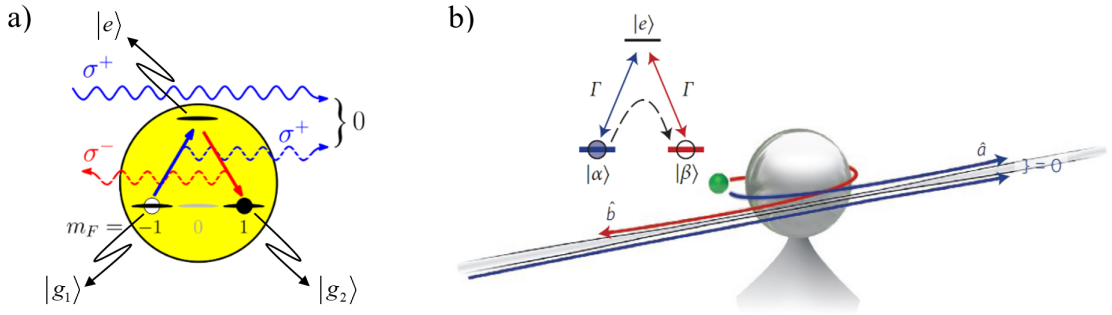


Figure 1.2: (a) Extraction of a single photon by a Λ-atom coupled to photons of opposite polarizations [125]. (b) A schematic view of the setup used by Rosenblum et al. [118].

by π compared to the incident field and destructively interferes with it. This destructive interference forces the emitter to decay to $|g_2\rangle$ by emitting a single photon in the opposite direction. After reflection of this first photon, as the emitter is in $|g_2\rangle$, it no more interacts with the incident field. Hence all the subsequent arriving photons will be transmitted, leading to the probability of subtracting more than one photon becoming exactly zero. This property enables the device to function as an ideal deterministic single photon subtractor, provided that the atom-field coupling strength is sufficiently high to suppress the probability of subtracting zero photons.

The SPRINT-based single-photon subtractor was first experimentally realized by Rosenblum et al. in 2015 [118,125]. They used single cold rubidium atoms coupled to evanescent TM modes of on-chip ultrahigh-Q microsphere resonators. These modes exhibit opposite polarizations for clockwise (CW) and counterclockwise (CCW) propagating photons. Furthermore, these light modes are evanescently coupled to a nano-fiber. Consequently, different transitions of their Λ-system are coupled to different propagation directions of light. When a photon is subtracted, it is reflected in the opposite direction; otherwise, it can transmit through the system. Their setup is schematically shown in Figure 1.2.(b).

In the weak excitation limit, the deterministic mechanisms described above extract the first arriving photon from the incident light. Consequently, since the subtracted photon temporally precedes the transmitted ones, inevitable temporal entanglement is generated in the time domain, which reduces the purity of the output states. The purity approaches 0.5 as the number of photons at the input increases [44]. As a result, the process cannot be fully described by the single-mode operator $\hat{s}$ introduced earlier. However, modal purity can be improved by post-selecting the output states based on the detection time of the subtracted photon, at the cost of reduced device efficiency. There are also specific applications, such

as the realization of PNR detectors, where this modal impurity does not significantly affect overall system performance [53]. Furthermore, applying high photon rates to the emitter may lead to its saturation, which can further alter the behavior of the output light.

1.2 Theoretical Background

This section provides a brief introduction to two key theoretical concepts: input-output formalism and the SLH framework, which form the foundation for the analyses and simulations presented in the subsequent chapters on the photon subtraction systems.

1.2.1 Input-output formalism of quantum optics

Input-output formalism is a method for studying the interaction of localized quantum systems with guided-wave quantized bosonic fields. It was originally formulated in 1985 by Gardiner and Collett in their seminal paper [41] and found wide application in the field of quantum optics where the bosonic field is an optical-frequency electromagnetic wave, and the quantum system typically involves atom-cavity interactions [115]. Using this method, the entire system is modeled in the Heisenberg picture, resulting in a general differential equation that describes the evolution of arbitrary system operators. Additionally, it provides a relationship between the input and output field operators [24].

Total Hamiltonian in this case can be written as $H_{\text{tot}} = H_{\text{sys}} + H_{\text{B}} + H_{\text{int}}$ where H_{sys} governs the internal dynamics of the localized quantum system, H_{B} is the bosonic field Hamiltonian, and H_{int} represents the interaction between the system and the field. Integrating over all frequency modes of the field, the field Hamiltonian can be expressed as $(\hbar = 1)$:

$$H_{\text{B}} = \int_0^\infty d\omega \omega b^\dagger(\omega)\, b(\omega) \tag{1.2}$$

where $b(\omega)$ is the annihilation operator of the field mode of frequency ω satisfying the commutation relation $[b(\omega), b^\dagger(\omega')] = \delta(\omega - \omega')$. The interaction Hamiltonian can also be assumed to have the following linear form, as arises in dipole-approximated light-matter interactions:

$$H_{\text{int}} = i \int_0^\infty d\omega \kappa(\omega) \left[b^\dagger(\omega)\, b(\omega)\right] \left[c - c^\dagger\right] \tag{1.3}$$

in which c is a system operator and $\kappa(\omega)$ is the coupling strength between the system and the field. In the weak coupling regime where the energy transfer between the system and the field happens on time scales much longer than optical oscillation periods, the rotating wave and Markov approximations can be made to further simplify the above Hamiltonian as follows:

$$H_{\text{int}} \approx i\sqrt{\frac{\gamma}{2\pi}} \int_{-\infty}^{\infty} d\omega \left[cb^{\dagger}(\omega) - c^{\dagger} b(\omega) \right] \tag{1.4}$$

where considering that c is a lowering operator, γ is the corresponding decay rate of excitations from the quantum system to the guided bath. As can be seen, the lower limit of the integral in the above expression has been extended to $-\infty$. This is justified as only field frequencies in the vicinity of the system's dynamic frequency are important. Introducing the above Hamiltonians to the Heisenberg equation, gives the following equation for the evolution of any arbitrary system operator over time:

$$\dot{a}(t) = -i\left[a(t), H_{\text{sys}}\right] - \left(\left[a(t), c^{\dagger}(t)\right] \left(\tfrac{\gamma}{2} c(t) + \sqrt{\gamma} b_{in}(t) \right) - \left(\tfrac{\gamma}{2} c^{\dagger}(t) + \sqrt{\gamma} b_{in}^{\dagger}(t) \right) \left[a(t), c(t)\right] \right) \tag{1.5}$$

The input operator $b_{in}(t)$ in the above equation represents the field incident on the quantum system derived by free propagation of the field $b_0(\omega) = b(\omega)|_{t=t_0}$ from an initial time t_0 using the following expression:

$$b_{in}(t) := \frac{1}{\sqrt{2\pi}} \int_{-\infty}^{\infty} d\omega e^{-i\omega(t-t_0)} b_0(\omega) \tag{1.6}$$

Similarly, the output field operator $b_{out}(t)$ immediately after interaction with the quantum system can be derived by back propagation of the field $b_1(\omega) = b(\omega)|_{t=t_1}$ from a later time t_1 according to the following equation:

$$b_{out}(t) := \frac{1}{\sqrt{2\pi}} \int_{-\infty}^{\infty} d\omega e^{-i\omega(t-t_1)} b_1(\omega) \tag{1.7}$$

The Heisenberg equation for the entire system gives the following important relation between the input, output, and system fields:

$$b_{out}(t) = b_{in}(t) + \sqrt{\gamma} c(t) \tag{1.8}$$

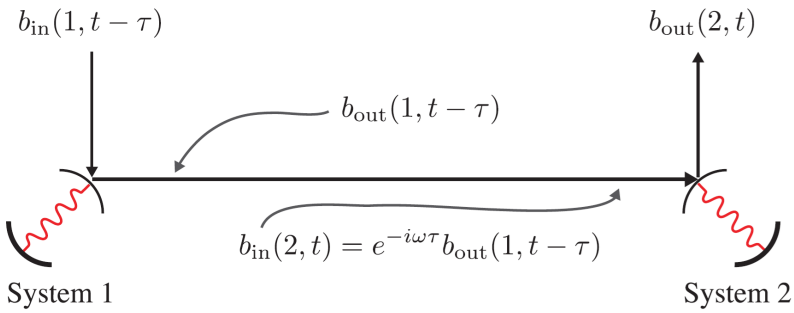


Figure 1.3: Two cascaded single-port cavities interacting through a uni-directional bosonic field [24].

The solution to equation 1.5 can be expressed as $a(t) = U^{\dagger}(t)\, aU(t)$, where $U(t)$ is the unitary propagator of the system, evolving any arbitrary system operator in the Heisenberg picture:

$$U(t) = \exp\left\{\int_{t_0}^{t} ds \left(-iH_{\text{sys}} + \left[Lb_{in}^{\dagger}(s) - L^{\dagger} b_{in}(s)\right]\right)\right\} \tag{1.9}$$

In this equation $L = \sqrt{\gamma} c$ is the coupling operator, representing the coupling of the system to the field.

1.2.2 SLH framework for modeling networked quantum systems

The above formalism can be extended to the more general case of a quantum input-output network, where multiple localized quantum systems interact with a shared bosonic field in a cascaded fashion, such that the output field from one system acts as the input to another system. As a simple example consider the system shown in Figure 1.3, where two one-sided cavities are cascaded to form a two-node quantum network. The input field to the network is first incident on cavity 1, then the reflected output field is fed as input to cavity 2. Time needed for propagation of the field between the systems is denoted by τ. Assuming that τ is much shorter than the interaction time $1/\gamma$ between the system and the field, one can neglect this delay time and perform an input-output analysis similar to the one introduced above in the limit of $\tau \to 0$ to derive the governing equation of the system. Results show that the dynamics of the system can be expressed by similar equations as those derived for the case of a single quantum system interacting with the field, but with the following

effective Hamiltonian and coupling operator:

$$\begin{aligned} H_{\text{eff}} &= H_{\text{sys},1} + H_{\text{sys},2} - i\frac{\sqrt{\gamma_1\gamma_2}}{2}\left(c_2^\dagger c_1 - c_1^\dagger c_2\right) \\ L_{\text{eff}} &= \sqrt{\gamma_1}c_1 + \sqrt{\gamma_2}c_2 \end{aligned} \tag{1.10}$$

The SLH framework, developed by Gough and James in 2009 [45, 46], is an extension of the above approach for analyzing quantum networks. It provides a systematic method to handle more complex networks, allowing for a comprehensive understanding of their behavior. In this formalism, each localized quantum system is represented by a triple of operators $\mathbf{G} = (\mathbf{S}, \mathbf{L}, H)$ which respectively denote the scattering operator, the Lindblad operator responsible for coupling of the system with the bath of modes in the channel, and the Hamiltonian of the system. When these quantum systems are connected to form a network, these operator triples can be combined following a set of rules to create the SLH formulation for the resulting composite system. For example, when two quantum systems represented by $\mathbf{G}_1 = (\mathbf{S}_1, \mathbf{L}_1, H_1)$ and $\mathbf{G}_2 = (\mathbf{S}_2, \mathbf{L}_2, H_2)$ are cascaded, the SLH triple of the combination will be given by:

$$\mathbf{G}_{\text{T}} = \mathbf{G}_2 \triangleleft \mathbf{G}_1 = \left(\mathbf{S}_2\mathbf{S}_1, \mathbf{L}_2 + \mathbf{S}_2\mathbf{L}_1, H_1 + H_2 + \frac{1}{2i}\left(\mathbf{L}_2^\dagger\mathbf{S}_2\mathbf{L}_1 - \mathbf{L}_1^\dagger\mathbf{S}_2^\dagger\mathbf{L}_2\right)\right) \tag{1.11}$$

which is consistent with the result given in equation 1.10 considering that for the single-port cavity $\mathbf{S} = \mathbf{I}$.

The above analysis gives the output field operator in the Heisenberg picture enabling calculation of mean values and correlation functions of the emitted fields. However, in certain applications of quantum information and communication, we are specifically concerned with the quantum state content of light pulses as they propagate through a quantum network. This becomes more intricate when dealing with light pulses that consist of multiple wave packets or temporal modes. In 2019, Kiilerich and Molmer developed a formalism for modeling the interaction between traveling quantum pulses of light and local quantum scatterers [63]. In their proposed method, each temporal mode of the light pulse was treated as oscillating mode of a virtual cavity interacting with the quantum system in a cascaded manner. The time-dependent complex coupling of the input and output cavities to the continuum field was chosen according to the corresponding mode function:

$$g_u(t) = \frac{u^*(t)}{\sqrt{1 - \int_0^t dt' |u(t')|^2}} \qquad g_v(t) = -\frac{v^*(t)}{\sqrt{\int_0^t dt' |v(t')|^2}} \tag{1.12}$$

which are determined by solving the quantum stochastic differential equation governing the system [47, 90].

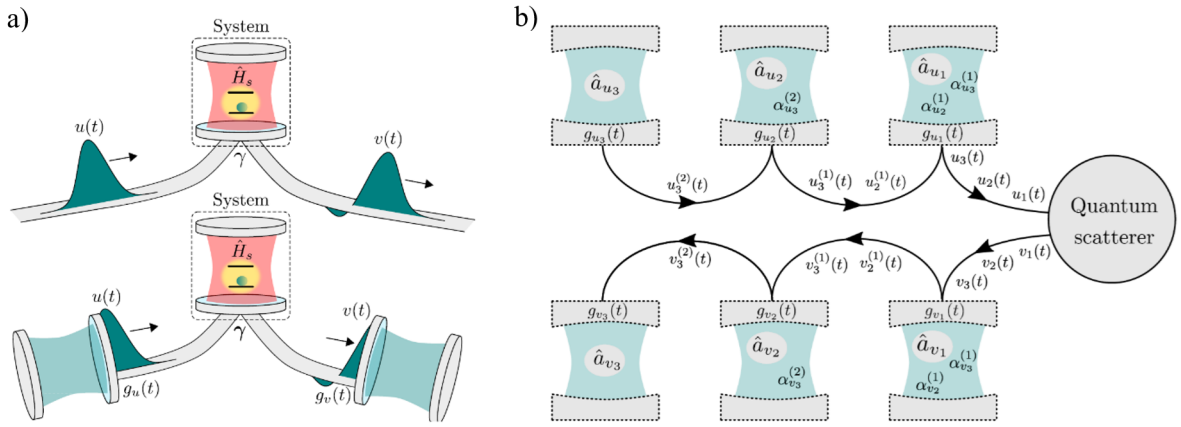


Figure 1.4: Using virtual cavities for representation of different modes. (a) single-mode input and output, and (b) multi-mode input and output [63].

In this way, the input cavity is able to emit its stored quantum state to a traveling wavepacket characterized by the desired mode function $u(t)$, while the output cavity absorbs a wavepacket with mode function $v(t)$ (see Figure 1.4.(a)). In the more general case of a quantum scatterer interacting with multi-mode input and output light, there will be multiple cavities cascaded with the scatterer at its input and output ports as shown in Figure 1.4.(b). Finally, since the input of this quantum network is in a vacuum state, one can solve the master equation in the Schrödinger picture to obtain the quantum state occupying different modes of the output field, as well as the final quantum state of the scatterer itself:

$$\frac{d\rho}{dt} = -i\left[H,\rho\right] + L\rho L - \frac{1}{2}\left\{L^{\dagger}L,\rho\right\} \tag{1.13}$$

For the case of single input and output modes, the Hamiltonian H and Lindblad operator L will be:

$$\begin{aligned} H(t) &= H_{sys} + \tfrac{i}{2}\left[\sqrt{\gamma}g_u(t)\,a_u^{\dagger}c + \sqrt{\gamma}g_v^{*}(t)\,c^{\dagger}a_v + g_u(t)\,g_v^{*}(t)\,a_u^{\dagger}a_v - \text{H.c.}\right] \\ L(t) &= \sqrt{\gamma}c + g_u^{*}(t)\,a_u + g_v^{*}(t)\,a_v \end{aligned} \tag{1.14}$$

where a_u and a_v are annihilation operators of the input and output cavities, respectively. Before using the above formalism to model the system, it is necessary to identify the dominant modes involved in the output light. One way to achieve this is by calculating the first-order autocorrelation function of the output light. The eigenvectors of the autocorrelation matrix correspond to the dominant modes involved, while the eigenvalues represent the average number of photons present in each mode.

1.3 Research Objectives and Thesis Outline

Upon reviewing the literature on the subject of deterministic photon subtraction, two fundamental gaps in the existing research become evident, highlighting the need for further improvement. Firstly, there is a notable absence of a comprehensive theoretical framework capable of accurately modeling the evolution of optical pulses in terms of both photon statistics and involved quantum states. Second, there is a need for conceptual design and analysis of quantum optical devices that exploit the deterministic nature of photon subtraction and the resulting temporal entanglement. Such devices could enable advanced functionalities in the control and detection of quantum light that are not achievable with conventional probabilistic photon subtractors.

In this thesis, we aim to address the two deficiencies mentioned above by focusing on the SPRINT mechanism as the platform for deterministic photon subtraction. The remaining chapters of the thesis are organized as follows. Chapter 2 presents a comprehensive analysis of a photon subtractor based on a quantum emitter coupled to a bimodal cavity with waveguide coupling. The performance of the photon subtractor in extracting single photons is studied in both single- and multi-photon regimes as a function of the emitter and cavity decay rates, as well as the atom–cavity coupling strength. Chapter 3 investigates the capability of SPRINT-based photon subtraction to generate non-Gaussian states of light from Gaussian inputs, including coherent and squeezed vacuum states. In Chapter 4, we explore cascaded photon subtractors capable of multi-photon subtraction as PNR detectors for counting the photon number in input light pulses, and compare their performance with currently available PNR detection schemes. Chapter 5 introduces the concept of two-way cascading of photon subtractors in chiral waveguides and demonstrates how this scheme can be employed to perform PNS attacks on QKD systems. Chapter 6 extends this approach to cascades with multiple emitters, enabling selective subtraction of single photons based on their position in the arrival-time sequence. Building on this capability, a scheme for generating multi-photon Fock states is presented, and its potential application in quantum metrology is explored. Finally, Chapter 7 concludes the thesis by summarizing the main findings and discussing potential directions for future research. The material presented in Chapters 2, 3, 5, and 6 has been published as four peer-reviewed journal papers [95–98], while a manuscript based on material presented in Chapter 4 is currently under review and available as preprint on arXiv [99].

Chapter 2

Deterministic Photon Subtraction in a Coupled Cavity–Waveguide Setting

In this chapter, we perform a comprehensive analysis of a SPRINT-based photon subtractor comprising a Λ-type emitter in a bimodal cavity directly coupled to two separate waveguide modes. Initially, we conduct a single-photon transport analysis using the input-output formalism to assess the system's capability in redirecting single-photon pulses arriving in one waveguide mode to the other. The insights gained from this analysis are then utilized to optimize the key parameters of the photon subtractor. Subsequently, by treating the system as an input-output quantum network, we numerically simulate its behavior under input pulses containing multiple photons. We then compare the results obtained from the single-photon and multiple-photon solutions to assess the effectiveness of the single-photon transport analysis in predicting and optimizing the device's performance in the multi-photon regime.

2.1 Single-Photon Transport Analysis

2.1.1 Modeling and formulation

Figure 2.1.(a) presents a schematic of the investigated photon subtractor, comprising a Λ-type quantum emitter coupled to a bimodal cavity. Distinct modes of the cavity are illustrated in different colors (blue and red), each regarded as a one-sided cavity with an ideal reflector on one side and a non-perfect mirror on the other. The energy decay

rates κ_b and κ_r correspond to the blue and red cavities, respectively. These are extrinsic decay rates, arising from photon decay from the cavities into the connected waveguides. Intrinsic decay, caused by photon absorption, scattering, or structural imperfections within the cavities, is assumed to be negligible compared to the extrinsic effects. This assumption holds particularly for short input pulses, where the extrinsic decay rate is deliberately set to be high. In high-quality cavities, this typically results in $\kappa_{\text{ext}} \gg \kappa_{\text{int}}$ [15]. The emitter-cavity system is proposed so that each ground-to-excited transition of the emitter selectively couples to one cavity mode through either resonance frequency or polarization selectivity. The coupling strengths for the respective cavity modes are denoted as g_b and g_r. Different modes of the cavity are designed for direct coupling to distinct waveguides, enabling the transmission of input light pulses to the atom-cavity system and the collection of outgoing pulses resulting from the subtraction process. This includes both the subtracted single-photon pulse and the remaining pulse after photon subtraction. A potential approach to experimental realization of the above-described system is depicted in Figure 2.1.(b) This illustration shows two 1D photonic-crystal cavities embedded in two crossed nanobeam waveguides, with a solid-state emitter positioned at the center of the cavities. A grating is used at the end of each nanobeam to couple the vertically propagating light from free space into the structure. The coupled light then is transmitted through the nanobeam to the cavity where the interaction with the emitter takes place. A detailed study of such a doubly resonant photonic crystal nanocavity can be found in Ref. [116].

In this section, we employ the input-output formalism of quantum optics as explained in section 1.2.1 to analytically investigate the interaction of the atom-cavity system with the bath of waveguide modes and examine how photons are transported within the entire bimodal atom-cavity-waveguide system. The extension of the input-output formalism to photon transport in waveguides with embedded atoms was first proposed and formulated by Fan et al. [35]. Subsequently, this formalism has also been applied to study photon transport in cavity-waveguide systems coupled to two-level atoms [115]. However, previous studies on systems consisting of bimodal cavities and three-level atoms have primarily relied on the real-space representation of the eigenstates of the system's Hamiltonian [131, 149]. Utilizing the input-output formalism in our photon transport analysis also helps to maintain consistency with the next section of the chapter, where we treat the system as an input-output quantum network to simulate its response to multi-photon pulses. As mentioned before, this method relies on defining input and output operators in the Heisenberg picture corresponding to each input or output of the system to capture the traveling pulses before and after the interaction takes place.

In general, the photon subtraction process begins by sending an n-photon quantum pulse, ideally with an arbitrary temporal shape and quantum state content – this might

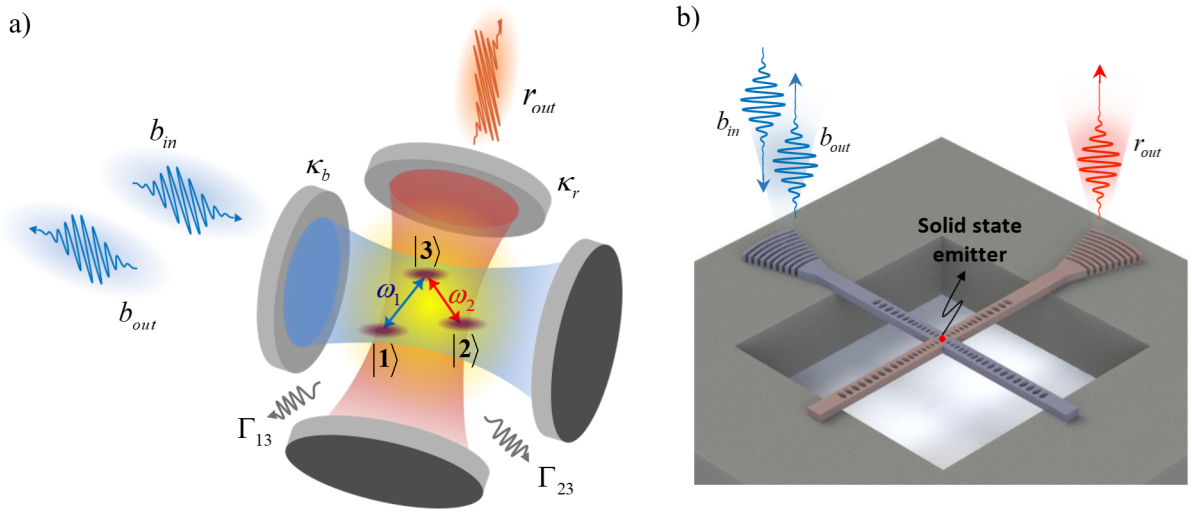


Figure 2.1: (a) The proposed atom–cavity scheme for deterministic single-photon subtraction from a light pulse incident on the input mode b_{in}; (b) A crossed nanobeam cavity structure as a potential physical implementation of the scheme.

even be a multi-mode pulse made of several wavepackets – through the blue waveguide input mode represented by b_{in}. Photons injected by this pulse into the cavity interact with the emitter, initially prepared in state $|1\rangle$, through a coherent Raman process. This process transfers the emitter to state $|2\rangle$ and emits a single photon to the red mode of the cavity. The subtracted photon then decays out of the red cavity, forming a quantum pulse that leaves the system through the red waveguide output mode r_{out}. Additionally, the remaining $n-1$ photons form a reflected pulse that leaves the blue cavity through the output mode b_{out}. Furthermore, to consider the spontaneous decay of the atom, we introduce the output operator e_{out} responsible for the photons emitted by the atom into the external bath of modes in the environment. According to the input–output formalism (see Equations 1.6 and 1.7), these operators are defined as follows [41]:

$$\begin{aligned} b_{in}(t) &:= \frac{1}{\sqrt{2\pi}} \int_{-\infty}^{+\infty} d\omega' b_0(\omega') e^{-i\omega'(t-t_0)} & b_{out}(t) &:= \frac{1}{\sqrt{2\pi}} \int_{-\infty}^{+\infty} d\omega' b_1(\omega') e^{-i\omega'(t-t_1)} \\ r_{out}(t) &:= \frac{1}{\sqrt{2\pi}} \int_{-\infty}^{+\infty} d\omega' r_1(\omega') e^{-i\omega'(t-t_1)} & e_{out}(t) &:= \frac{1}{\sqrt{2\pi}} \int_{-\infty}^{+\infty} d\omega' e_1(\omega') e^{-i\omega'(t-t_1)} \end{aligned} \tag{2.1}$$

where $\alpha_i(\omega') := \alpha(\omega')|_{t=t_i}$ for $\alpha = b, r, e$ are the annihilation operators that annihilate a

photon of frequency ω' in the corresponding bath of modes long before (t_0) and long after (t_1) the interaction takes place.

Any arbitrary system operator A evolves in time according to the Heisenberg equation $\partial_t A = i\left[H_{\mathrm{JC1}} + H_{\mathrm{JC2}} + H_{\mathrm{WG}} + H_{\mathrm{ext}} + H_{\mathrm{int}}, A\right]$, where the Hamiltonian of the system is given by the sum of five terms. These terms include two Jaynes-Cummings Hamiltonians corresponding to different modes of the cavity (H_{JC1} and H_{JC2}), the waveguides bath field Hamiltonian (H_{WG}), the external bath field Hamiltonian (H_{ext}), and the cavity-waveguide interaction Hamiltonian (H_{int}). Employing the rotating wave and second Markov approximations, these Hamiltonian terms can be expressed as follows ($\hbar = 1$):

$$
\begin{aligned}
H_{\mathrm{JC1}} &= \omega_b a_b^\dagger a_b + \omega_1 \sigma_{33} + g_b\left(a_b\sigma_{31} + a_b^\dagger\sigma_{13}\right)\\
H_{\mathrm{JC2}} &= \omega_r a_r^\dagger a_r + \left[\omega_1 - \omega_2\right]\sigma_{22} + g_r\left(a_r\sigma_{32} + a_r^\dagger\sigma_{23}\right)\\
H_{\mathrm{WG}} &= \frac{1}{\sqrt{2\pi}}\int_{-\infty}^{\infty} d\omega'\omega'\left(b^\dagger\left(\omega'\right)b\left(\omega'\right) + r^\dagger\left(\omega'\right)r\left(\omega'\right)\right)\\
H_{\mathrm{ext}} &= \frac{1}{\sqrt{2\pi}}\int_{-\infty}^{\infty} d\omega'\omega'\left(e^\dagger\left(\omega'\right)e\left(\omega'\right) + e^\dagger\left(\omega'\right)e\left(\omega'\right)\right)\\
H_{\mathrm{int}} &= \frac{1}{\sqrt{2\pi}}\int_{-\infty}^{\infty} d\omega'\left(\begin{array}{l}\sqrt{\kappa_b}\left[a_b b^\dagger\left(\omega'\right) + a_b^\dagger b\left(\omega'\right)\right] + \sqrt{\kappa_r}\left[a_r r^\dagger\left(\omega'\right) + a_r^\dagger r\left(\omega'\right)\right]\\ + \sqrt{\Gamma_{13}}\left[\sigma_{13}e^\dagger\left(\omega'\right) + \sigma_{13}^\dagger e\left(\omega'\right)\right] + \sqrt{\Gamma_{23}}\left[\sigma_{23}e^\dagger\left(\omega'\right) + \sigma_{23}^\dagger e\left(\omega'\right)\right]\end{array}\right)
\end{aligned}
\tag{2.2}
$$

In the above expression $\omega_{1,2}$ are the atomic transition frequencies and $\sigma_{ij} = |i\rangle\langle j|$ is the atomic transition operator that takes the emitter from state $|j\rangle$ to $|i\rangle$ where $i, j = 1, 2, 3$. Additionally, a_b (a_r) and ω_b (ω_r) are annihilation operator and resonance frequency of the blue (red) cavity. Furthermore, Γ_{13} and Γ_{23} represent the decay rate due to spontaneous emission from the excited state to the ground states $|1\rangle$ and $|2\rangle$, respectively. Substituting equations 2.1 and 2.2 into the Heisenberg equation gives the following set of optical Bloch equations governing the dynamics of the system:

$$
\begin{aligned}
\partial_t a_b &= \left(-i\omega_b - \frac{\kappa_b}{2}\right) a_b - i g_b \sigma_{13} - i\sqrt{\kappa_b} b_{in} \\
\partial_t a_r &= \left(-i\omega_r - \frac{\kappa_r}{2}\right) a_r - i g_r \sigma_{23} \\
\partial_t \sigma_{13} &= \left(-i\omega_1 - \frac{\Gamma_{13}+\Gamma_{23}}{2}\right) \sigma_{13} + i g_b a_b \left(\sigma_{33} - \sigma_{11}\right) - i g_r a_r \sigma_{12} \\
\partial_t \sigma_{23} &= \left(-i\omega_2 - \frac{\Gamma_{13}+\Gamma_{23}}{2}\right) \sigma_{23} + i g_r a_r \left(\sigma_{33} - \sigma_{22}\right) - i g_b a_b \sigma_{12}^{\dagger} \\
\partial_t \sigma_{12} &= -i\left[\omega_1 - \omega_2\right] \sigma_{12} + i g_b a_b \sigma_{23}^{\dagger} - i g_r a_r^{\dagger} \sigma_{13}
\end{aligned}
\tag{2.3}
$$

Additionally, since r and e modes are initially in vacuum state, the input-output relations are given by:

$$
b_{out} = b_{in} - i\sqrt{\kappa_b} a_b, \qquad r_{out} = -i\sqrt{\kappa_r} a_r, \qquad e_{out} = -i\sqrt{\Gamma_{13}} \sigma_{13} - i\sqrt{\Gamma_{23}} \sigma_{23} \tag{2.4}
$$

To study the single photon transport in the photon subtractor, we consider a single photon of frequency k to be sent to the blue input mode b_{in}. The following elements of the scattering matrix $\mathbf{S}$ can be used to calculate the probability of the photon to be reflected back to the blue waveguide (b_{out} output mode), the probability to be diverted to the red waveguide (r_{out} output mode), and the probability to be emitted to free space (e_{out} output mode):

$$
\begin{aligned}
{}_b\left\langle p\right| \mathbf{S} \left|k\right\rangle_b &= {}_b\left\langle p^- \middle| k^+ \right\rangle_b = \left\langle 0,1\right| b_{out}\left(p\right) b_{in}^{\dagger}\left(k\right) \left|0,1\right\rangle \\
{}_r\left\langle p\right| \mathbf{S} \left|k\right\rangle_b &= {}_r\left\langle p^- \middle| k^+ \right\rangle_b = \left\langle 0,2\right| r_{out}\left(p\right) b_{in}^{\dagger}\left(k\right) \left|0,1\right\rangle \\
{}_e\left\langle p\right| \mathbf{S} \left|k\right\rangle_b &= {}_e\left\langle p^- \middle| k^+ \right\rangle_b = \left\langle 0,1\right| e_{out}\left(p\right) b_{in}^{\dagger}\left(k\right) \left|0,1\right\rangle + \left\langle 0,2\right| e_{out}\left(p\right) b_{in}^{\dagger}\left(k\right) \left|0,1\right\rangle
\end{aligned}
\tag{2.5}
$$

in which $\left|k^{\pm}\right\rangle_{\alpha}$ for $\alpha = b, r, e$ are scattering eigenstates that evolve in interaction picture from distant past and future in the blue waveguide, red waveguide, and external bath, respectively. Also, states $\left|0,1\right\rangle$ and $\left|0,2\right\rangle$ both represent vacuum states but with different emitter components. The first one has the emitter in state $\left|1\right\rangle$, while for the latter the emitter is in state $\left|2\right\rangle$. Taking Fourier transforms of the input-output relations given in equation 2.4, and then substituting the results into the above equation, one obtains:

$$
\begin{aligned}
{}_b\left\langle p^- \middle| k^+ \right\rangle_b &= \delta\left(k-p\right) - i\sqrt{\kappa_b} \left\langle 0,1\right| a_b\left(p\right) \left|k^+\right\rangle_b \\
{}_r\left\langle p^- \middle| k^+ \right\rangle_b &= -i\sqrt{\kappa_r} \left\langle 0,2\right| a_r\left(p\right) \left|k^+\right\rangle_b \\
{}_e\left\langle p^- \middle| k^+ \right\rangle_b &= -i\sqrt{\Gamma_{13}} \left\langle 0,1\right| \sigma_{13}\left(p\right) \left|k^+\right\rangle_b - i\sqrt{\Gamma_{23}} \left\langle 0,2\right| \sigma_{23}\left(p\right) \left|k^+\right\rangle_b
\end{aligned}
\tag{2.6}
$$

To calculate the above matrix elements, one needs to sandwich the Bloch equations given in equation 2.3 between $\langle 0,1|$ (or $\langle 0,2|$) and $|k^+\rangle_b$ states giving the following closed set of equations:

$$\begin{cases} \partial_t \langle 0,1|\, a_b|k^+\rangle_b = \left(-i\omega_b - \frac{\kappa_b}{2}\right) \langle 0,1|\, a_b|k^+\rangle_b - ig_b \langle 0,1|\, \sigma_{13}|k^+\rangle_b - i\sqrt{\kappa_b}\, \langle 0,1|\, b_{in}|k^+\rangle_b \\ \partial_t \langle 0,1|\, \sigma_{13}|k^+\rangle_b = \left(-i\omega_1 - \frac{\Gamma_{13}+\Gamma_{23}}{2}\right) \langle 0,1|\, \sigma_{13}|k^+\rangle_b - ig_b \langle 0,1|\, a_b|k^+\rangle_b - ig_r \langle 0,1|\, a_r\sigma_{12}|k^+\rangle_b \\ \partial_t \langle 0,1|\, a_r\sigma_{12}|k^+\rangle_b = \left(-i\left[\omega_1 - \omega_2\right] + \left(-i\omega_r - \frac{\kappa_r}{2}\right)\right) \langle 0,1|\, a_r\sigma_{12}|k^+\rangle_b - ig_r \langle 0,1|\, \sigma_{13}|k^+\rangle_b \\ \partial_t \langle 0,2|\, a_r|k^+\rangle_b = \left(-i\omega_r - \frac{\kappa_r}{2}\right) \langle 0,2|\, a_r|k^+\rangle_b - ig_r \langle 0,2|\, \sigma_{23}|k^+\rangle_b \\ \partial_t \langle 0,2|\, \sigma_{23}|k^+\rangle_b = \left(-i\omega_2 - \frac{\Gamma_{13}+\Gamma_{23}}{2}\right) \langle 0,2|\, \sigma_{23}|k^+\rangle_b - ig_r \langle 0,2|\, a_r|k^+\rangle_b - ig_b \langle 0,2|\, a_b\sigma_{12}^\dagger|k^+\rangle_b \\ \partial_t \langle 0,2|\, a_b\sigma_{12}^\dagger|k^+\rangle_b = \left(i\left[\omega_1 - \omega_2\right] + \left(-i\omega_b - \frac{\kappa_b}{2}\right)\right) \langle 0,2|\, a_b\sigma_{12}^\dagger|k^+\rangle_b - ig_b \langle 0,2|\, \sigma_{23}|k^+\rangle_b \\ \qquad\qquad -i\sqrt{\kappa_b}e^{i(\omega_1-\omega_2)t}\, \langle 0,1|\, b_{in}|k^+\rangle_b \end{cases} \tag{2.7}$$

The derived equations are specific to the case of single-photon transport, where assuming the existence of only a single excitation in the entire system leads to the elimination of certain terms. Substituting $\langle 0,1|\, b_{in}\,(t)\,|k^+\rangle_b = \left(1/\sqrt{2\pi}\right) e^{-ikt}$, in the above equations, taking Fourier transform and solving for $\langle 0,1|\, a_b\,(p)\,|k^+\rangle_b$, $\langle 0,2|\, a_r\,(p)\,|k^+\rangle_b$, $\langle 0,1|\, \sigma_{13}\,(p)\,|k^+\rangle_b$, and $\langle 0,2|\, \sigma_{23}\,(p)\,|k^+\rangle_b$, then substituting the results back into equation 2.6, gives:

$$\begin{aligned} {}_b\langle p^-\mid k^+\rangle_b &= r_k\delta\left(k-p\right) \\ {}_r\langle p^-\mid k^+\rangle_b &= t_k\delta\left(k-p-\left(\omega_1-\omega_2\right)\right) \\ {}_e\langle p^-\mid k^+\rangle_b &= s_k^1\delta\left(k-p\right) + s_k^2\delta\left(k-p-\left(\omega_1-\omega_2\right)\right) \end{aligned} \tag{2.8}$$

in which:

$$r_k = \frac{\left(k-\omega_b-i\frac{\kappa_b}{2}\right)\left(k-\omega_1-\frac{{g_r}^2}{\left(k-\omega_r-(\omega_1-\omega_2)+i\frac{\kappa_r}{2}\right)}+\frac{1}{2}i\left(\Gamma_{13}+\Gamma_{23}\right)\right)-{g_b}^2}{D}$$

$$t_k = -\frac{i\sqrt{\kappa_b\kappa_r}g_bg_r}{D\left(k-\omega_r-(\omega_1-\omega_2)+i\frac{\kappa_r}{2}\right)} \qquad s_k^1 = -\frac{ig_b\sqrt{\Gamma_{13}\kappa_b}}{D} \qquad s_k^2 = -\frac{ig_b\sqrt{\Gamma_{23}\kappa_b}}{D} \tag{2.9}$$

The term D, which appears in the denominator of the above expressions, is given by:

$$D = \left(k-\omega_b+i\frac{\kappa_b}{2}\right)\left(k-\omega_1-\frac{{g_r}^2}{\left(k-\omega_r-(\omega_1-\omega_2)+i\frac{\kappa_r}{2}\right)}+\frac{1}{2}i\left(\Gamma_{13}+\Gamma_{23}\right)\right)-{g_b}^2 \tag{2.10}$$

In equation 2.9, r_k is the reflectivity of the system, which relates the incoming field amplitude in the blue waveguide to the amplitude of the field reflected to the same waveguide. t_k is the transmissivity, representing the ratio of the field successfully transmitted to

the red waveguide to the incoming field amplitude. Additionally, s_k^i gives the amplitude of the emitted field to free space, resulting in leaving the emitter in the ground state $|i\rangle$. Based on these results, when a photon of frequency k is sent to the blue input mode of the proposed scheme, it can interact with the atom-cavity system in one of the following four different ways. It is either reflected with probability $P_1 = |r_k|^2$, or transmitted to the red mode with probability $P_2 = |t_k|^2$, or emitted to free space through spontaneous decay of the atom to level $|1\rangle$ with probability $P_3 = |s_k^1|^2$, or emitted to free space leaving the atom in state $|2\rangle$ with probability $P_4 = |s_k^2|^2$.

Now, consider the case where, instead of a single-frequency photon, a single-photon pulse with a carrier frequency k_c is sent to the subtractor as the input. The Fourier transform $f(\omega)$ of the field in this case exhibits a distribution around the center frequency k_c in the frequency domain. Since, in the single-photon regime, the system behaves linearly, using the superposition principle, the probabilities P_1 to P_4 defined above can be obtained by calculating the following integrals over the entire frequency interval:

$$\begin{aligned} P_1 &= \int_{-\infty}^{+\infty} |r_\omega f(\omega)|^2 d\omega \qquad P_2 = \int_{-\infty}^{+\infty} |t_\omega f(\omega)|^2 d\omega \\ P_3 &= \int_{-\infty}^{+\infty} \left|s_\omega^1 f(\omega)\right|^2 d\omega \qquad P_4 = \int_{-\infty}^{+\infty} \left|s_\omega^2 f(\omega)\right|^2 d\omega \end{aligned} \tag{2.11}$$

2.1.2 Results and discussion

As a first step in evaluating the photon subtractor's performance, we need to define the conditions under which we consider photon subtraction successful or unsuccessful. An ideal deterministic photon subtractor should precisely subtract one photon from the input pulse, irrespective of the total number of photons it contains. Therefore, for the specific case of a single-photon input in the proposed scheme of Figure 2.1, there should be no photon in the reflected output mode b_{out} for subtraction to be deemed successful. If this condition is met, it indicates that the photon has either been emitted by the atom into free space or transmitted to the red output mode r_{out}. Since, in various applications of photon subtractors, the subtracted photon often needs to be detected by a photon detector, we will consider the former case a failure. Note that this may not necessarily be the case for certain applications, such as when the state created by photon subtraction is the intended outcome. However, for instance, a PNR detector can be implemented by cascading several photon subtractors and, in this case, accurate photon counting would rely on detecting all

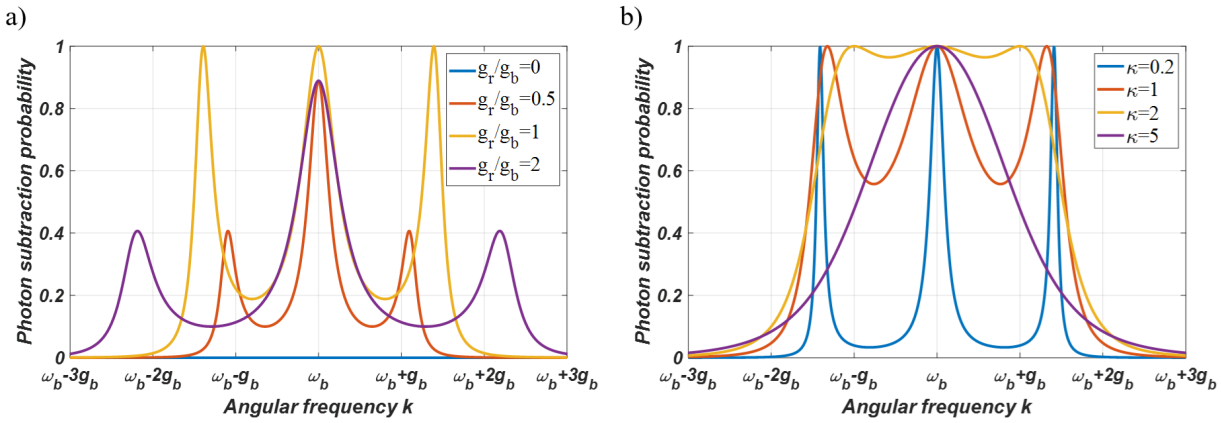


Figure 2.2: Probability of successful photon subtraction ($P_2 = |t_k|^2$) with respect to the angular frequency of the arriving photon, illustrating (a) the effect of the ratio of coupling strengths of different modes ($\kappa_b/g_b = \kappa_r/g_r = 0.5$), and (b) the effect of the cavities' decay rate ($g_r/g_b = 1$ and $\kappa_b/g_b = \kappa_r/g_r = \kappa$).

subtracted photons by each photon subtractor. Another example is when the subtractor is used in single photon splitting attacks on QKD, where the subtracted photon contains communicated information and its successful collection is crucial. Consequently, we define the success probability of our photon subtractor as the probability that the photon is successfully transmitted to the red mode, denoted as P_2 in equation 2.11 and the explanation above it.

Figure 2.2 depicts this success probability with respect to the angular frequency k of a single-frequency photon sent as input. In parts (a) and (b) of this figure, effects of the ratio of coupling strengths of different modes of the cavity, i.e., g_r/g_b, and the ratio of the decay rates of modes to their corresponding coupling strengths, i.e., $\kappa_{b(r)}/g_{b(r)}$, are shown, respectively. The results presented in this figure assume perfect resonance between the cavity modes and their respective emitter transitions, i.e., $\omega_b = \omega_1$ and $\omega_r = \omega_2$. Additionally, to better distinguish the effects of different parameters on the system's response, the spontaneous decay has been assumed to be negligible (i.e., $\Gamma_{13} = \Gamma_{23} = 0$). It should be noted that this assumption is not a requirement for the system or the analysis, as the impact of spontaneous emission is analyzed separately in the next figure. As depicted in Figure 2.2.(a), a success probability of unity can only be achieved in a device with a symmetric bimodal cavity, where the coupling strengths of different modes, as well as their decay rates, are equal. This happens because under this condition, at the same rate that photons enter the blue cavity and excite the emitter, the emitter is de-excited to the second

ground state, emitting photons to the red mode, which then leave the red cavity mode, resulting in no photon being re-emitted to the blue cavity mode. If this condition holds, photons with three different frequencies will be transmitted completely: those in resonance with the blue cavity and two others, one slightly above and one slightly below the resonance frequency. As the decay rates of the cavities tend toward zero, these side peaks occur at $k = \omega_b \pm \sqrt{2}g_b$, while increasing the decay rates makes them approach the center peak at ω_b, forming a cubed Lorentzian lineshape centered at ω_b. This can be clearly observed in Figure 2.2.(b), where the effect of decay rates on the frequency response is illustrated.

To understand the origin of the existence of these three peaks in the system's transmissivity, we need to investigate the dressed states of our bimodal atom-cavity system. These dressed states are the eigenstates of the Hamiltonian $H = H_{\text{JC1}} + H_{\text{JC2}}$, where the Jaynes-Cummings Hamiltonians H_{JC1} and H_{JC2} are as defined in equation 2.2. Considering the case with n exctations in the system, the Hamiltonian can be expressed in the basis $\{|1, n, 0\rangle, |2, n-1, 1\rangle, |3, n-1, 0\rangle\}$, where the three numbers used in the representation of the states denote the emitter state, the number of photons in the blue cavity, and the number of photons in the red cavity, respectively. It should be noted that, as the input light is applied to the blue cavity, states with more than one photon in the red cavity do not appear in the overall quantum state of the system. Therefore, there is no need to take them into account in our analysis. Eigendecomposition of the Hamiltonian gives the following dressed states and their corresponding energies for the case where the cavity modes are in perfect resonance with the emitter ($\omega_b = \omega_1$ and $\omega_r = \omega_2$):

$$
\begin{aligned}
|\psi_{n,1}\rangle &= \frac{1}{\sqrt{2\left(ng_b^2 + g_r^2\right)}}\left(\sqrt{n}g_b\,|1, n, 0\rangle + g_r\,|2, n-1, 1\rangle - \sqrt{ng_b^2 + g_r^2}\,|3, n-1, 0\rangle\right) \\
|\psi_{n,2}\rangle &= \frac{1}{\sqrt{ng_b^2 + g_r^2}}\left(g_r\,|1, n, 0\rangle - \sqrt{n}g_b\,|2, n-1, 1\rangle\right) \\
|\psi_{n,3}\rangle &= \frac{1}{\sqrt{2\left(ng_b^2 + g_r^2\right)}}\left(\sqrt{n}g_b\,|1, n, 0\rangle + g_r\,|2, n-1, 1\rangle + \sqrt{ng_b^2 + g_r^2}\,|3, n-1, 0\rangle\right) \\
E_{n,1} &= n\omega_b - \sqrt{ng_b^2 + g_r^2}, \qquad E_{n,2} = n\omega_b, \qquad , E_{n,3} = n\omega_b + \sqrt{ng_b^2 + g_r^2}
\end{aligned}
\tag{2.12}
$$

The above results for $n = 1$ confirm both the existence and location of the three peaks observed in the transmissivity of the system in our single-excitation analysis and when the cavity decay rates tend toward zero. The increase in the decay rates of the cavities is equivalent to a decrease in effective atom-cavity coupling strengths, justifying the decrease in resonance frequency splitting and the approach of the side peaks to the one at the center, as seen in Figure 2.2.(b). The structure of the dressed states reveals that the middle state

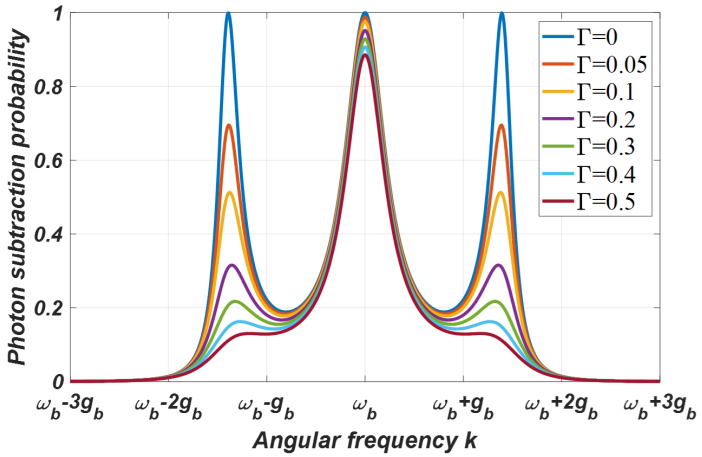


Figure 2.3: Effect of spontaneous decay of the emitter on the probability of successful photon subtraction ($g_r = g_b$, $\kappa_b/g_b = \kappa_r/g_r = 0.5$, $\Gamma_{13}/g_b = \Gamma_{23}/g_r = \Gamma$).

belongs to a manifold of equally spaced dark states, each corresponding to a different number of excitations. Consequently, when the excitation frequency is near the resonance frequency ω_b, the contribution of the atomic excited state becomes negligible, allowing the system's dynamics to be effectively analyzed within this manifold. Restricting the system to this manifold reduces the number of operators governing the system's dynamics, thereby simplifying the Bloch equations, which is particularly beneficial for multi-photon transport analysis.

The effect of spontaneous decay rates of the atom on the success probability of the photon subtractor is depicted in Figure 2.3. According to this figure, spontaneous decay of the atom results in a decrease in the photon subtraction probability, as expected. However, the important point is that while this decrease is smaller at the central peak of the frequency response, it highly suppresses the side peaks. The reason can be deduced from the dressed states given in equation 2.12. The second dressed state which corresponds to the central peak is a superposition of states with emitter parts in ground energy levels, meaning that at this frequency the excited atomic state is not populated during the population transfer between the ground states. This results in zero emitter sponatenous emission regardless of the magnitude of emitter decay rates. However, it should be noted that these results are for the undamped resonating system (zero cavity decay), justyfying the slight decrease in the central peak amplitude in Figure 2.3. On the other hand, the other two dressed states have the excited atomic level as a part of their superposition, meaning that the excited state is populated at the two side peak frequencies. Therefore, as the emitter decay rate

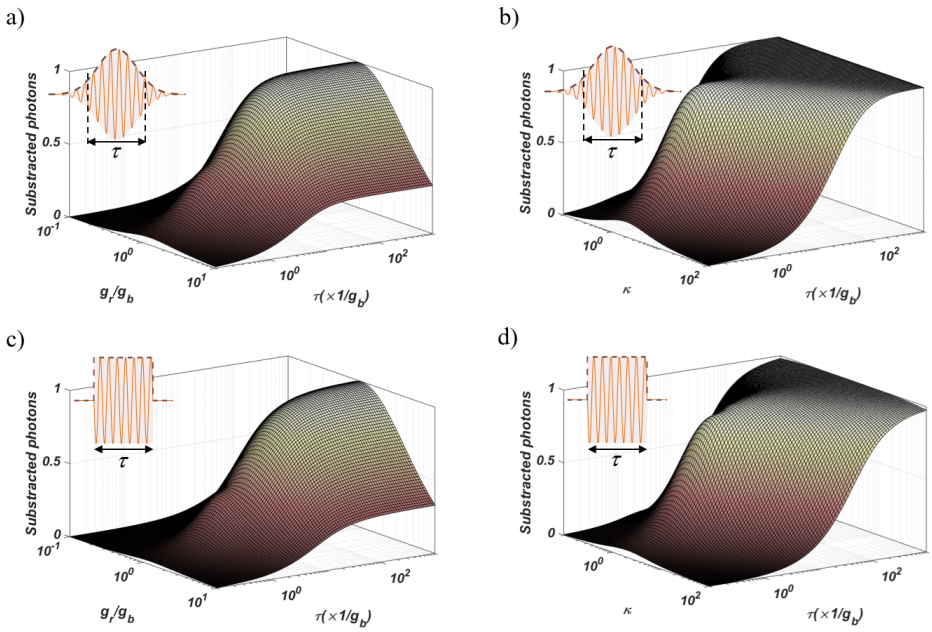


Figure 2.4: Probability of successful photon subtraction from pulsed input light: (a) Gaussian input ($\kappa = 0.5$), (b) Gaussian input ($g_r/g_b = 1$), (c) rectangular input ($\kappa = 0.5$), and (d) rectangular input ($g_r/g_b = 1$).

increases, the excitation most probably leaves the system through spontaneous decay of the emitter, resulting in what we defined as failure of the photon subtraction process.

Figures 2.2 and 2.3 offer insights into the system's ability to subtract single-frequency photons or equivalently single-photon pulses of infinite duration. In practical applications, however, it is essential to subtract photons from input pulses with finite time durations which are composed of a continuum of frequencies. In the single photon regime, this frequency responses can still be used to calculate system's response to pulsed input light as described in equation 2.11. To assess the performance of our photon subtractor in the pulsed regime, we examine the system's response to pulses with two distinct temporal shapes: a Gaussian pulse and an ideal rectangular pulse. Figure 2.4 illustrates the probability of successfully subtracting the photon contained in single-photon pulses of each shape. It should be noted that, due to the self-terminating nature of the process, as explained in the introduction section, no more than one photon can be subtracted. Therefore, the y-axis of Figures 2.4 to 2.8, which corresponds to the mean number of subtracted photons, effectively represents the probability that a single photon is subtracted. The graphs are plotted versus the pulse duration τ, which, for the Gaussian pulse, is defined as the full-

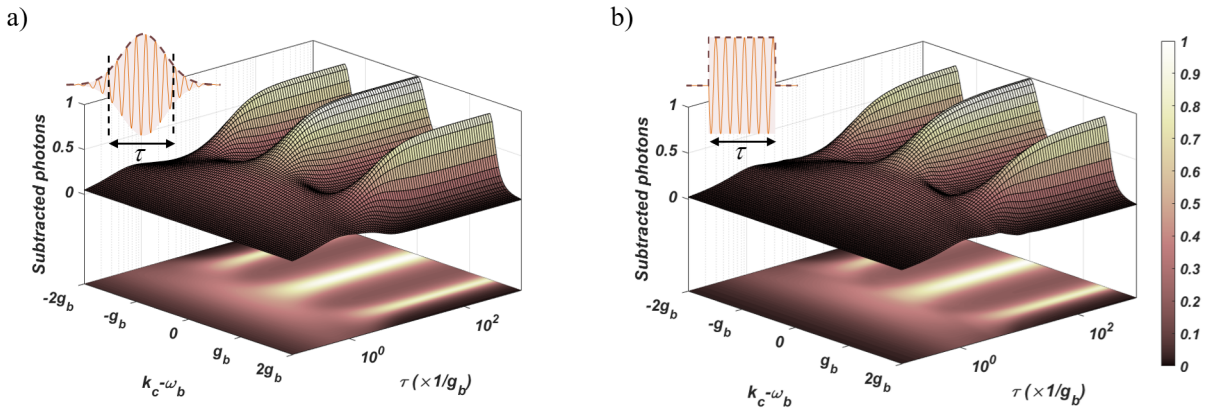


Figure 2.5: Probability of successful photon subtraction from detuned pulsed input light: (a) Gaussian input, and (b) rectangular input ($g_r = g_b$, $\kappa_b/g_b = \kappa_r/g_r = 0.5$, $\Gamma_{13}/g_b = \Gamma_{23}/g_b = 0.02$).

width at half maximum (FWHM) of the power amplitude, the coupling strength ratio g_r/g_b and the dimensionless decay rate κ of the cavities. It's evident from this figure that in the single-photon regime, a bimodal cavity with equal coupling strengths at different modes is crucial for achieving a photon subtraction probability approaching unity. However, while this probability can approach unity for long input pulses regardless of the cavity decay rate κ, this parameter needs to be optimized for pulses of medium duration to maximize the success probability. In the results shown in this figure, we assume that the carrier frequency k_c of the pulses is in resonance with the blue mode of the cavity and the atomic spontaneous decay is negligible.

Figure 2.5 illustrates the impact of detuning the input pulse from the cavity resonance frequency on the performance of the photon subtractor. As anticipated from the frequency responses, for sufficiently long pulses with narrow frequency content, the plots feature three peaks, one at zero detuning and two side peaks corresponding to the other two dressed energy levels. However, for short pulses, not only does the success probability decrease dramatically, but the three peaks are also combined, resulting in a single broad peak at zero detuning frequency. To better understand why the success probability is higher for long pulses, it is important to consider two key factors affecting the device's performance: first, whether the single photons in the input pulse can successfully enter the cavity, and second, whether they can successfully excite the atom before decaying back out of the cavity. The first factor depends on the coupling strength of the cavity field to the waveguide field and improves as the decay rate increases. In contrast, the second factor depends on the ratio of

the atom-cavity coupling strength to the cavity decay rate and diminishes with increasing decay rate. Additionally, when the input pulses are longer, the photon has more time to enter the cavity due to the limited cavity decay rate, while the probability of exciting the atom remains unaffected by the pulse length. As a result of these effects, as shown in Figure 2.5, increasing the pulse length enhances the success rate of the photon subtractor. The effect of the pulse length can also be understood from a frequency-domain perspective, where longer pulses have narrower frequency content, aligning more effectively with the peak of the system's frequency response.

2.2 Numerical Simulations and Results

The analytical results derived in the previous section can be verified through numerical simulation of the system. Moreover, numerical simulations allow the investigation of the system's response to multi-photon inputs. A general solution involves simulating the interaction of the emitter-cavity system with an infinite continuum of waveguide modes, which is practically impossible. However, when the traveling light in the waveguide can be discretized into a finite number of wave packets, each occupied by quantum states with a finite number of photons, it becomes possible to reduce the problem to a finite-dimensional one. In this method, neglecting the propagation time of the pulses in the waveguide leads to a Markovian system where each input or output wave packet is treated as a single oscillator with a time-dependent coupling (according to its temporal shape) to the local quantum system (the bimodal atom-cavity in our case). Additionally, the input-output formalism can be utilized to introduce Lindblad operators representing the system's collapses, resulting in the emission of photons at the system's outputs.

Since we are solely concerned with the photon statistics at the outputs of the system, we model only the input wave packet as an oscillator, while introducing two Lindblad operators corresponding to the two outputs of the system (L_1 and L_2). Additionally, L_3 and L_4 are responsible for spontaneous decay of the atom. According to section 1.2.2, the total Hamiltonian of such a system and the collapse operators are as follows:

$$\begin{aligned} H &= (k_c - \omega_b)\, a_u^\dagger a_u + i\left[g_b^* a_b^\dagger \sigma_{13} + g_r^* a_r^\dagger \sigma_{23} + \tfrac{1}{2}\sqrt{\kappa_b} g_u(t)\, a_u^\dagger a_b - H.c.\right] \\ L_1 &= \sqrt{\kappa_b} a_b + g_u^*(t) a_u \qquad L_2 = \sqrt{\kappa_r} a_r \qquad L_3 = \sqrt{\Gamma_{13}}\sigma_{13} \qquad L_4 = \sqrt{\Gamma_{23}}\sigma_{23} \end{aligned} \tag{2.13}$$

where $g_u(t)$ is as given in equation 1.12, with $u(t)$ being the temporal envelope of the input pulse. The Hamiltonian is formulated under the assumption that the cavity modes precisely match their corresponding atomic transitions, and it is expressed in frames rotating with these resonance frequencies. The subsequent system simulation will involve

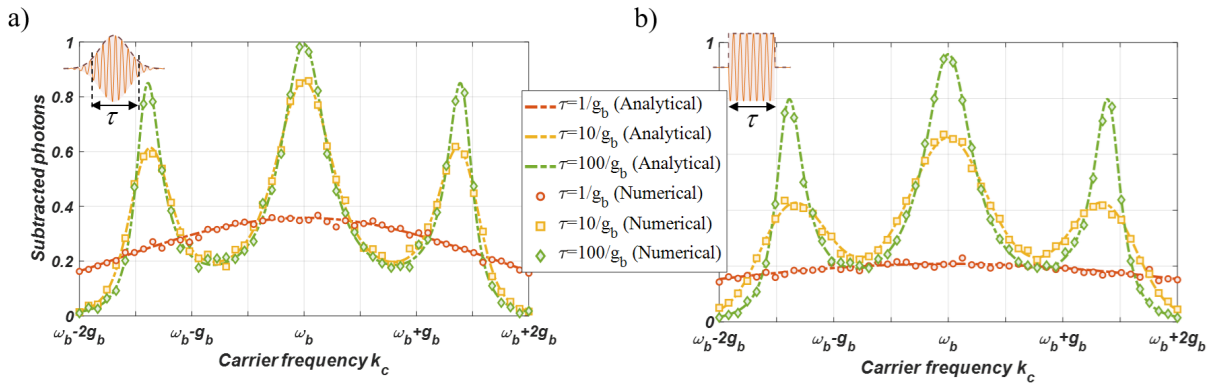


Figure 2.6: Comparison of analytical and numerical solutions to the system's response in the pulsed regime: (a) Gaussian pulse, and (b) Rectangular pulse ($g_r = g_b$, $\kappa_b/g_b = \kappa_r/g_r = 0.5$, $\Gamma_{13}/g_b = \Gamma_{23}/g_b = 0.02$).

numerically solving the master equation using the quantum trajectory approach, based on the Hamiltonian and Lindblad operators introduced above.

Figure 2.6 presents a comparison between analytical and numerical results in the single-photon regime. The solid lines correspond to the results from the analytical closed-form solution given in equations 2.9 to 2.11, while the markers depict the outcomes obtained through the above-described numerical simulation. The results show a remarkable agreement between the analytical and numerical methods.

To assess how effectively our single-photon model can predict the behavior of the system in the multi-photon regime, we conducted numerical simulations using input pulses occupied by Fock states with different numbers of photons. The results are depicted in Figure 2.7 for a rectangular pulse with $\tau = 10/g_b$. As shown in this figure, increasing the number of arriving photons enhances the probability of photon subtraction. However, the overall behavior of the system in the frequency domain remains consistent, exhibiting three peaks. The impact of the number of arriving photons on the amplitude and shape of these peaks differs. For the side peaks, while increasing the number of photons from one to two significantly enhances the success probability, further increases do not alter either the amplitude or the shape of the peak. This can be justified based on the energy level structure derived in equation 2.12. In essence, the non-uniform frequency splitting of the dressed energy levels leads to a photon blockade effect for pulses resonating with one of the side dressed states of the single-excitation level. Consequently, sending pulses with more photons initially boosts the success probability due to the possible spontaneous decay of the emitter from state $|3\rangle$ to $|1\rangle$ (in case of sponataneous decay there is another photon

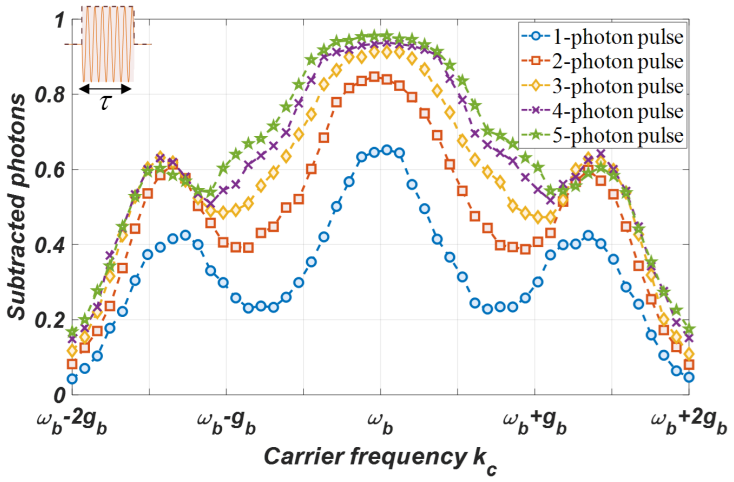


Figure 2.7: Probability of successful photon subtraction from light pulses containing different number of photons ($g_r = g_b$, $\kappa_b/g_b = \kappa_r/g_r = 0.5$, $\Gamma_{13}/g_b = \Gamma_{23}/g_b = 0.02$).

to enter the cavity and interact with the emitter). Further increases in the number of photons have no effect since no more than one photon can enter the cavity at these side frequencies. However, the situation differs for the central peak. Unlike the side peaks, there is no photon blockade effect at this frequency. Consequently, increasing the number of incoming photons can lead to more photons entering the cavity. Thus, even at frequencies slightly detuned from the peak frequency, at least one photon would be able to enter the cavity, enabling photon subtraction. This results in the widening of the peak shape at higher numbers of photons, as shown in the figure. However, the success probability saturates at an amplitude smaller than one due to the spontaneous decay of the emitter from state $|3\rangle$ to $|2\rangle$, resulting in the termination of the interaction and the failure of the photon subtraction process, regardless of the number of photons present at the input.

Depending on the application, the subtracted photon (red output port), the remaining photons (blue output port), or both may be the primary focus or require detection. For instance, a PNR detector can be implemented by cascading photon subtractors in a daisy-chain configuration where the blue output port of each subtractor is routed to the input port of the next block, as will be discussed in chapter 4. In this scheme, the red output port of each subtractor is monitored by a single-photon detector, and the number of clicks registered by the detectors corresponds to the number of photons in the input pulse. In the PNS attack application, the subtracted photon from the input pulse sent by the first party is directed to the eavesdropper for measurement to extract the communicated data, while the remaining photons are forwarded to the second party (see chapter 5). When the

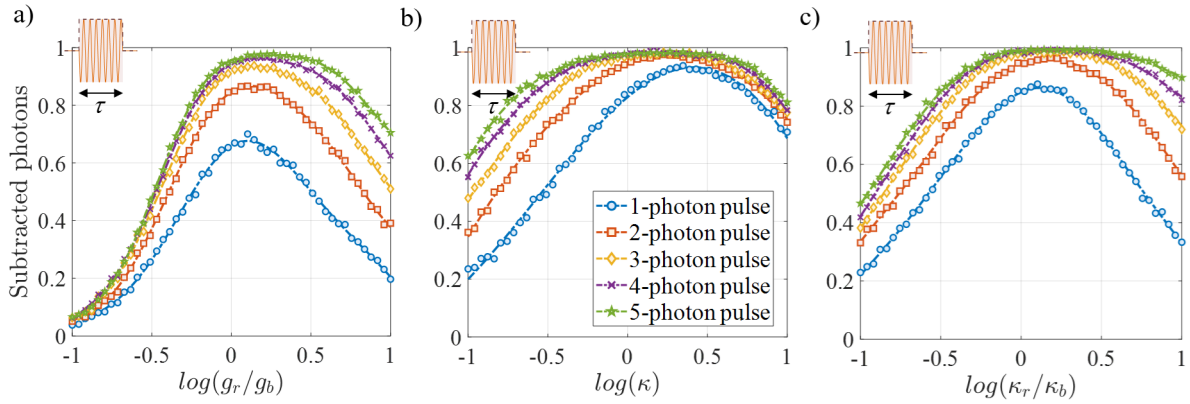


Figure 2.8: Effect of (a) coupling strength ratio ($\kappa_b/g_b = \kappa_r/g_r = 0.5$, $\Gamma_{13}/g_b = \Gamma_{23}/g_b = 0.02$), (b) decay rate of cavities ($g_r = g_b$, $\kappa_b/g_b = \kappa_r/g_r = \kappa$, $\Gamma_{13}/g_b = \Gamma_{23}/g_b = 0.02$), and (c) ratio of decay rates in different modes ($g_r = g_b$, $\kappa_b/g_b = 0.5$, $\Gamma_{13}/g_b = \Gamma_{23}/g_b = 0.02$) on photon subtraction probability from pulses with different number of photons.

photon subtractor is used to generate non-Gaussian states of light, the output pulse from the blue port contains the generated quantum state, while the single photon leaving the red port, as mentioned above, can be used for post-selection purposes.

Figure 2.8 illustrates how the main design parameters of the cavity, including the ratio of coupling strengths of different modes and their decay rates, affect the probability of successful photon subtraction when the input pulse contains more than one photon. The results shown in this figure are for pulses again with $\tau = 10/g_b$ and resonating with the blue mode of the cavity, i.e., on the central peak of Figure 2.7. As depicted in this figure, while in the single-photon regime the curves exhibit a sharp peak at which the success probability is maximized, the peaks start widening as the number of input photons increases, enabling efficient photon subtraction over a broader range of parameters. Based on these results, when the input is a multi-photon pulse, successful photon subtraction not only occurs at the peak location of the single-photon curves but can also occur at higher g_r/g_b and lower κ values. This is because in the multi-photon regime, more than one photon can enter the cavity, resulting in a higher Rabi frequency in the blue mode. Moreover, when more than one photon is present at the input, the probability that one of them successfully enters the cavity remains high, even at low cavity decay rates. Figure 2.8.(c) shows that as the number of input photons increases, a higher decay rate for the red cavity becomes more favorable compared to the blue cavity. The important point regarding Figure 2.8 is that optimized parameters based on the single-photon pulse results lead to efficient performance of the system regardless of the number of photons at the input. Therefore, the results of

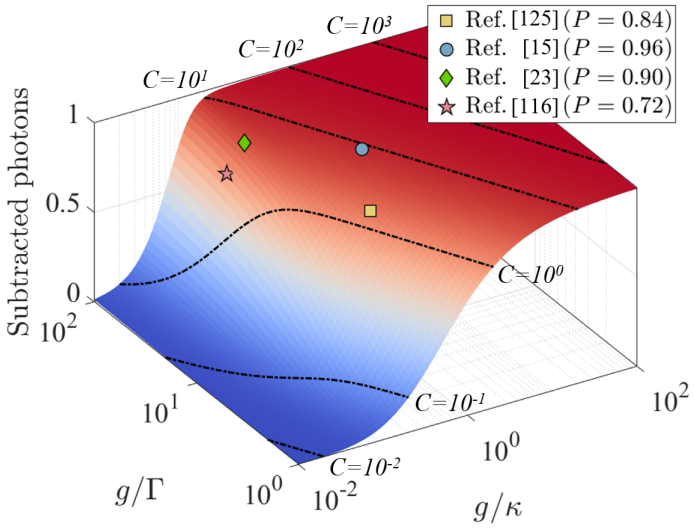


Figure 2.9: Probability of successful photon subtraction as a function of the coupling strength-to-cavity decay rate ratio and the coupling strength-to-atomic decay rate ratio. The two modes are assumed to be symmetric with equal parameters ($g_r = g_b = g$, $\kappa_b = \kappa_r = \kappa$, $\Gamma_{13} = \Gamma_{23} = \Gamma$). The markers indicate where different systems described in the text fall on the performance diagram, with their corresponding success probabilities denoted in the legend.

single-photon transport can be effectively used in the design process of an efficient photon subtractor.

2.3 Feasibility Study

Experimentally, cavity QED systems with multiple cavity modes interacting with a single quantum emitter have been successfully fabricated and tested [15, 62, 64, 125]. These systems serve as key components in quantum optics, enabling the realization of photonic devices where single photons in one mode either control or herald the application of a quantum operation in another mode. Efficient coupling of the cavity modes to separate waveguides is crucial for interfacing these devices and forming a quantum network [114]. To evaluate the feasibility of photon subtractor, we consider four potential waveguide-coupled cavity QED platforms based on the experimental results reported in the literature. These include atoms evanescently coupled to counterpropagating whispering-gallery modes of micro-resonators [125], cold atoms trapped in crossed optical fiber cavities [15],

quantum dots (QDs) coupled to bimodal photonic crystal cavities [23], and QDs coupled to crossed nanobeam cavities [116]. For the last two systems, the coupling strength is estimated based on the simulated mode volumes of the fabricated structures, compared with measured data from QDs in photonic crystal cavities [91]. Figure 2.9 shows the success probability of photon subtraction when a single-photon Gaussian pulse of width $\tau = 40/\kappa$ is supplied, as a function of coupling strength to cavity decay rate ratio g/κ and coupling strength to atomic decay rate ratio g/Γ. The markers on the plot represent points where these systems fall on the performance diagram. Additionally, the dash-dot contour lines indicate the loci of constant cooperativity $C = g^2/2\kappa\Gamma$.

As shown in this figure, success rates approaching unity can be achieved with both existing atom-cavity and QD-cavity structures, with atomic systems offering better overall performance. In QD-cavity systems, higher coupling strengths are achievable due to the small mode volume of photonic crystal cavities, the strong dipole moment of QD transitions, and the direct interaction of the confined field with the emitter. However, the limited quality factor of fabricated cavities constrains their performance. Since $\kappa \gg \Gamma$ in most such systems, the primary focus has been on improving the coupling-to-decay rate ratio g/κ, which largely depends on enhancing the quality factor of the cavity structures [69]. Despite better performance of cold atom setups, an important feature of solid-state platforms that makes them favorable in this context is their higher scalability and miniaturization potential, which is desirable for specific potential applications of deterministic photon subtraction, such as PNR detection, requiring multiple photon subtractors connected in a cascaded fashion [129].

Chapter 3

Non-Gaussian State Generation via Deterministic Photon Subtraction

In Section 1.1.2, we introduced the operator $\hat{s}$ as an ideal deterministic single-photon subtraction operator, capable of shifting the photon-number distribution of a quantum light pulse downward by one while preserving the temporal distribution and coherence of the remaining photons. Although the potential of this operator to generate non-Gaussian states of light was previously proposed by Höner et al. [53], no experimental scheme is currently known to accurately implement it. Similar to other schemes that subtract the first-arriving photon, the SPRINT mechanism results in a multimode output even when the input pulse is single-mode. Although this characteristic limits its ability to deterministically generate pure single-mode states, in this chapter we demonstrate that SPRINT still offers potential for non-Gaussian manipulation of quantum pulses. To this end, we perform a comprehensive analysis of the SPRINT-based photon subtraction process in a setup involving a chiral waveguide directly coupled to a Λ-type atom [120]. First, we calculate the first-order coherence matrices to extract the mode shapes present in the output pulses. Next, we use the results of the first step to model the device as a cascaded atom-cavity quantum network and determine its effective Hamiltonian and Lindblad operators. Finally, we employ the quantum trajectory method to simulate the system and derive the quantum states generated. We demonstrate that, using a conditional measurement-based scheme, non-Gaussian states can be generated directly from input Gaussian states.

3.1 System Description and Input–Output Formulation

As described in section 1.1.2, a SPRINT-based photon subtractor relies on a three-level Λ-type atom, where distinct ground-to-excited state transitions are selectively coupled to two different light modes. These modes can correspond either to separate modes of a bimodal cavity, as examined in Chapter 2, or to counterpropagating modes in a chiral waveguide [120]. Figure 3.1 schematically depicts the latter design employing a chiral waveguide which is directly interacting with the atom. Modes propagating in different directions are represented by distinct colors, with their correspondence to atomic transitions highlighted in the same color. Consider the atom initially prepared in ground state $|1\rangle$, with the input light directed towards the right propagating mode (depicted in green). During the Raman interaction, the atom first absorbs a single photon from the input light, becoming excited. Subsequently, the destructive interference between the atom's emission into the same mode as the input light causes it to decay to the other ground state [119]. This transition results in the emission of a single photon into the left propagating mode (depicted in red), effectively subtracting one photon from the input pulse in a deterministic manner.

Here we use input-output formalism to analytically study the interaction of the atom with the bath of waveguide modes during the photon subtraction process. This gives a set of differential equations governing evolution of the atomic operators $\sigma_{ij} = |i\rangle\langle j|$ in the Heisenberg picture as a function of the input operators $r_{in}(t)$ and $l_{in}(t)$:

$$\begin{aligned}
\partial_t\sigma_{11} &= \sqrt{\gamma_g}\left(\sigma_{31}r_{in} + r_{in}^\dagger\sigma_{13}\right) + \gamma_g\sigma_{33} \\
\partial_t\sigma_{22} &= \sqrt{\gamma_g}\left(\sigma_{32}l_{in} + l_{in}^\dagger\sigma_{23}\right) + \gamma_g\sigma_{33} \\
\partial_t\sigma_{33} &= -\sqrt{\gamma_g}\left(\sigma_{31}r_{in} + r_{in}^\dagger\sigma_{13}\right) - \sqrt{\gamma_g}\left(\sigma_{32}l_{in} + l_{in}^\dagger\sigma_{23}\right) - 2\gamma_g\sigma_{33} \\
\partial_t\sigma_{13} &= -i\omega_1\sigma_{13} + \sqrt{\gamma_g}\left(\sigma_{33} - \sigma_{11}\right)r_{in} - \sqrt{\gamma_g}\sigma_{12}l_{in} - \gamma_g\sigma_{13} \\
\partial_t\sigma_{23} &= -i\omega_2\sigma_{23} + \sqrt{\gamma_g}\left(\sigma_{33} - \sigma_{22}\right)l_{in} - \sqrt{\gamma_g}\sigma_{21}r_{in} - \gamma_g\sigma_{23} \\
\partial_t\sigma_{12} &= -i\left(\omega_1 - \omega_2\right)\sigma_{12} + \sqrt{\gamma_g}\sigma_{32}r_{in} + \sqrt{\gamma_g}l_{in}^\dagger\sigma_{13}
\end{aligned} \tag{3.1}$$

In the above equation ω_i is the transition frequency from the excited state to the ground state $|i\rangle$ and γ_g denotes the emission rate of the atom to the guided modes of the waveguide. In addition, the correponding inputs and outputs of the system are connected by the following relations:

$$r_{out} = r_{in} + \sqrt{\gamma_g}\sigma_{13} \qquad l_{out} = l_{in} + \sqrt{\gamma_g}\sigma_{23} \tag{3.2}$$

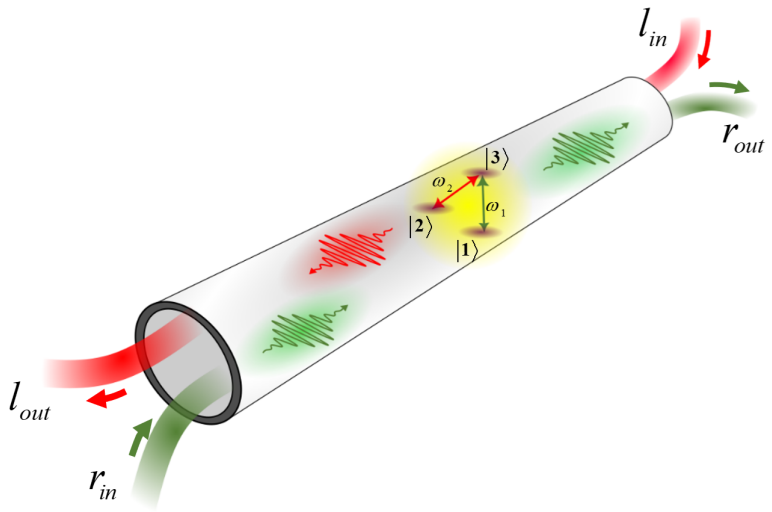


Figure 3.1: Schematic view of a Λ-type atom coupled to a chiral waveguide. The input pulse is sent to the right-propagating (green) mode, the subtracted photon is reflected to the left-propagating (red) mode, while the remaining pulse leaves the waveguide from the same mode's output.

The details on derivation of equations 3.1 and 3.2 are provided in Appendix A. We assume that the input light is sent to the r_{in} mode and l_{in} is initially in vacuum state. Also, the emitter is in its ground state $|1\rangle$ at $t = t_0$ before the light interacts with the emitter. Therefore, According to the photon subtraction scenario described above, l_{out} contains the subtracted single photon and r_{out} represents the remaing light after subtraction of a single photon.

3.2 First-Order Coherence Analysis and Temporal Mode Decomposition

In the pulsed operation regime, where both the input and output of the device consist of pulses of light with finite durations, the initial step in the quantum state analysis of the output light is to conduct a modal decomposition to distinguish the potentially involved temporal modes at each output. Consider a set of temporal modes identified by their complex mode amplitude functions $h_j(t)$, which represent the temporal shape of each wave-packet, where j indexes the mode number. A photon wave-packet annihilation operator

A_j can be defined for each mode as the following superposition [14, 110]:

$$A_j = \int h_j(t)\, a_t dt \tag{3.3}$$

where $a_t = (1/\sqrt{2\pi}) \int a_\omega \exp(-i\omega t)\, d\omega$ is the annihilation operator that annihilates a photon at time t. It can be shown that if h_j forms a set of orthonormal functions, satisfying $\int h_i^*(t)\, h_j(t)\, dt = \delta_{ij}$, then the wave-packet annihilation operators obey the bosonic commutation relation $\left[A_i, A_j^\dagger\right] = \delta_{ij}$ just as a_ω or a_t do. This allows us to express the quantum state of the light in its most general form as follows:

$$|\psi\rangle = \bigotimes_{i=1}^{n} |\psi_i\rangle \tag{3.4}$$

where $|\psi_i\rangle = \sum_j (c_{ij}/\sqrt{j!})(A_i^\dagger)^j |0\rangle$ denotes the quantum state of light in the i-th temporal mode, and n represents the number of modes in which all, or, using an approximation, the majority of photons exist. The elements c_{ij} are components of a matrix containing the superposition coefficients. Additionally, using the above representation, the mean number of photons existing in the i-th mode is given by:

$$\bar{n}_i = \langle\psi_i| A_i^\dagger A_i |\psi_i\rangle = \sum_j j|c_{ij}|^2 \tag{3.5}$$

Using equation 3.3, the first-order autocorrelation function $G^{(1)}(t_2, t_1) = \left\langle a_{t_2}^\dagger a_{t_1} \right\rangle$ for a light field in the quantum state $|\psi\rangle$, as given in equation 3.4, can be written as follows:

$$G^{(1)}(t_2, t_1) = \left(\bigotimes_{i=1}^{n} \langle\psi_i|\right) a_{t_2}^\dagger a_{t_1} \left(\bigotimes_{i=1}^{n} |\psi_i\rangle\right) = \sum_{i=1}^{n} \bar{n}_i h_i^*(t_1)\, h_i(t_2) \tag{3.6}$$

The above equation suggests that an effective way to identify an appropriate set of orthonormal modes for a light field is through the eigendecomposition of its first-order autocorrelation matrix [63]. In this process, the resulting eigenvectors form the orthonormal mode function set, and their corresponding eigenvalues indicate the mean number of photons in each mode. The unnormalized first autocorrelation functions for l_{out} and r_{out} modes, by definition, are [78]:

$$\begin{aligned} G_l^{(1)}(t_2, t_1) &= \left\langle l_{out}^\dagger(t_2)\, l_{out}(t_1) \right\rangle \\ G_r^{(1)}(t_2, t_1) &= \left\langle r_{out}^\dagger(t_2)\, r_{out}(t_1) \right\rangle \end{aligned} \tag{3.7}$$

which after substituting equation 3.2, results in:

$$\begin{aligned} G_l^{(1)}(t_2,t_1) &= \gamma_g \langle \sigma_{32}(t_2)\,\sigma_{23}(t_1)\rangle \\ G_r^{(1)}(t_2,t_1) &= \gamma_g \langle \sigma_{31}(t_2)\,\sigma_{13}(t_1)\rangle + \langle {r_{in}}^{\dagger}(t_2)\,r_{in}(t_1)\rangle + \sqrt{\gamma_g}\langle {r_{in}}^{\dagger}(t_2)\,\sigma_{13}(t_1)\rangle \\ &\quad + \sqrt{\gamma_g}\langle \sigma_{31}(t_2)\,r_{in}(t_1)\rangle \end{aligned} \tag{3.8}$$

To find $G_{r,l}^{(1)}$, we use quantum regression theorem (QRT). Based on this theorem, if there exists a complete set of system operators A_μ, $\mu = 1, 2, \ldots$ such that:

$$\frac{d}{dt}\langle A_\mu(t)\rangle = \sum_\lambda M_{\mu\lambda}\langle A_\lambda(t)\rangle \tag{3.9}$$

for a two-point correlation, like the ones appeared in equation 3.8, one can write [17]:

$$\frac{d}{dt_2}\langle A_\mu(t_2)\,O(t_1)\rangle = \sum_\lambda M_{\mu\lambda}\langle A_\lambda(t_2)\,O(t_1)\rangle \tag{3.10}$$

To assess the performance of the single photon subtractor, we examine three distinct input pulses: Fock state pulse, squeezed vacuum pulse, and coherent pulse. Initially, consider an n-photon Fock state pulse with carrier frequency ω_1 and a wavepacket amplitude of $\alpha(t)$ sent to the input mode r_{in}. By sandwitching the optical Bloch equations 3.1 between the input n-photon Fock state $|n\rangle$, the following sets of recurrence differential equations governing the time evolution of the expectation values $\langle\sigma_{ab}\rangle = {}_n\langle\sigma_{ab}\rangle_n = \langle n|\,\sigma_{ab}\,|n\rangle$ are derived:

$$\begin{aligned} \partial_t\langle\sigma_{11}\rangle &= \sqrt{\gamma_g}\left({}_n\langle\sigma_{31}\rangle_{n-1}\,\alpha(t) + \alpha^*(t)\,{}_{n-1}\langle\sigma_{13}\rangle_n\right)\sqrt{n} + \gamma_g\langle\sigma_{33}\rangle \\ \partial_t\langle\sigma_{33}\rangle &= -\sqrt{\gamma_g}\left({}_n\langle\sigma_{31}\rangle_{n-1}\,\alpha(t) + \alpha^*(t)_{n-1}\langle\sigma_{13}\rangle_n\right)\sqrt{n} - 2\gamma_g\langle\sigma_{33}\rangle \\ \partial_t\langle\sigma_{13}\rangle &= \sqrt{\gamma_g}\left({}_n\langle\sigma_{33}\rangle_{n-1} - {}_n\langle\sigma_{11}\rangle_{n-1}\right)\sqrt{n}\alpha(t) - \gamma_g\langle\sigma_{13}\rangle \\ \partial_t\langle\sigma_{31}\rangle &= \sqrt{\gamma_g}\left({}_{n-1}\langle\sigma_{33}\rangle_n - {}_{n-1}\langle\sigma_{11}\rangle_n\right)\sqrt{n}\alpha^*(t) - \gamma_g\langle\sigma_{31}\rangle \\ \partial_t\langle\sigma_{32}\rangle &= -\sqrt{\gamma_g}{}_{n-1}\langle\sigma_{12}\rangle_n\sqrt{n}\alpha^*(t) - \gamma_g\langle\sigma_{32}\rangle \\ \partial_t\langle\sigma_{12}\rangle &= \sqrt{\gamma_g}{}_n\langle\sigma_{32}\rangle_{n-1}\sqrt{n}\alpha(t) \end{aligned} \tag{3.11}$$

In deriving the above equation, we used the relation $r_{in}(t)\,|n\rangle = \sqrt{n}\alpha(t)\,|n-1\rangle$. To calculate the expectation value $\langle\sigma_{ij}\rangle$, one needs to first derive differential equations for all terms of the form ${}_i\langle\sigma_{ab}\rangle_j = \langle i|\,\sigma_{ab}\,|j\rangle$, where both i and j vary between 0 and n. This results in a set of $6(n+1)^2$ coupled equations which can be numerically integrated with the initial condition of ${}_i\langle\sigma_{11}\rangle_i = 1$. Also, according to equations 3.9 and 3.10, similar sets

of equations are derived for the first correlation terms appeared in the right-hand side of equation 3.8 i.e. $\langle\sigma_{32}(t_2)\,\sigma_{23}(t_1)\rangle$ and $\langle\sigma_{31}(t_2)\,\sigma_{13}(t_1)\rangle$:

$$\begin{aligned}
\partial_{t_2}\langle\sigma_{11}(t_2)\,\sigma_{13}(t_1)\rangle &= \sqrt{n\gamma_g}\left({}_n\langle\sigma_{31}(t_2)\,\sigma_{13}(t_1)\rangle_{n-1}\,\alpha(t_2)+\alpha^*(t_2)\,{}_{n-1}\langle\sigma_{13}(t_2)\,\sigma_{13}(t_1)\rangle_n\right)\\
&\quad+\gamma_g\langle\sigma_{33}(t_2)\,\sigma_{13}(t_1)\rangle\\
\partial_{t_2}\langle\sigma_{33}(t_2)\,\sigma_{13}(t_1)\rangle &= -\sqrt{n\gamma_g}\left({}_n\langle\sigma_{31}(t_2)\,\sigma_{13}(t_1)\rangle_{n-1}\,\alpha(t_2)+\alpha^*(t_2)_{n-1}\langle\sigma_{13}(t_2)\,\sigma_{13}(t_1)\rangle_n\right)\\
&\quad-2\gamma_g\langle\sigma_{33}(t_2)\,\sigma_{13}(t_1)\rangle\\
\partial_{t_2}\langle\sigma_{13}(t_2)\,\sigma_{13}(t_1)\rangle &= \sqrt{n\gamma_g}\left({}_n\langle\sigma_{33}(t_2)\,\sigma_{13}(t_1)\rangle_{n-1}\alpha(t_2)-\alpha^*(t_2)\,{}_n\langle\sigma_{11}(t_2)\,\sigma_{13}(t_1)\rangle_{n-1}\right)\\
&\quad-\gamma_g\langle\sigma_{13}(t_2)\,\sigma_{13}(t_1)\rangle\\
\partial_{t_2}\langle\sigma_{31}(t_2)\,\sigma_{13}(t_1)\rangle &= \sqrt{n\gamma_g}\left({}_{n-1}\langle\sigma_{33}(t_2)\,\sigma_{13}(t_1)\rangle_n-{}_{n-1}\langle\sigma_{11}(t_2)\,\sigma_{13}(t_1)\rangle_n\right)\alpha^*(t_2)\\
&\quad-\gamma_g\langle\sigma_{31}(t_2)\,\sigma_{13}(t_1)\rangle\\
\partial_{t_2}\langle\sigma_{32}(t_2)\,\sigma_{23}(t_1)\rangle &= -\sqrt{n\gamma_g}{}_{n-1}\langle\sigma_{12}(t_2)\,\sigma_{23}(t_1)\rangle_n\alpha^*(t_2)-\gamma_g\langle\sigma_{32}(t_2)\,\sigma_{23}(t_1)\rangle\\
\partial_{t_2}\langle\sigma_{12}(t_2)\,\sigma_{23}(t_1)\rangle &= \sqrt{n\gamma_g}{}_n\langle\sigma_{32}(t_2)\,\sigma_{23}(t_1)\rangle_{n-1}\alpha(t_2)
\end{aligned}\tag{3.12}$$

which are derived based on the commutation relation $[\sigma_{ij}(t_1), r_{in}(t_2)]=0$ for $t_2>t_1$, as a result of causality [143]. Equation 3.12 needs to be integrated from $t_2=t_1$ according to the following initial conditions:

$$\begin{aligned}
{}_i\langle\sigma_{32}(t_2)\,\sigma_{23}(t_1)\rangle_j\Big|_{t_2=t_1} &= {}_i\langle\sigma_{31}(t_2)\,\sigma_{13}(t_1)\rangle_j\Big|_{t_2=t_1} = {}_i\langle\sigma_{33}(t_1)\rangle_j\\
{}_i\langle\sigma_{12}(t_2)\,\sigma_{23}(t_1)\rangle_j\Big|_{t_2=t_1} &= {}_i\langle\sigma_{11}(t_2)\,\sigma_{13}(t_1)\rangle_j\Big|_{t_2=t_1} = {}_i\langle\sigma_{13}(t_1)\rangle_j
\end{aligned}\tag{3.13}$$

For the other three correlation terms appeared in equation 3.8, one can write:

$$\begin{aligned}
\left\langle {r_{in}}^\dagger(t_2)\,r_{in}(t_1)\right\rangle &= n\alpha^*(t_2)\,\alpha(t_1)\\
\left\langle {r_{in}}^\dagger(t_2)\,\sigma_{13}(t_1)\right\rangle &= \sqrt{n}\alpha^*(t_2)\,{}_{n-1}\langle\sigma_{13}(t_1)\rangle_n\\
\langle\sigma_{31}(t_2)\,r_{in}(t_1)\rangle &= {}_n\langle\sigma_{31}(t_2)\rangle_{n-1}\sqrt{n}\alpha(t_1)
\end{aligned}\tag{3.14}$$

When the input is a squeezed vacuum or coherent state, a similar analysis can be used to calculate the first autocorrelation matrices, with the detailed steps provided in Appendix B.

In our simulations, we make the assumption that the input pulse has a Gaussian temporal shape. For the case of an input Fock or squeezed state, the temporal profile is modeled by the normalized form of a Gaussian function i.e. $\alpha(t)=\sqrt{2}\Big/\sqrt[4]{\pi\tau^2}\times\exp(-2t^2/\tau^2)$, while for the coherent pulse containing an average number of $\bar{n}$ photons, where $\alpha(t)$ essentially represents the phasor of the light pulse, we multiply it by $\sqrt{\bar{n}}$. By employing the method described above, we first determine the first-order coherence matrices of the light

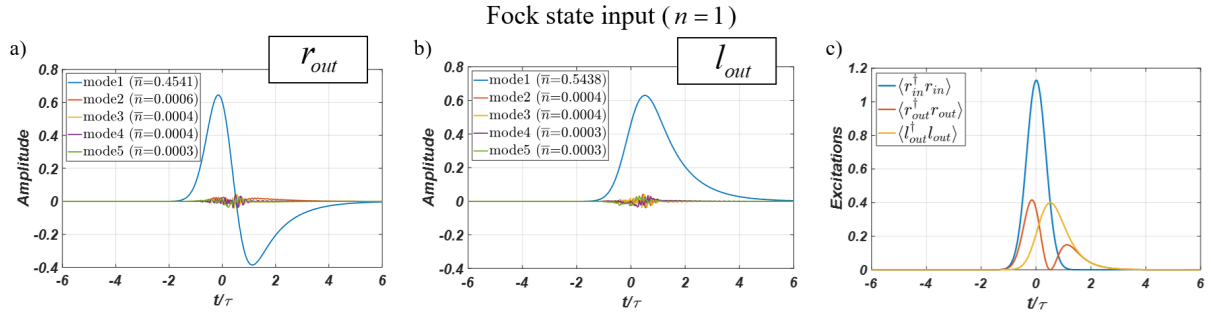


Figure 3.2: System output with a single-photon Fock state as input ($\tau = 1/\gamma_g$), showing (a) modal decomposition of the right (r_{out}) output mode, (b) modal decomposition of the left (l_{out}) output mode, and (c) temporal distribution of photons in input and output pulses.

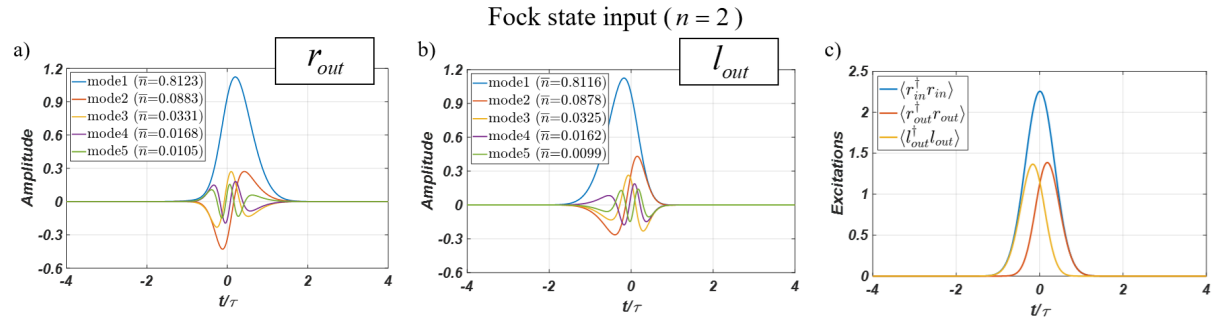


Figure 3.3: System output with a two-photon Fock state as input ($\tau = 100/\gamma_g$), showing (a) modal decomposition of the right (r_{out}) output mode, (b) modal decomposition of the left (l_{out}) output mode, and (c) temporal distribution of photons in input and output pulses.

at outputs r_{out} and l_{out}. Then, through an eigen-decomposition, we identify the mode-shapes contained in each output. Results are illustrated in Figures 3.2 to 3.5 for the three different types of input pulses. The legends of the plots indicate the number of photons in each eigenmode which are their corresponding eigenvalues. For enhanced visual representation of the photon distribution among modes, and to better illustrate the relative contribution of different modes to the final modal structure, the mode shapes are weighted by the square root of the contained photons. It should be noted that, because the input light applied to the system is a single-wavepacket pulse with a real-valued amplitude function, the calculated $G^{(1)}$ will be both real-valued and symmetric, as the autocorrelation matrix is Hermitian. The eigenvalues and eigenvectors of a real symmetric matrix are also real, which explains why the mode amplitude functions shown in Figures 3.2 to 3.5 are

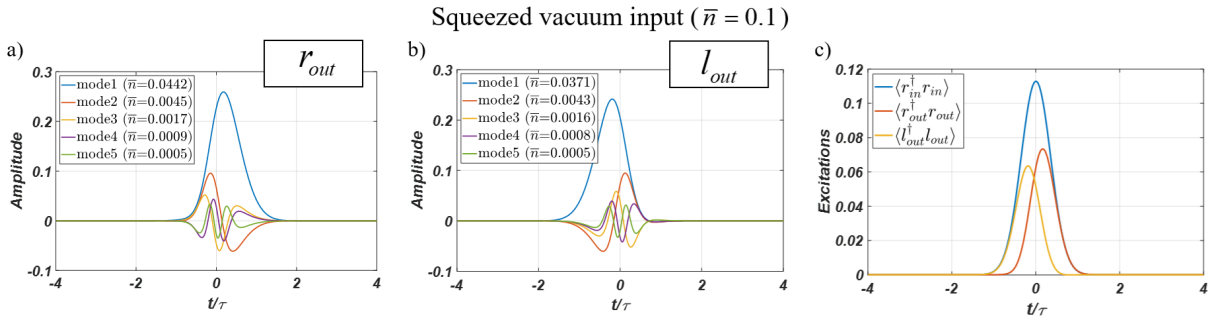


Figure 3.4: System output with a squeezed vacuum state with $\bar{n} = 0.1$ photons as input ($\tau = 100/\gamma_g$), showing (a) modal decomposition of the right (r_{out}) output mode, (b) modal decomposition of the left (l_{out}) output mode, and (c) temporal distribution of photons in input and output pulses.

real-valued.

As can be seen in Figure 3.2, the utilization of a single-photon Fock state as the input reveals a linear system behavior, generating single-mode outputs for both r_{out} and l_{out} outputs. Any small-amplitude higher-order modes observed in this case can be attributed to minor numerical errors. In contrast, in all other cases where the input comprises multi-photon states, the system exhibits nonlinear behavior, leading to multi-mode outputs. This nonlinearity stems from the saturation of the emitter when exposed to light pulses containing more than one photon.

Due to the deterministic nature of the photon subtractor, if the duration of the input pulse is long enough based on the coupling strength of the emitter to the guided modes, a single photon is subtracted from all non-vacuum states at the input. Because of this, in Figure 3.2, we assume a short pulse with $\tau = 1/\gamma_g$ so that there is still approximately half a photon at the right output, enabling us to explore the modal composition at this output as well. Otherwise, the single photon would be completely reflected, and there would be no photon in the right output mode. However, in all other figures throughout this chapter, the pulse duration is assumed to be much longer than the radiation time of the atom to the waveguide, i.e., $\tau = 100/\gamma_g$. In Figures 3.2 to 3.5, part (c) illustrates the temporal intensity of the input and output pulses, representing their mean photon number distribution. In Figure 3.2.(c), due to the fast input pulse, it takes some time for the emitter to initiate interaction with the light. Consequently, the r_{out} pulse leads compared to the l_{out} pulse. However, after the emitter becomes excited, it starts reflecting photons to the l_{out} mode, leading to a decrease in the intensity of the transmitted pulse. Additionally, both output

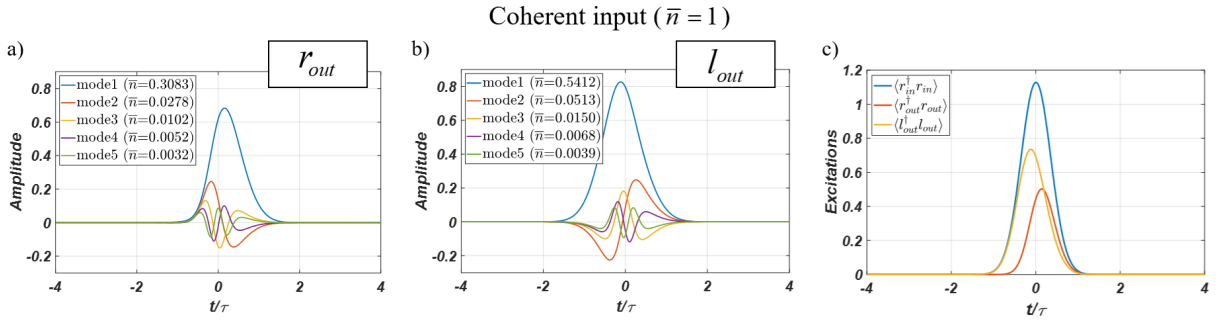


Figure 3.5: System output with a coherent state with $\bar{n} = 1$ photon as input ($\tau = 100/\gamma_g$), showing (a) modal decomposition of the right (r_{out}) output mode, (b) modal decomposition of the left (l_{out}) output mode, and (c) temporal distribution of photons in input and output pulses.

pulses persist even after the input pulse vanishes, which is attributed to the time needed for the excited emitter to radiate photons to the guided modes. Conversely, as observed in the temporal intensity plots (part (c)) of the other three figures, the l_{out} pulse leads the r_{out} pulse. This implies that when the input pulse duration is sufficiently long, the subtractor subtracts the first arriving photon and subsequently allows other photons to transmit.

3.3 Calculation of the Output Quantum State

After determining the modes included in the output light through eigen decomposition of the first-order coherence matrices, we follow the method proposed in Ref. [63] and described in section 1.2.2 to calculate the quantum state of the light in each mode. The method enables the modeling of each propagating wavepacket in the waveguide through a single virtual one-sided cavity with a time-dependent decay rate, coupled with the three-level emitter in a cascaded manner. The input cavity (with annihilation operator a_α) initially contains the quantum state of the input pulse sent to the photon subtractor, while the output cavities (with annihilation operators a_u^i and a_w^i) capture the quantum state contained at each output mode as the interaction occurs. Figure 3.6 shows a schematic view of the obtained quantum network, where only one cavity is depicted at each output port for simplicity. This network can be evolved over time by solving its governing master equation:

$$\frac{d\rho}{dt} = -i\,[H, \rho] + \sum_{i=0} \left(L_i \rho L_i^{\dagger} - \frac{1}{2} \left\{ L_i^{\dagger} L_i, \rho \right\} \right) \tag{3.15}$$

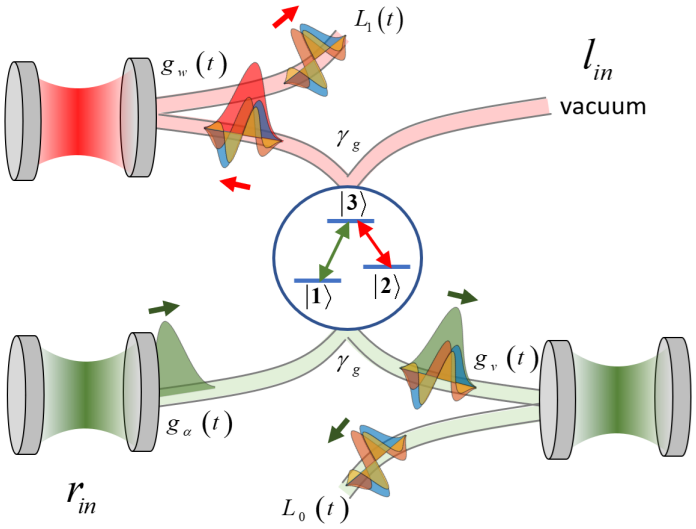


Figure 3.6: Quantum network comprising one input and two output cavities interacting with the emitter in a cascade manner. The couplings of the output cavities are adjusted so that they absorb the main wavepacket at each output pulse.

with the following Hamiltonian and Lindblad operators in the rotating frame:

$$\begin{aligned} H(t) &= \tfrac{i}{2}\left[\sqrt{\gamma_g} g_\alpha(t)\, a_\alpha^\dagger \sigma_{13} + \sqrt{\gamma_g} g_v^*(t)\, \sigma_{31} a_v + g_\alpha(t)\, g_v^*(t)\, a_\alpha^\dagger a_v + \sqrt{\gamma_g} g_w^*(t)\, \sigma_{32} a_w - \text{H.c.}\right] \\ L_0(t) &= \sqrt{\gamma_g}\sigma_{13} + g_\alpha^*(t)\, a_\alpha + g_v^*(t)\, a_v \qquad\qquad L_1(t) = \sqrt{\gamma_g}\sigma_{23} + g_w^*(t)\, a_w \end{aligned} \tag{3.16}$$

L_0 and L_1 in the above equation are responsible for collapses when a photon, not in the main mode, is detected at the right and left propagating outputs, respectively. The time-dependent coupling of the cavities to their input continuum field is related to their corresponding wavepacket function according to the below relations:

$$g_\alpha(t) = \frac{\alpha^*(t)}{\sqrt{1 - \int_0^t dt' |\alpha(t')|^2}} \qquad g_x(t) = -\frac{x^*(t)}{\sqrt{\int_0^t dt' |x(t')|^2}} \qquad x = v, w \tag{3.17}$$

Here, $\alpha(t)$, as before, represents the wavepacket amplitude of the input pulse, while $v(t)$ and $w(t)$ denote the first mode shapes of the pulses leaving the system at the right and left propagating outputs, respectively. The above model can be extended for a higher number of cavities to capture additional modes at the outputs (see Figure 1.4.(b)), following a similar framework based on the SLH method [24].

3.4 Generating Single-Mode Non-Gaussian States

Since our primary objective is to investigate the photon subtractor's potential for generating non-Gaussian states, we specifically concentrate on cases where the input to the system is of Gaussian type, namely the squeezed vacuum and coherent state inputs. While the presented photon subtractor operates deterministically, it can only subtract a photon if there is one present in the input, meaning that the input is not in the vacuum state. Therefore, for lightly squeezed vacuum states—such as those reported in Ref. [134] —as well as weak coherent pulses, containing a low mean photon number, there is still a high probability that no photon is subtracted. As a result, the process still needs to be heralded, where the detection of a photon at the l_{out} mode signals the successful subtraction of a photon and the potential generation of a non-Gaussian state.

Given that numerous applications in CV quantum optics rely on the utilization of single-mode non-Gaussian quantum states, we initially explore a configuration featuring a demultiplexing device at the r_{out} output. This device is a demultiplexer designed to effectively isolate the principal temporal mode from others, as depicted in Figure 3.7.(a). One experimental implementation for achieving this separation involves the utilization of quantum pulse gates (QPGs) [110]. A QPG operates through quantum frequency conversion in a nonlinear optical medium, where the input light interacts with a group-velocity-matched, shaped strong laser pulse. Depending on the medium's nonlinearity, this process can occur via either three-wave or four-wave mixing, translating the desired mode in the frequency domain to allow easy separation from the remaining light [2]. Initial experimental results for single-stage QPGs have demonstrated mode selectivity around 80% [13]. However, both theoretical and experimental studies have shown that cascading QPGs in a two-stage interferometric scheme can achieve near-unity conversion efficiency and selectivity [111,112].

In the presented configuration, two detectors are utilized: detector D2 registers a click when a photon is successfully subtracted and directed to the l_{out} output, while detector D1 identifies the presence of photons in modes other than the principal mode of the r_{out} output. Now consider that a squeezed vacuum Gaussian pulse $|\zeta\rangle = \hat{S}(\zeta)|0\rangle$ is sent to r_{in} input and we want to study the generated quantum state in the principal mode of the r_{out} output. To model this problem, we need to consider a quantum network similar to the one shown in Figure 3.6 with one virtual cavity at the input, one at the r_{out} output, and no cavity at the l_{out} output. The Hamiltonian of the system and Lindblad collapse operators corresponding to photon detection at detectors D1 and D2 will be as follows:

$$\begin{aligned} H(t) &= \tfrac{i}{2}\left[\sqrt{\gamma_g} g_\alpha(t)\, a_\alpha^\dagger \sigma_{13} + \sqrt{\gamma_g} g_v^*(t)\, \sigma_{31} a_v + g_\alpha(t)\, g_v^*(t)\, a_\alpha^\dagger a_v - \text{H.c.}\right] \\ L_0(t) &= \sqrt{\gamma_g}\sigma_{13} + g_\alpha^*(t)\, a_\alpha + g_v^*(t)\, a_v \qquad L_1(t) = \sqrt{\gamma_g}\sigma_{23} \end{aligned} \tag{3.18}$$

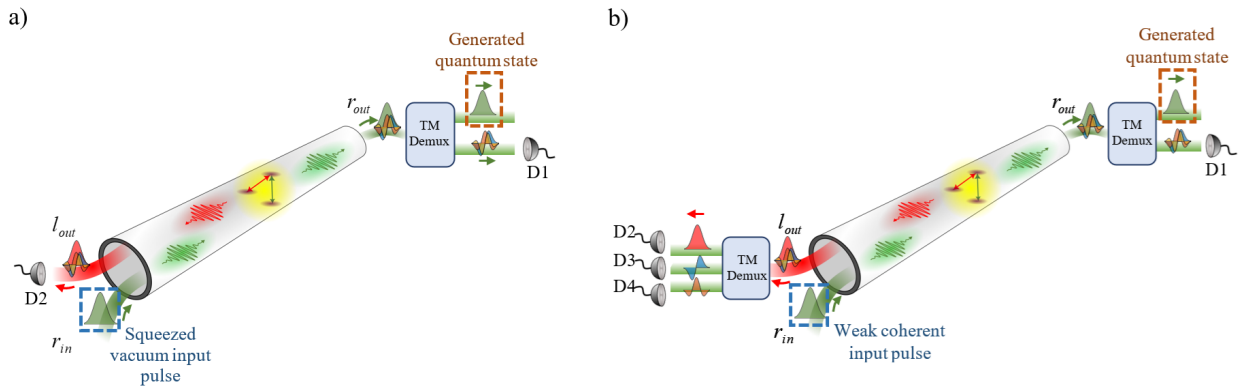


Figure 3.7: Proposed configurations for generation of single-mode non-Gaussian states from pulsed Gaussian input light: (a) configuration with one demultiplexer and two detectors used for squeezed vacuum input pulses, and (b) configuration with two demultiplexers and four detectors used for coherent input pulses.

We employ the Monte Carlo wave-function (MCWF) method implemented in the QuTiP package in Python to simulate the described experimental scenario. Our focus is on the heralded (i.e. conditional on a detection event) generation of the output quantum state in two specific cases. First, we explore the scenario where no measurement is performed using detector D1, while D2 heralds the successful subtraction of a photon. In the second case, we investigate the generated state signaled by a click on D2, with no concurrent click recorded by D1. The results are presented in Figures 3.8 and 3.9 for two different input states with different squeezing levels containing mean number of photons $\bar{n} = 0.1$ and 0.2 (corresponding to $|\zeta| = 0.31$ and$|\zeta| = 0.43$), respectively. As seen in these figures, both measurement scenarios have resulted in the generation of non-Gaussian Wigner functions, reaching negative values and closely resembling the Wigner function of an odd Schrödinger's kitten state. The concept of generating Schrödinger's cat states by subtracting or adding single photons through traditional non-deterministic methods, equivalent to the implementation of photon annihilation and creation operators, has been explored for a long time [83]. For the sake of comparison, part (a) of the figures depicts the Wigner function of the state generated by applying the annihilation operator. Additionally, part (b) shows the result of applying ideal deterministic single-photon subtraction operator $\hat{s}$ introduced in section 1.1.2 to the input state.

In Figure 3.10, the fidelity of these generated states with the odd Schrödinger cat state $|\text{cat}_o\rangle = |\alpha\rangle - |-\alpha\rangle$ is plotted as a function of the amplitude α. As shown in this figure, while the first scenario, where no measurement is performed by detector D1, cannot

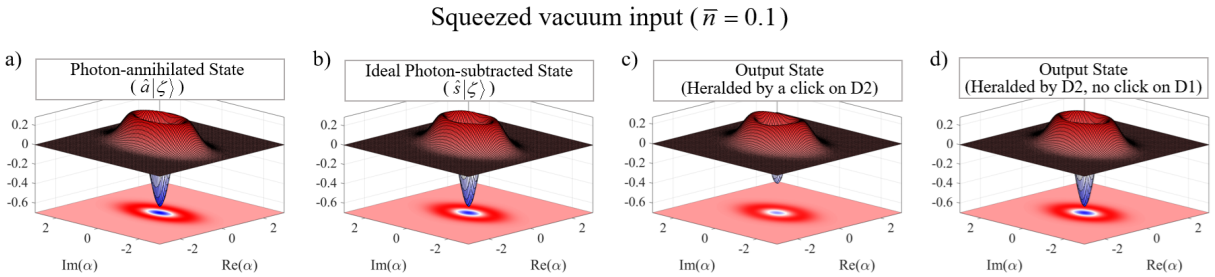


Figure 3.8: Photon subtraction results for a squeezed vacuum input $|\zeta\rangle$ with a mean photon number of $\bar{n} = 0.1$. The plots show the Wigner functions for (a) $\hat{a}\,|\zeta\rangle$, (b) $\hat{s}\,|\zeta\rangle$, (c) generated state by the proposed subtractor with no measurement performed by D1, and (d) generated state by the proposed subtractor where both D1 and D2 are used for measurements according to the described scenario.

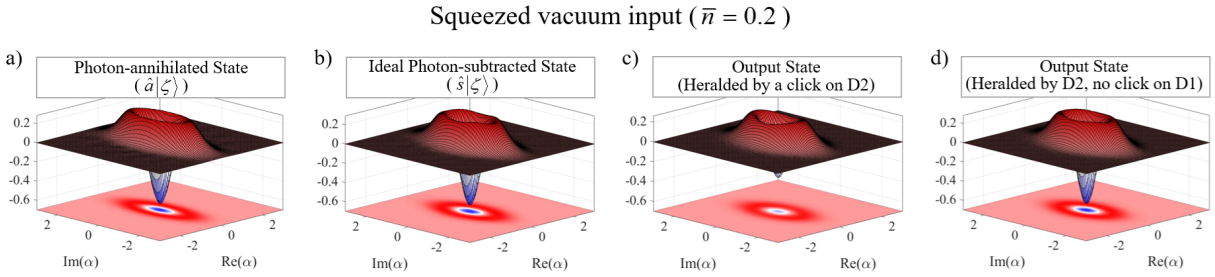


Figure 3.9: Photon subtraction results for a squeezed vacuum input $|\zeta\rangle$ with a mean photon number of $\bar{n} = 0.2$. The plots show the Wigner functions for (a) $\hat{a}\,|\zeta\rangle$, (b) $\hat{s}\,|\zeta\rangle$, (c) generated state by the proposed subtractor with no measurement performed by D1, and (d) generated state by the proposed subtractor where both D1 and D2 are used for measurements according to the described scenario.

surpass a fidelity of 90%, the second scenario generates cat states with an amplitude close to unity (given the level of squeezing) and achieves a fidelity approaching unity. While the non-deterministic method of photon subtraction can also theoretically generate cat states with fidelity approaching unity, it is important to note that this approach suffers from a significantly low success probability. This limitation arises from the use of beam splitters with very low reflectivity to suppress the subtraction of more than one photon. In contrast, the deterministic photon subtractor presented here can generate these states with much higher probabilities. Moreover, success probability increases as the level of squeezing in the input state rises. For the two scenarios discussed earlier, when $|\zeta| = 0.31$ the success

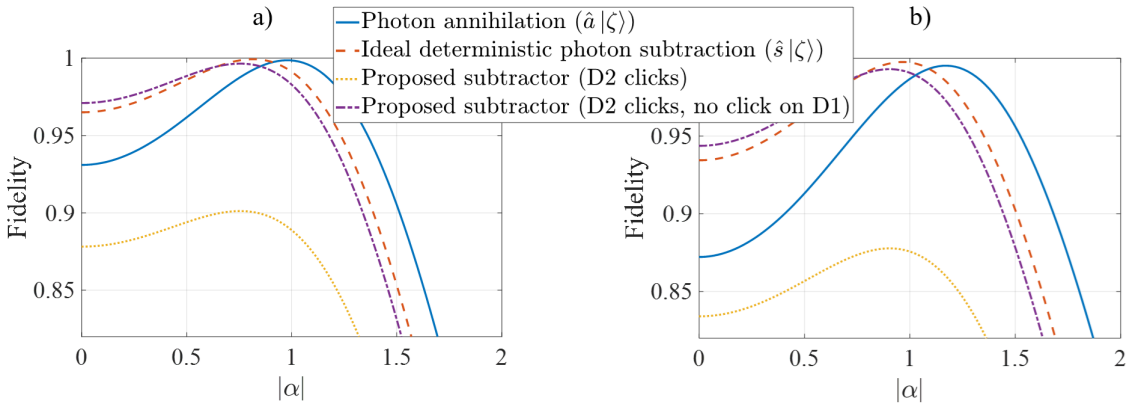


Figure 3.10: Fidelity between the generated states (obtained by applying different photon subtraction methods, as indicated in the plot legend) and odd Schrödinger's cat states of amplitude α. The input $|\zeta\rangle$ is a squeezed vacuum state with mean photon numbers: (a) $\bar{n} = 0.1$, and (b) $\bar{n} = 0.2$.

probabilities are 4.3% and 3.5%, respectively. Increasing the squeezing to $|\zeta| = 0.43$ raises the success probabilities to 8.63% and 6.67%.

While squeezed states are indeed Gaussian states with positive Wigner functions throughout their phase space and exhibit classical-like properties such as well-defined phase and amplitude, they are not readily available experimentally. Their generation typically necessitates nonlinear interactions such as parametric down-conversion [1]. Conversely, the generation of few-photon coherent pulses is relatively straightforward, achieved through the appropriate attenuation of modulated laser beams. This highlights the significance of developing systems capable of directly generating exotic non-Gaussian states from coherent light. The coherent state is an eigenstate of the annihilation operator, implying that traditional beamsplitter-based photon subtraction does not alter the coherent input. Furthermore, an ideal deterministic photon subtractor (represented by the operator $\hat{s}$ defined in section 1.1.2) when applied to a coherent state, while altering its photon number distribution, is still incapable of generating non-classical effects such as negative Wigner functions.

We thus aim to leverage the nonlinear multi-temporal mode nature of the SPRINT mechanism to explore the possibility of heralded generation of non-Gaussian states from a coherent input pulse. To achieve this, we consider the schematic setup configuration depicted in Figure 3.7.(b). In this setup, there are two demultiplexers at the two outputs of the photon subtractor, which separate the generated temporal modes. The first

demultiplexer at the r_{out} output, similar to Figure 3.7.(a), only separates the principal mode, which contains the major part of the photons, from the other modes. The second demultiplexer at the l_{out} output independently extracts the first three modes of the pulse. Three detectors (D2 to D4) are utilized at different outputs of this demultiplexer which allow us to determine the mode at which the subtracted photon exists. It's important to note that since the l_{out} output pulse cannot contain more than one photon in the deterministic photon subtraction, only one of the detectors can register a click. In our scenario, we explore the conditional generation of quantum states at the principal mode of the r_{out} output based on three different conditions. First, D1 registers no click, and D2 registers one. Second, D1 registers no click, and D3 registers one. Third, D1 registers no click, and D4 registers one.

To simulate the system, one can consider a quantum network again similar to the one shown in Figure 3.6 but with three cascaded virtual cavities at the l_{out} output. Since here we are specifically interested in conditions where all the output photons go to the arranged cavities, and thus, no collapse occurs, it is possible to directly solve Schrödinger's equation $i\hbar\partial_t |\psi\rangle = H_{eff} |\psi\rangle$ using a time-dependent non-Hermitian effective Hamiltonian. The form of this Hamiltonian is given by $H_{eff} = H - i\hbar/2 \left(L_0^\dagger L_0 + L_1^\dagger L_1\right)$, where the network Hamiltonian H and Lindblad operators L_0 and L_1 are derived in a manner similar to the explanation provided above equation 3.15 (see supplementary material of Ref. [63]). After determining the final density matrix $\rho = |\psi\rangle \langle\psi|$ of the entire system, the quantum state stored in the r_{out} output cavity can be extracted by defining a suitable projection operator projecting the density matrix on a subspace based on the specified condition, which identifies the l_{out} cavity containing the subtracted photon. The density matrix of the resulting quantum state is obtained by projecting the overall density matrix using this operator, followed by a partial trace over the atomic state and the states of all cavities other than the one at r_{out} output. The outcomes of this simulation are depicted in parts (a) to (c) of Figures 3.11 and 3.12 for coherent inputs with $\bar{n} = 1$ and 3 photons, respectively.

As depicted in these figures, when the subtracted photon is detected in the first mode of the l_{out} output, the resulting state closely resembles a coherent state. On the other hand, if the subtracted photon is found in the second mode, the output state resembles a displaced single-photon Fock state. However, when the photon is detected in the third mode, indicated by a click from detector D4, the generated state exhibits a Wigner function similar to that of a displaced cat state, represented by the form $\hat{D}(\gamma)\left[|\alpha\rangle + e^{i\beta} |-\alpha\rangle\right]$, where $\hat{D}$ is the displacement operator. Through optimization of the parameters α, β, and γ, we have identified the cat state that exhibits the highest fidelity with the state shown in part (c) of the figures. These optimized cat states are presented in part (d) of the

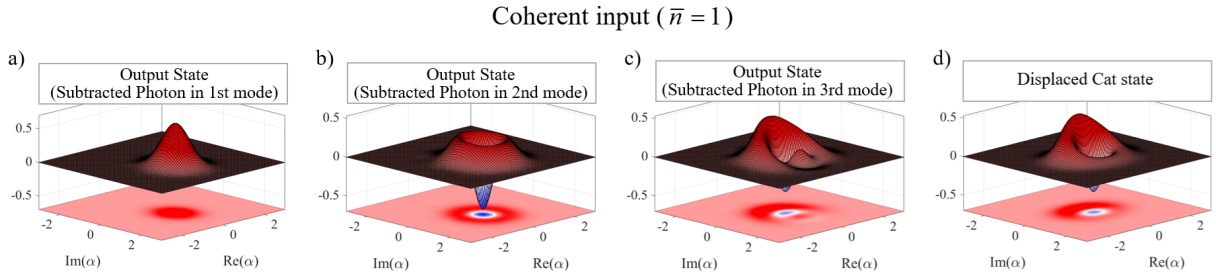


Figure 3.11: Photon subtraction results for a coherent input with a mean photon number of $\bar{n} = 1$. The plots show the Wigner functions for (a) generated output state when the subtracted photon in detected in 1st mode, (b) generated output state when the subtracted photon in detected in 2nd mode, (c) generated output state when the subtracted photon in detected in 3rd mode, and (d) a displaced cat state with parameters $\alpha = 0.60$, $\beta = 3.90$, and $\gamma = 0.07$.

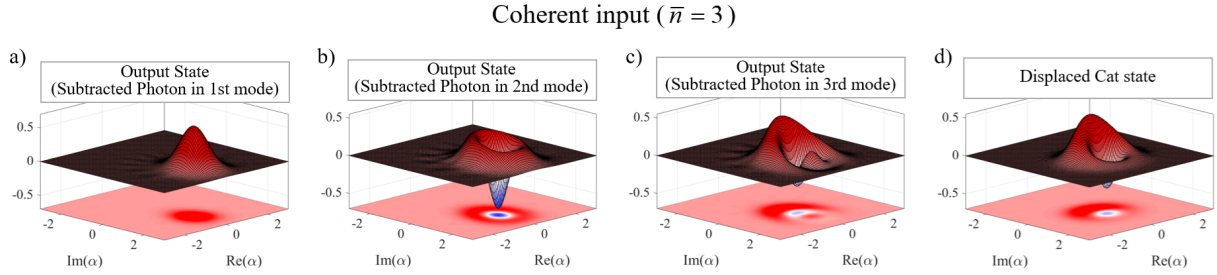


Figure 3.12: Photon subtraction results for a coherent input with a mean photon number of $\bar{n} = 3$. The plots show the Wigner functions for (a) generated output state when the subtracted photon in detected in 1st mode, (b) generated output state when the subtracted photon in detected in 2nd mode, (c) generated output state when the subtracted photon in detected in 3rd mode, and (d) a displaced cat state with parameters $\alpha = 0.47$, $\beta = 3.83$, and $\gamma = 0.56$.

figures, with their corresponding parameters detailed in the figure captions. Notably, the maximum fidelity achieved is 99.3% and 99.1% for the input coherent states with $\bar{n} = 1$ and 3 photons, respectively. A further displacement of this generated states produces the Schrodinger's cat state which is a pivotal quantum source with numerous applications in quantum technology.

3.5 Current State of Chiral Waveguide–Emitter Coupling

Successful interfacing of quantum emitters with chiral nanophotonic structures has been experimentally demonstrated across various platforms [3,54,74,85,102,113,132]. Achieving this requires high confinement levels to activate optical spin-orbit interactions, coupling light's polarization with its propagation direction [77]. Selective interaction of atomic transitions with photons of specific polarizations thereby creates a chiral light-matter system. The performance of these systems is commonly evaluated based on two factors. The first is the total coupling efficiency of each atomic transition to the waveguide, given by $\beta = \gamma/(\gamma + \Gamma)$, where γ is the total emission rate into both counterpropagating waveguide modes, and Γ accounts for all dissipative radiative and non-radiative channels. The second factor is the directionality of the coupling, defined as $F_{dir} = \gamma_{dir}/\gamma$, where γ_{dir} represents the emission rate into the desired propagation direction. Cold atoms coupled to the evanescent field of nanofibers have demonstrated directional emission into the guided modes [102]. In these systems, coupling efficiency can be enhanced by positioning the atoms closer to the fiber surface [19]. Higher coupling efficiencies can also be achieved by replacing the nanofiber with photonic crystal waveguides with reduced group velocity, which occurs when the guided mode frequency approaches the bandgap edge of the photonic structure [54]. Coupling efficiencies as high as $\beta = 0.98$ have been reported when using quantum dots embedded within the waveguide and directly coupled to the waveguide field [3,113]. Charged quantum dots possess a Λ-type energy level structure, making them promising candidates for single-photon Raman interactions. Their potential for deterministic single-photon subtraction has been previously studied [31]. Near-unity directionality has been achieved in both nanofiber and photonic crystal waveguide setups. Cesium cold atoms evanescently trapped on the surface of a nanofiber have demonstrated directional photon emission into the waveguide mode, with a directionality factor of $F_{dir} = 0.92$ [85]. Additionally, for quantum dots coupled to photonic crystal waveguides, directionality values as high as 0.98 have been reported [132]. According to these results, the high coupling and directionality reported specifically for solid-state systems make them potential candidates for implementing the photon subtraction scheme discussed in this chapter.

Chapter 4

One-Way Multi-Emitter Cascade for Photon-Number-Resolving Detection

Robust detection of multi-photon states open experimental access to study the rich space of non-classical states of light by granting new ways for exploring fundamental aspects of quantum optics. PNR detection is required to characterize and diagnose many-photon states of light by measuring their photon-number distributions. Furthermore, generalized detection schemes composed of such detectors can lend access to novel forms of quantum tomography. In particular, characterizing complex, correlated many-photon states [30, 57, 87, 95, 107] can help to reveal dynamics of many-body quantum systems.

In this chapter, we investigate the capability of a cascade of SPRINT-based photon subtractors for PNR detection of multi-photon pulses. To this end, we develop a theoretical formalism to model multi-photon transport through a cascade of waveguide-coupled Λ-type quantum emitters. Multiple-photon propagation in waveguides through quantum emitters have been experimentally [30, 36, 76, 84, 107] and theoretically [58, 59, 81, 104, 140] studied in a variety of settings. Already, the relatively simple case of two photons propagating through a single two-level emitter provides novel output light with features of squeezing, entanglement, and tuneable bunching [51, 70, 76, 84, 106]. More generally, many-photon transport through many two-level and multi-level quantum emitters in a waveguide has shown to output highly non-classical, strongly correlated states and can showcase novel many-body phases of light [7, 30, 57, 72, 124]. A suite of theoretical techniques has been developed to study quantum dynamics of multi-photon quantum light transport through quantum emitters. These include Master equation-based input-output theory [148], scattering matrix formalisms [56, 104, 123], Green's function [7] and matrix product state-based approaches [7, 140], among others [72, 124].

Our analysis in this chapter focuses on the single- and multi-photon scattering characteristics of individual emitter-based subtractors in the time domain and combining them into emitter cascades to evaluate the precision of the proposed detectors. We examine photon propagation in two regimes: linear and nonlinear. In the linear regime, multi-photon propagation can be treated as a series of independent single-photon events, allowing single-photon transport knowledge to infer multi-photon behavior. In the nonlinear regime, photons can arrive within the emitter's lifetime, leading to correlations between input photons due to emitter-mediated photon-photon interactions. The results are analyzed and compared in both regimes and are verified through numerical simulations using the SLH framework of input-output theory combined with the quantum trajectory method.

4.1 Modeling and Formulation

4.1.1 Cascaded photon subtraction scheme

Figure 4.1.(a) shows the schematic of the waveguide-QED system used as deterministic single-photon subtractor. The setup includes a single three-level Λ-type quantum emitter (atom) coupled to two waveguides. The waveguides are chiral [77], allowing light to propagate in one direction only, as indicated by the arrows. Waveguide 1, depicted in red, is coupled to the $|1\rangle - |3\rangle$ transition, while waveguide 2, shown in blue, is coupled to the $|2\rangle - |3\rangle$ transition. These waveguides can be either physically separate or distinct modes of a single waveguide such as counter propagating modes of a bidirectional chiral waveguide, similar to the scheme shown in Figure 3.1 [132]. We use $a_{i,\omega}$ to denote the annihilation operator for an excitation of guided mode i at frequency ω. Additionally, γ_g as before characterizes the coupling strength and defines the rate at which the emitter emits and absorbs photons to and from the guided modes. In the configuration shown, the atom is initially in state $|1\rangle$, and the input pulse is introduced into the input mode of waveguide 1. Consequently, the subtracted photon exits the subtractor through the output mode of waveguide 2, while the remaining photons exit via the output of waveguide 1. If the input photons are separated by a duration longer than the atom's absorption/emission time, only a single photon will interact with the atom at any given time, resulting in no atom-mediated photon-photon interaction. In this case, the probability of each photon being subtracted can be calculated independently based on its frequency content and the system's single-photon transfer function [98]. After one photon is subtracted, the atom in state $|2\rangle$ and no longer interacts with photons in waveguide 1, so any subsequent photons are directly transferred to the output mode of waveguide 1. When two photons arrive at

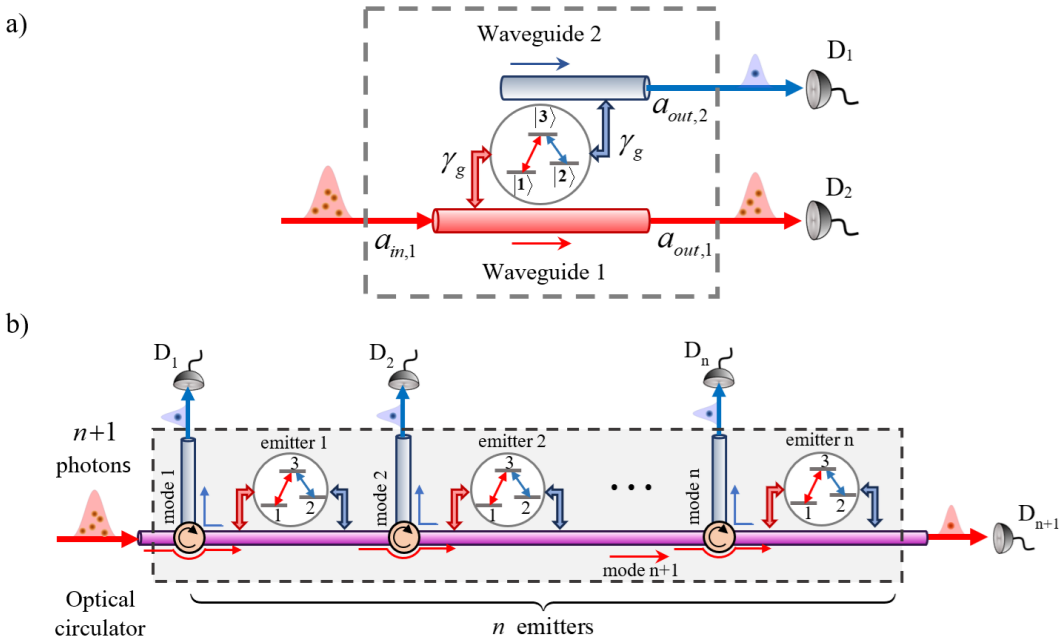


Figure 4.1: (a) Schematic of the photon subtractor as a three-port quantum optics device consisting of a Λ-type emitter coupled to two chiral (one-way) waveguide modes, and (b) A cascade of n photon subtractors forming a PNR detector capable of resolving up to $n+1$ photons.

the atom within a time interval shorter than the atomic response time, they can activate the system's nonlinearity by saturating the atom.

If two single-photon detectors are placed at the outputs of the waveguide modes, as shown in the figure, the single-photon subtractor can function as a PNR detector, capable of counting photons in pulses with up to two photons. In this configuration, the number of detectors registering a click corresponds to the number of photons contained in the input pulse. Following this idea further, PNR detectors capable of resolving higher photon counts can be constructed by cascading single photon subtractors over a shared waveguide, as illustrated in Figure 4.1.(b). In this setup, the atoms each coherently absorb one photon from the right-propagating red mode and divert those photons to the left-propagating blue mode. Optical circulators [60] placed between the emitters extract the single photons subtracted by each emitter and send them to separate detectors via the vertical blue waveguides. In this way, a cascade of n emitters can resolve light pulses containing up to $n+1$ photons. Since there is no external photon input to the waveguide modes 1

to n, they can only be in either a vacuum state or contain a single photon routed by their corresponding circulator from the left propagating field of the chiral waveguide. In contrast, the chiral waveguide mode can contain any number of photons, depending on the photon count in the input pulse. Therefore, the waveguides Hilbert spaces will be $\mathcal{H}_{\text{wg}}^{i=1,\dots,n} = \text{span}\left\{|\text{vac}\rangle, |t\rangle_i\right\}$ and $\mathcal{H}_{\text{wg}}^{i=n+1} = \text{span}\left\{|\text{vac}\rangle, |t_1, t_2, \cdots, t_m\rangle_i\right\}$, where:

$$\begin{aligned} |t_1, t_2, \cdots, t_m\rangle_i &= \prod_{n=1}^{m} a_{i,t_n}^\dagger |\text{vac}\rangle \quad \forall m \in \mathbb{N} \\ |t\rangle_i &= a_{i,t}^\dagger |\text{vac}\rangle \end{aligned} \tag{4.1}$$

In the above expression, $a_{i,t}^\dagger = \int a_{i,\omega}^\dagger \exp(i\omega t)\, d\omega/\sqrt{2\pi}$ is the temporal creation operator creating a photon in the waveguide mode i at time t and in the atom's position. These photons propagate freely in the respective waveguides before and after interacting with the atom. The total Hilbert space of the composite system can be written as the tensor product of these Hilbert spaces with the atomic Hilbert spaces $\mathcal{H}_{\text{atom}}^{i=1,\dots,n} = \text{span}\left\{|1\rangle_i, |2\rangle_i, |3\rangle_i\right\}$. Therefore, a basis for the Hilbert space of the entire system can be represented as:

$$\left[\bigotimes_{i=1}^{n} |\sigma\rangle_i\right] \otimes \left[\bigotimes_{i=1}^{n} |t\rangle_i\right] \otimes |t_1, t_2, \cdots, t_m\rangle_{n+1} \tag{4.2}$$

with $\sigma = 1, 2, 3$ denoting the corresponding atomic level of the emitters. If either of the waveguide modes is in the vacuum state, the corresponding element is replaced by "vac".

4.1.2 Scattering matrix calculation

In quantum field theory, the effect of a local quantum system on propagating quantum fields coupled to it can be studied using the scattering matrix $\mathbf{\Sigma}$. It is essentially the interaction picture propagation operator of the system between two specific time points: long before the interaction starts ($t = \tau^- \to -\infty$) and long after it ends ($t = \tau^+ \to +\infty$). According to this definition, the scattering matrix is given by $\mathbf{\Sigma} = \mathcal{T} \exp\left(-iH_I\left(\tau^+ - \tau^-\right)\right)$, where H_I is the interaction picture Hamiltonian, and $\mathcal{T}$ represents the time-ordering operator. Different elements of the scattering matrix represent the transition amplitude from various input states of the system onto its distinct output states. For instance, consider a PNR detector consisting of n emitters. It can successfully count the number of photons in an $n+1$-photon pulse if one photon is detected at each output port and all emitters end up in state $|2\rangle$. This outcome corresponds to the following element of the scattering matrix:

$$\left[\bigotimes_{i=1}^{n} \langle 2|_i\right] \otimes \left[\bigotimes_{i=1}^{n+1} \langle t'_i|_i\right] \mathbf{\Sigma} \left[\bigotimes_{i=1}^{n} |\text{vac}\rangle_i\right] \otimes |t_1, t_2, \cdots, t_{n+1}\rangle_{n+1} \otimes \left[\bigotimes_{i=1}^{n} |1\rangle_i\right] \tag{4.3}$$

In the above notation, t_1 to t_{n+1} are the time points at which the input photons are introduced to the detector's input port, while t'_1 to t'_{n+1} represent the times at which the output photons are detected at their respective output ports. This means that n photons have interacted with the emitters and been diverted to a different waveguide mode, while one photon has either not interacted with any of the emitters or has been absorbed and then re-emitted into the same waveguide mode.

In a cascaded quantum system, the scattering matrix for the entire system can be expressed as a product of the scattering matrices of each individual cascaded element, integrated over all possible intermediate states. Furthermore, when all cascaded elements are of the same type, the scattering behavior of a single element can provide insight into how optical properties are altered as they propagate through the cascade. Therefore, we begin our analysis by focusing on the scattering behavior of a single photon subtractor, as illustrated in Figure 4.1.(a). When N photons are introduced to the single photon subtractor, two distinct outcomes are possible: either one photon (e.g., j-th photon) is subtracted and diverted to the second waveguide mode, or no photon is subtracted. In the former case, the atom's state changes to $|2\rangle$, while in the latter case, the atom's state remains unchanged. These different outcomes correspond to distinct elements of the N-photon scattering matrix, denoted by Σ_j^N and Σ_0^N, respectively:

$$\begin{aligned}\Sigma_j^N &= \langle 2| \otimes \langle t'_{j'}| \otimes \langle t'_1, \ldots, t'_{j'-1}, t'_{j'+1}, \ldots, t'_N| \, \mathbf{\Sigma} \, |t_1, \ldots, t_N\rangle \otimes |\text{vac}\rangle \otimes |1\rangle \\ \Sigma_0^N &= \langle 1| \otimes \langle \text{vac}| \otimes \langle t'_1, \ldots, t'_N| \, \mathbf{\Sigma} \, |t_1, \ldots, t_N\rangle \otimes |\text{vac}\rangle \otimes |1\rangle \end{aligned} \tag{4.4}$$

We assume that photon arrival times at both the input and output are ordered such that $t_1 \leq t_2 \leq \ldots \leq t_N$ and $t'_1 \leq t'_2 \leq \ldots \leq t'_N$. Since the atom can absorb no more than one photon at a time, it is impossible to detect two consecutive photons at the outputs without sending any photons to the input, meaning that $t_1 \leq t'_1 \leq t_2 \leq t'_2 \leq \ldots \leq t_N \leq t'_N$. Additionally, since after the first photon is subtracted the atom no longer interacts with photons in the red waveguide, we have $t'_i = t_i$ for all photons sent and received after the photon subtraction occurs.

To calculate the matrix elements given in equation 4.4, we follow the approach proposed by Xu and Fan in Ref. [148]. That work investigated multi-photon transport through a waveguide-coupled low-dimensional quantum system, establishing a connection between the general N-photon transport scattering matrix and the Green's functions of the local quantum system. The key significance of this work was that the Green's function could, in turn, be computed using an effective Hamiltonian that depends solely on the internal degrees of freedom of the local system. Later, Xu and Fan's method was extended to time-dependent quantum systems coupled to multiple waveguides in Ref. [140]. There, Trivedi

et al. express the system's propagator elements as functions of the Green's function $\mathcal{G}^{\sigma',\sigma}_{\tau^+,\tau^-}$, which correlates the times of absorption and re-emission of photons to the external optical modes. In this notation, σ and σ' are states of the local quantum system before and after the interaction, respectively. For the case of k photons interacting with the emitter, we have the following Green's functions:

$$\begin{aligned}
\mathcal{G}^{2,1}_{\tau^+,\tau^-}\left(t_1,\ldots,t_k;t'_1,\ldots,t'_k\right) &= \left(\theta\left(t'_1-t_1\right)\prod_{i=2}^{k}\theta\left(t'_i-t_i\right)\theta\left(t_i-t'_{i-1}\right)\right) \\
&\quad\times\gamma_g^k\left\langle 2\right|\tilde{\sigma}_{23}\left(t'_k\right)\tilde{\sigma}_{31}\left(t_k\right)\mathcal{T}\left[\prod_{i=1}^{k-1}\tilde{\sigma}_{13}\left(t'_i\right)\tilde{\sigma}_{31}\left(t_i\right)\right]\left|1\right\rangle \\
\mathcal{G}^{1,1}_{\tau^+,\tau^-}\left(t_1,\ldots,t_k;t'_1,\ldots,t'_k\right) &= \left(\theta\left(t'_1-t_1\right)\prod_{i=2}^{k}\theta\left(t'_i-t_i\right)\theta\left(t_i-t'_{i-1}\right)\right) \\
&\quad\times\gamma_g^k\left\langle 1\right|\mathcal{T}\left[\prod_{i=1}^{k}\tilde{\sigma}_{13}\left(t'_i\right)\tilde{\sigma}_{31}\left(t_i\right)\right]\left|1\right\rangle
\end{aligned} \tag{4.5}$$

where $\theta\left(t\right)$ is the Heaviside step function. In the above equation, $\mathcal{G}^{2,1}_{\tau^+,\tau^-}$ represents the case where the k-th arriving photon is successfully subtracted, while $\mathcal{G}^{1,1}_{\tau^+,\tau^-}$ corresponds to the case where no photon has been subtracted and all photons exit through the red waveguide output. It should be noted that, since the emitter no longer interacts with input photons after subtracting a photon, the subtracted photon, if any, must be the last photon to interact with the emitter (i.e., the k-th photon in the case of k interacting photons). Additionally, $\tilde{\sigma}_{ij}\left(t\right)$ are atomic transition operators that evolve in time under an effective Hamiltonian H_{eff} according to $\dot{\tilde{\sigma}}_{ij} = i[H_{\text{eff}},\tilde{\sigma}_{ij}]$, starting from their Schrodinger picture counterparts $\sigma_{ij} = \left|i\right\rangle\left\langle j\right|$. The effective Hamiltonian is $H_{\text{eff}} = H_{\text{atom}} - \frac{i}{2}\sum_{\mu=1}^{2}L_\mu^\dagger L_\mu$ where $H_{\text{atom}} = \omega_{13}\sigma_{33} + \left(\omega_{13}-\omega_{23}\right)\sigma_{22}$, with ω_{12} and ω_{23} representing the atomic transition frequencies from ground states $\left|1\right\rangle$ and $\left|2\right\rangle$ to the excited state $\left|3\right\rangle$, respectively. Additionally, $L_1 = \sqrt{\gamma_g}\sigma_{13}$ and $L_2 = \sqrt{\gamma_g}\sigma_{23}$, are the coupling operators that couple the atom to the waveguide modes. Therefore, for $\tilde{\sigma}_{13}$ and $\tilde{\sigma}_{23}$ we have:

$$\tilde{\sigma}_{13}\left(t\right) = \exp\left(-\left(i\omega_{13}+\gamma_g\right)t\right)\sigma_{13} \qquad \tilde{\sigma}_{23}\left(t\right) = \exp\left(-\left(i\omega_{23}+\gamma_g\right)t\right)\sigma_{23} \tag{4.6}$$

Substituting these operators into equation 4.5, gives the following Green's functions:

$$\begin{aligned}\mathcal{G}^{2,1}_{\tau^+,\tau^-}\left(t_1,\ldots,t_k;t'_1,\ldots,t'_k\right) &= \left(\theta\left(t'_1-t_1\right)\prod_{i=2}^{k}\theta\left(t'_i-t_i\right)\theta\left(t_i-t'_{i-1}\right)\right)\\ &\quad\times\gamma_g^k\exp\left(i\omega_{12}t'_k\right)\exp\left(\left(i\omega_{13}+\gamma_g\right)\sum_{i=1}^{k}\left(t_i-t'_i\right)\right)\\ \mathcal{G}^{1,1}_{\tau^+,\tau^-}\left(t_1,\ldots,t_k;t'_1,\ldots,t'_k\right) &= \left(\theta\left(t'_1-t_1\right)\prod_{i=2}^{k}\theta\left(t'_i-t_i\right)\theta\left(t_i-t'_{i-1}\right)\right)\\ &\quad\times\gamma_g^k\exp\left(\left(i\omega_{13}+\gamma_g\right)\sum_{i=1}^{k}\left(t_i-t'_i\right)\right)\end{aligned} \tag{4.7}$$

Each input photon to the photon subtractor can have one of three outcomes: it may be absorbed by the emitter and diverted to the second waveguide mode, absorbed and re-emitted into the same mode, or pass through the atom without interacting with it. Based on this, and utilizing the Green's functions mentioned earlier, we can express the scattering matrix elements introduced in equation 4.4. For the case of one-photon transport, the matrix elements, after transforming to a rotating frame at the atomic transition frequencies, are given by:

$$\begin{aligned}\Sigma_1^1\left(t'_1-t_1\right) &= -\gamma_g\exp\left(\gamma_g\left(t_1-t'_1\right)\right)\\ \Sigma_0^1\left(t'_1-t_1\right) &= \delta\left(t_1-t'_1\right)-\gamma_g\exp\left(\gamma_g\left(t_1-t'_1\right)\right)\end{aligned} \tag{4.8}$$

Additionally, for N-photon transport, the scattering matrix elements can be expressed as a product of the single-photon elements given above, with an additional multi-photon kernel (MPK) that accounts for photon reordering due to saturation effects:

$$\Sigma_j^N\left(t_1,\ldots,t_N;t'_1,\ldots,t'_N\right) = \left(\left[\prod_{i=1}^{j-1}\Sigma_0^1\left(t'_i-t_i\right)\right]\Sigma_1^1\left(t'_j-t_j\right)+\mathrm{MPK}\right)\left[\prod_{i=j+1}^{N}\delta\left(t'_i-t_i\right)\right] \tag{4.9}$$

where:

$$\mathrm{MPK}=\sum_{A_j}\left[\left[\prod_{\substack{i=1\\A_j(i)=1}}^{|A_j|}\Sigma^1_{\delta_{ij}}\left(t'_i-t_i\right)\right]\times\left[\prod_{\substack{i=1\\A_j(i)>1}}^{|A_j|}\left[-\gamma_g\left(\prod_{k=1}^{A_j(i)-1}\delta\left(t_{B(i-1)+k+1}-t'_{B(i-1)+k}\right)\right)\times\exp\left(\gamma_g\left(t_{B(i-1)+1}-t'_{B(i-1)+A_j(i)}\right)\right)\right]\right]\right] \tag{4.10}$$

In the above expression, δ_{ij} is the Kronecker delta function, A_j is an ordered set of fewer than j natural numbers whose sum is j, $|A_j|$ denotes its cardinal, and B is a set whose elements are the partial sums of the first i elements of A_j, i.e., $B(i) = \sum_{k=1}^{i} A_j(k)$. For the case where no photon is subtracted, photon-photon interactions involving up to N photons are possible. Therefore, in the above equation, j should be replaced by N, and δ_{ij} should be set to zero. It is worth noting again that the expressions given in equations 4.9 and 4.10 are valid only when the input and output photon arrival times are sorted, and there is exactly one output photon between each pair of input photons (i.e., $t_1 \leq t'_1 \leq t_2 \leq t'_2 \leq \ldots \leq t_N \leq t'_N$), otherwise, the transition amplitude is zero.

4.1.3 Equivalent input-output network model

The proposed PNR detector in Figure 4.1.(b) functions as a quantum input-output network (QION) with one input port and $n+1$ output ports. By neglecting the propagation time of light between the emitters, an equivalent Markovian model for the network can be derived, comprising a higher-order local quantum system coupled to multiple field modes. This is achieved by eliminating the interconnections within the network and calculating an equivalent Hamiltonian along with the coupling operators responsible for the whole network's interaction with the external field modes. This procedure is carried out using the SLH framework introduced in Section 1.2.2. It is important to note that the scattering matrix $\mathbf{S}$ appearing in the SLH formalism differs from the one designated by $\mathbf{\Sigma}$ in the previous section, as the former accounts solely for the direct rerouting of fields without any interaction with the quantum system.

In the scheme shown in Figure 4.1.(b), the circulators directly transmit the right-propagating mode and route the single photons subtracted by the emitters (located to their right) to the vertical waveguide mode. Therefore, when deriving our input-output model, we can eliminate the circulators and assume that each emitter is directly coupled to the vertical waveguide to its left. By doing so, the network consists of n emitters cascaded along a single guided mode (the right-propagating mode). For the ith emitter we have:

$$\begin{gathered} G_i = \left(\mathbf{I}, [L_1, \ldots, L_{n+1}]^T, H^{(i)} = \omega_{13}\sigma_{33}^{(i)} + (\omega_{13} - \omega_{23})\,\sigma_{22}^{(i)}\right) \\ \text{where :} \qquad L_j = \sqrt{\gamma_g}\left(\sigma_{23}^{(i)}\delta_{ij} + \sigma_{13}^{(i)}\delta_{(n+1)j}\right) \end{gathered} \tag{4.11}$$

In the above expression, $\sigma_{kl}^{(i)} = |k\rangle\langle l|$ is the transition operator of the i-th emitter. Applying the cascade rule described in section 1.2.2 to the SLH form given in equation

4.11, the total SLH representation for the PNR detector is found as follows:

$$\begin{aligned} G_T &= G_1 \triangleright \ldots \triangleright G_n \\ &= \left(\mathbf{I}, \sqrt{\gamma_g} \left[\sigma_{23}^{(1)}, \ldots, \sigma_{23}^{(n)}, \sum_{i=1}^{n} \sigma_{13}^{(i)} \right]^T, \left[\sum_{i=1}^{n} H^{(i)} \right] + \frac{\gamma_g}{2i} \left[\sum_{j=2}^{n} \left(\sigma_{31}^{(j)} \sum_{i=1}^{j-1} \sigma_{13}^{(i)} \right) - \text{H.c.} \right] \right) \end{aligned} \tag{4.12}$$

where H.c. stands for Hermitian conjugate terms. To investigate the response of the atomic cascade to propagating light pulses, a modulating filter that generates the intended nonclassical field must also be cascaded to its input [47]. With vacuum as input, the modulator should be capable of generating the desired nonclassical field. One possible realization of such a modulator is a cavity mode, where the coupling to the photon subtractor is defined according to the intended pulse profile. If the input light to the photon subtractor has a multi-temporal mode structure, a separate cavity mode is used for each temporal mode of the input (see section 1.2.2).

4.2 Results and Discussion

In this section, we apply the mathematical models developed in previous section to examine the behavior of single- and multi-photon subtractors when subjected to input fields containing multiple photons. The quantum state of the N-photon input light is expressed in the following general form, where the photons are labeled based on their arrival times:

$$|\psi_{in}\rangle = \mathcal{N} \int_{t_N > \ldots > t_1} \left[g\left(t_1, t_2, \ldots, t_N\right) \prod_{i=1}^{N} a_{in}^{\dagger}\left(t_i\right) dt_i \right] |0\rangle \tag{4.13}$$

In the above expression, g is the N-photon amplitude function and $\mathcal{N}$ is the normalization factor arising from the indistinguishability and sorting of the photons. Additionally, the N-fold integral used is defined as follows:

$$\int_{t_N > \ldots > t_1} dt_N dt_{N-1} \ldots dt_1 := \int_{-\infty}^{\infty} dt_N \int_{-\infty}^{t_N} dt_{N-1} \ldots \int_{-\infty}^{t_2} dt_1 \tag{4.14}$$

In our analysis, we consider various input types based on time correlations and the number of wavepackets. We begin with a single-wavepacket Gaussian-shaped pulsed input, for which the amplitude function is expressed as:

$$g\left(t_1, t_2, \ldots, t_N\right) = \prod_{i=1}^{N} h\left(t_i\right) \tag{4.15}$$

with $h(t) = \sqrt{2/(\delta\sqrt{\pi})}\exp(-i\omega_0 t - 2t^2/\delta^2)$ being the single-photon amplitude function of the Gaussian wavepacket with width δ and carrier frequency ω_0. The normalization factor in this case is given by $\mathcal{N} = \sqrt{N!}$ [44].

4.2.1 Linear analysis

In the linear regime, the system's behavior can be fully predicted through a single-photon transport analysis. In this case, the transfer function of each photon subtractor between its input and each of its two outputs can be determined by taking the Fourier transform of the scattering matrix elements $\Sigma_1^1(t'-t)$ and $\Sigma_0^1(t'-t)$ given in equation 4.8, yielding the well-known Lorentzian-shaped frequency responses $\Sigma_1^1(\omega) = -\gamma_g/(\gamma_g + i\omega)$ and $\Sigma_0^1(\omega) = i\omega/(\gamma_g + i\omega)$ [57], where ω is the detuning from the atomic resonance frequency ω_{13}. Using these transfer functions, we can calculate the probability that a single photon present at the input is subtracted by a cascade of λ emitters (each in their $|1\rangle$-state), as:

$$P_{1,1}^{\lambda} = 1 - \int \left| \left(\Sigma_0^1(\omega)\right)^{\lambda} h(\omega + \omega_{13}) \right|^2 d\omega \tag{4.16}$$

where $h(\omega') = \sqrt{\delta/(2\sqrt{\pi})}\exp\left(-(\omega'-\omega_0)^2\delta^2/8\right)$ is the Fourier transform of $h(t)$, representing the frequency distribution of each single photon. An important point regarding the above expression is that when the single-photon pulse passes through each emitter without being subtracted, it is reshaped according to $\Sigma_0^1(\omega)$, which reduces its likelihood of being absorbed by subsequent emitters. If we have a PNR detector with n emitters, as shown in Figure 4.1.(b), we can use equation 4.16 to calculate the probability of successfully subtracting k photons out of N photons at the input, denoted by $P_{N,k}^n$. This is determined by summing the probabilities of successfully subtracting all possible combinations of k photons out of N photons, while accounting for the fact that after each successful subtraction, the number of active emitters decreases by one, resulting in:

$$P_{N,k}^n = \begin{cases} \left(\prod_{m=0}^{k-1} P_{1,1}^{n-m}\right) \sum_{B_{N-k}^k} \left(\prod_{i=1}^{N-k} \left(1 - P_{1,1}^{n-B_{N-k}^k(i)}\right)\right) & k > 0 \\ \left(1 - P_{1,1}^n\right)^N & k = 0 \end{cases} \tag{4.17}$$

where B_{N-k}^k is an unordered set with $N-k$ elements chosen from $\{0, 1, \ldots, k\}$. If $k = N$ or $k = N-1$, the number of detectors that register a click equals N, resulting in accurate photon counting. Otherwise, there is an error of $k+1-N$ in counting the photons. Therefore, the average error of the detector in counting the input photons can be written

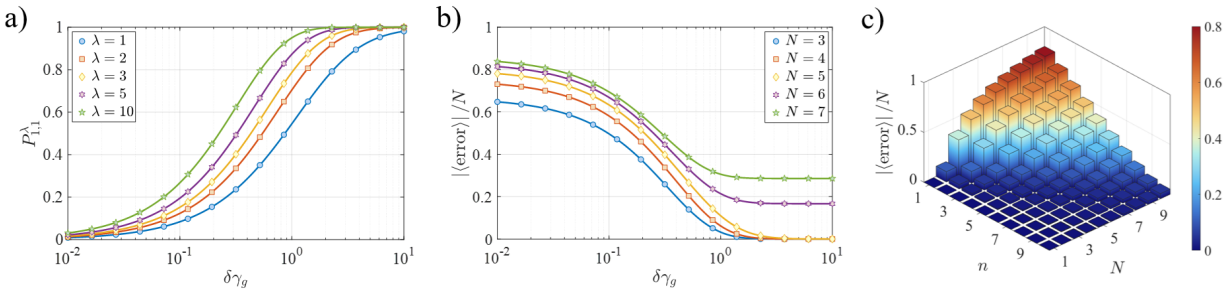


Figure 4.2: (a) Probability of successfully subtracting a single photon by a cascade of λ emitters, based on equation 4.16, (b) Relative error of a PNR detector with a cascade of $n = 4$ emitters, for input pulses with different photon numbers N, and (c) Relative error of a PNR detector as a function of the input photon number N and the number of emitters n for $\delta\gamma_g = 0.5$.

as:

$$\langle \text{error} \rangle = \sum_{k=0}^{\min(n,N-2)} (k + 1 - N)\, P_{N,k}^{n} \tag{4.18}$$

If in an n-emitter PNR detector subjected to an $n+1$ photon pulse any emitter fails to subtract a photon, the resulting photon count will be inaccurate. This occurs because multiple photons may arrive at the last detector, which lacks PNR capability and, regardless of the number of arriving photons, registers only a single click. One approach to increase the precision of the detector is to add additional emitters. This way, if one emitter fails to subtract a photon, other emitters downstream can compensate by subtracting it, ensuring the final count remains accurate. However, as mentioned above, the pulse reshaping occurred during its interaction with upstream emitters makes it harder for downstream emitters to subtract a photon. Figure 4.2 shows the results for the linear regime based on equations 4.16 to 4.18 when the carrier frequency of the input pulses is in resonance with the atomic transition, i.e., $\omega_0 = \omega_{13}$. Parts (b) and (c) are particularly relevant from a design perspective, as they provide insight into the number of emitters required to count photons in the input pulse within a specified error margin. The results are plotted as functions of $\delta\gamma_g$ representing the ratio of the atomic linewidth to the spectral bandwidth of the input pulse.

4.2.2 Nonlinear analysis

In the nonlinear regime, in addition to the pulse shaping discussed above, upstream emitters can also influence the probability of photon subtraction by downstream counterparts through a second mechanism: generating correlations between their scattered photons by forming multi-photon bound states [73, 122]. To investigate this correlation, we first define the zero-delay second-order correlation function $g^{(2)}(0)$ for photons exiting the photon subtractor through the $a_{out,1}$ output mode (see Figure 4.1.(a)). By averaging and normalizing the two-time correlator $G^{(2)}(t_1, t_2)$, the following expression for $g^{(2)}(0)$ is derived for a pulse containing N photons:

$$g^{(2)}(0) = (N-1)^2 \frac{\int G^{(2)}(t,t)\, dt}{\int \left| \int G^{(2)}(t,t')\, dt' \right|^2 dt} \tag{4.19}$$

In the derivation of the above expression, the following relation between the first-order and second-order correlation functions for an N-photon pulse is used:

$$G^{(1)}(t,t) = \frac{1}{N-1} \int G^{(2)}(t,t')\, dt' \tag{4.20}$$

Generation of photon-photon correlations at the $a_{out,1}$ output requires that at least two photons in this output have interacted with the emitter. Since the emitter's interaction with the input photons ceases as soon as a photon is subtracted, such correlations can occur only if no photon is subtracted from an input pulse with at least two photons, or if the third photon or any subsequent photon is subtracted from input pulses with at least three photons. Consequently, here, we study three specific cases: first, when two photons are present at the input and no photon is subtracted, second, when three photons are present at the input and no photon is subtracted, and third, when three photons are present at the input and the third photon is successfully subtracted. The derived scattering matrix elements for two- and three-photon inputs are provided in Appendix C. As we will show, this analysis provides valuable insights into the behavior observed during nonlinear N-photon transport through a cascaded system.

Using the derived scattering matrix elements given in equation 4.9, the amplitude function of photons after interacting with a single emitter, for the case where the j-th photon is subtracted (denoted as $g'_{N,j}(t'_1, \ldots, t'_N)$), can be expressed as:

$$g'_{N,j}(t'_1, \ldots, t'_N) = \int_{t'_{N-1}}^{t'_N} dt_N \ldots \int_{t'_1}^{t'_2} dt_2 \int_{-\infty}^{t'_1} dt_1 \left[\sum_{perm_N} \Sigma_j^N \left(t_1, \ldots, t_N; t'_{perm_N(1)}, \ldots, t'_{perm_N(N)} \right) \right] g(t_1, \ldots, t_N) \tag{4.21}$$

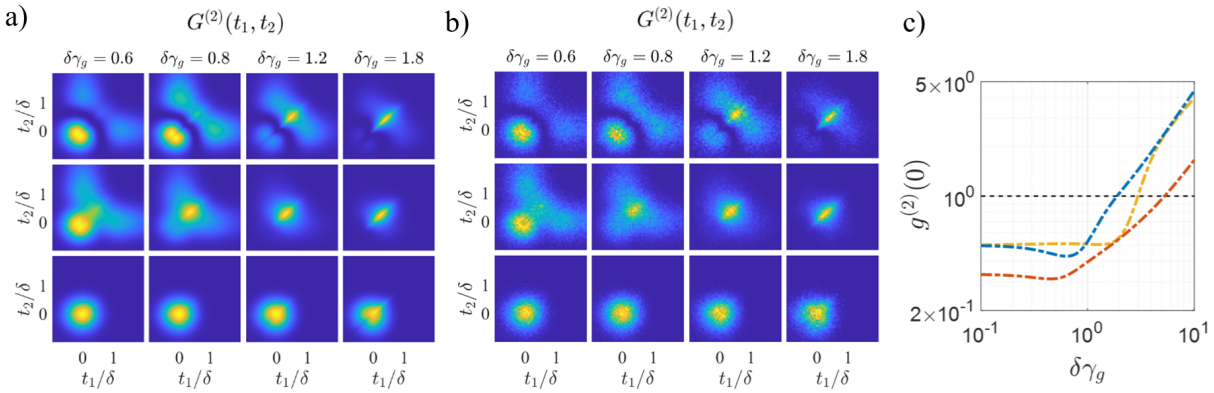


Figure 4.3: (a) Second-order correlation of the output photons at the $a_{out,1}$ mode of a single-emitter photon subtractor, shown for various values of $\delta\gamma_g$. The first row corresponds to a two-photon input with no photon subtracted, the second row to a three-photon input with no photon subtracted, and the third row to a three-photon input where the third photon is subtracted. (b) Same results as in (a), obtained using the Monte-Carlo method by averaging across 50,000 trajectories. (c) Zero-delay single-time correlation function $g^{(2)}(0)$ as a function of $\delta\gamma_g$ for the three cases mentioned above, represented by the blue, red, and yellow curves, respectively.

where $perm_N$ denotes a permutation of numbers 1 to N. This amplitude function can be used to derive the second-order correlation of the output photons in the form:

$$G^{(2)}\left(t'_1, t'_2\right) = N\left(N-1\right)\int \left|g'_{N,j}\left(t'_1,\ldots,t'_N\right)\right|^2 dt'_3\ldots dt'_N \tag{4.22}$$

In addition, the probability that the j-th photon is subtracted from an N-photon input pulse is given by:

$$P_j^N = \int \left|g'_{N,j}\left(t'_1,\ldots,t'_N\right)\right|^2 dt'_1\ldots dt'_N \tag{4.23}$$

Figure 4.3 shows the second-order autocorrelation function of the output photons for the cases described below equation 4.20. Each plot in parts (a) and (b) of the figure is normalized to its maximum value for improved visual clarity. As can be seen, in all parts of the figure, the output light in all three cases exhibits some degree of bunching in the strong interaction regime, where $\delta\gamma_g > 1$. This phenomenon arises from the enhanced two-photon transition due to stimulated emission [71]. The generated anti-bunching observed

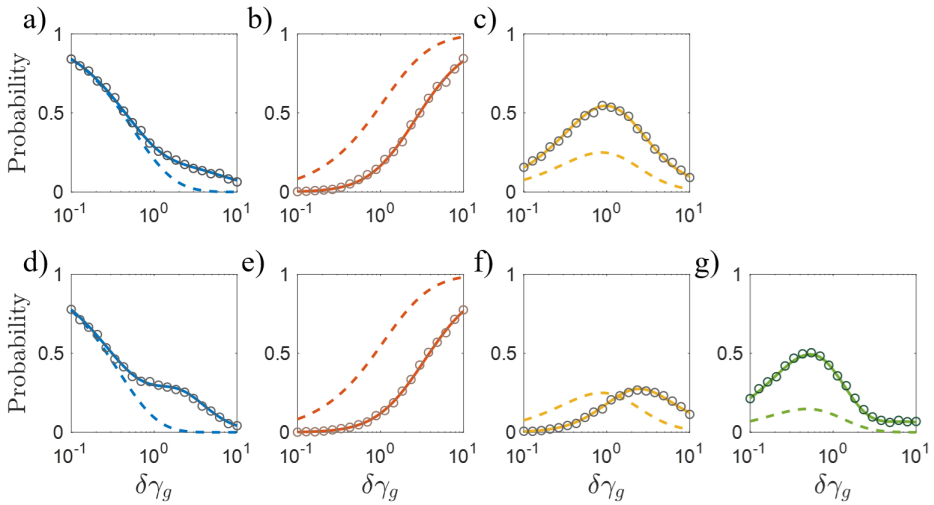


Figure 4.4: (a, b, c) Probabilities of subtracting no photon, the first photon, and the second photon from a two-photon input, respectively. (d, e, f, g) Probabilities of subtracting no photon, the first photon, the second photon, and the third photon from a three-photon input, respectively. The solid and dashed lines represent the nonlinear and linear analytical solutions, respectively, while the circle markers denote the numerical solutions obtained using the quantum trajectory method, averaged across 2000 trajectories.

in the weak interaction regime with $\delta\gamma_g < 1$ arises when one of the two incident photons is absorbed by the emitter, delaying its re-emission, while the second photon simply passes through without interacting. The numerical results are obtained through simulations of the quantum network described in section 4.1.3 using the quantum trajectory method with the QuTiP toolbox in Python, showing good agreement with their analytical counterparts.

In Figure 4.4, for the two cases of two and three input photons, the probabilities of different outcomes are presented, including the possibilities of subtracting no photon or subtracting each of the contained photons in the input pulse based on their arrival order. The nonlinear solutions are calculated from equation 4.23. For the linear solution, the probability of subtracting no photon out of N photons is given by $\left(1 - P^1_{1,1}\right)^N$, and the probability of subtracting the j-th photon is given by $\left(1 - P^1_{1,1}\right)^{j-1} P^1_{1,1}$, where $P^1_{1,1}$ is determined using equation 4.16. As seen in parts (a) and (d) of the figure, in the weak interaction regime where $\delta\gamma_g < 1$, the linear model can predict the failure probability of the process—resulting in no photon being subtracted—with reasonable precision. However, as shown in the other parts of the figure, the linear solution cannot reliably determine which

photon will be subtracted. This occurs due to nonlinear scattering induced by atomic saturation, leading to the reordering of the scattered photons. The first arriving photon excites and saturates the atom but is routed to the other waveguide mode only after the second photon has passed. Another essential observation from this figure is that in the strong coupling regime where the probability of subtracting no photon approaches zero, the first photon is almost deterministically subtracted, as predicted by both linear and nonlinear models. As described in Section 1.1.2, this process temporally entangles the subtracted photon with the remaining photons, ensuring that the subtracted photon is always detected prior to the remaining ones. This effect has been experimentally confirmed by Rosenblum et al. [118]. The higher failure rate of photon subtraction predicted by the nonlinear model arises from the stimulated emission effect when multiple photons interact with the atom within its response time. This interaction leads to the formation of bound states at the $a_{out,1}$ output, which is not accounted for in the linear model.

So far, we have investigated the performance of SPRINT-based photon subtractors for inputs with different photon numbers, all of which were in a single temporal mode. We observed that the width of the input pulses, relative to the atomic response time, plays a key role in the successful subtraction of photons. Now, we will explore the system's response to inputs with multiple modes. First, to examine how the photons' overlap affects the validity of the linear solution, let us consider a two-photon state consisting of two single-photon Gaussian wavepackets separated by a time interval Δ. The symmetrized amplitude function for this state will be:

$$g\left(t_1, t_2, \ldots, t_N\right) = \sum_{perm_N} \left[\prod_{i=1}^{N} h\left(t_{perm_N(i)} - i\Delta\right)\right] \tag{4.24}$$

In this case, the photons have partial indistinguishability, and the normalization factor is $\mathcal{N} = 1/\sqrt{\text{permanent}\left(\mathcal{S}\right)}$, where $\mathcal{S}$ is the indistinguishability matrix, with its elements given by the inner product of different wavepackets [136], i.e., $\mathcal{S}_{ij} = \langle h(t - i\Delta) \mid h(t - j\Delta)\rangle$. For the two-photon input with Gaussian wavepackets introduced earlier, this results in $\mathcal{N} = 1/\sqrt{1 + \exp(-2\Delta^2/\delta^2\ )}$. By structuring the input in this way, it becomes possible to investigate the system's response in both linear and nonlinear regimes simply by adjusting the parameter Δ. When $\Delta \gg \delta$ and $\Delta \gg 1/\gamma_g$, only one photon interacts with the system at a time, resulting in a linear response. For smaller values of Δ, two-photon effects may arise, leading to a nonlinear response. In the limit of $\Delta = 0$, the input resembles a two-photon pulse within a single wavepacket, as considered before. The results shown in Figure 4.5 correspond to the case of two-photon input. As Δ increases, leading to a lower overlap between the photons, the results converge to the linear solution. Additionally, as seen in

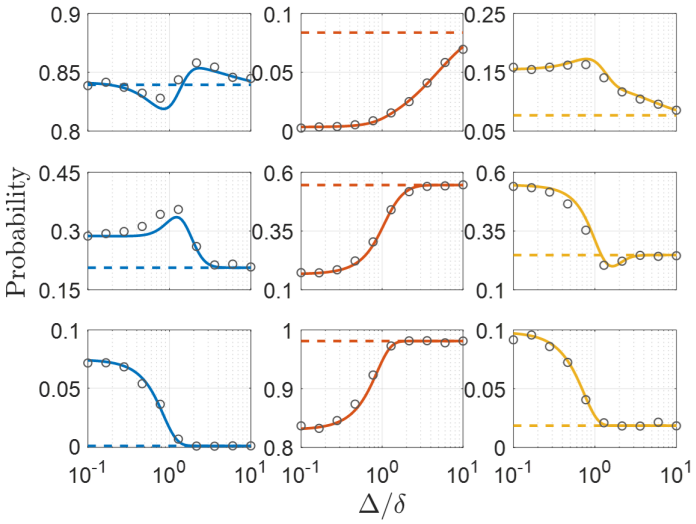


Figure 4.5: Probabilities of subtracting no photon (first column), the first arriving photon (second column), and the second arriving photon (third column) from two overlapping photons as a function of their separation time. First, second, and third row correspond to the weak interaction ($\delta\gamma_g = 0.1$), intermediate interaction ($\delta\gamma_g = 1$), and strong interaction ($\delta\gamma_g = 10$) regimes, respectively. Solid lines represent analytical results, while dots indicate numerical results obtained using the Monte Carlo method, averaged over 10,000 trajectories. Dashed lines correspond to linear solutions.

part (a) of the figure, in the weak interaction regime ($\delta\gamma_g \ll 1$), the linear solution for the success probability of the photon subtractor remains valid with high precision, regardless of the amount of overlap. This is because, in this regime, the probability of two-photon interactions remains low, even when photons arrive at the atom within a short time interval.

To further verify the accuracy of our analytical and numerical models for inputs with more than one mode, particularly those that exhibit correlations or further anti-correlations compared to Fock-state inputs, we consider the following two-mode inputs:

$$\begin{aligned} g_1(t_1,t_2) &= h_0(t_1)\,h_0(t_2) + h_1(t_1)\,h_1(t_2) \qquad (a \\ g_2(t_1,t_2) &= h_0(t_1)\,h_0(t_2) - h_1(t_1)\,h_1(t_2) \qquad (b \end{aligned} \tag{4.25}$$

where $h_0(t)$ and $h_1(t)$ are the zero-th and first-order 1D Hermite-Gauss functions of width δ, respectively, which are defined generally for the n-th order as $h_n(t) = \sqrt{1/2^{n-1}n!\sqrt{\pi}\delta} \times \exp(-2t^2/\delta^2)\,\mathrm{H}_n(2t/\delta)$, with $\mathrm{H}_n(t)$ being the n-th order Hermite polynomial. As seen in the first column of parts (a) and (b) of Figure 4.6, the amplitude functions given in equation

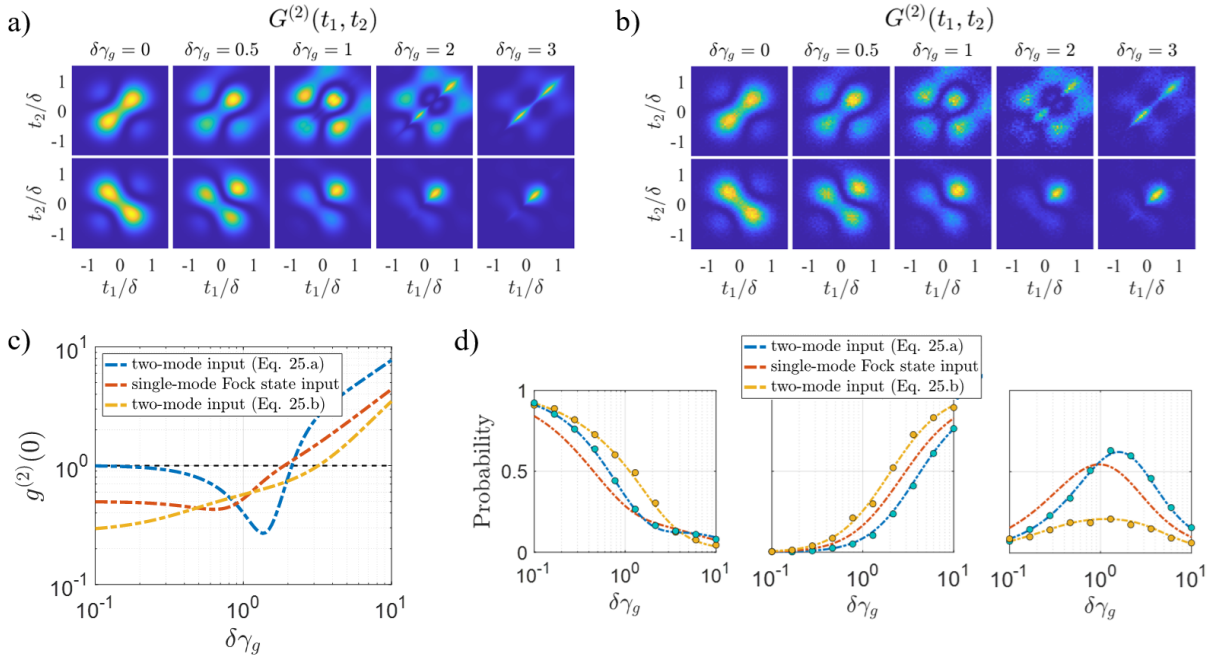


Figure 4.6: (a) Second-order correlation of the output photons at the $a_{out,1}$ mode of a single-emitter photon subtractor, shown for various values of $\delta\gamma_g$. The first and second rows corresponds to a bunched and anti-bunched two-photon input with amplitudes given in equations 4.25.a and 4.25.b, respectively. (b) Same results as in (a), obtained using the Monte-Carlo method by averaging across 50,000 trajectories. (c) Zero-delay single-time correlation function $g^{(2)}(0)$ of the output light as a function of $\delta\gamma_g$ for these two correlated input states, along with the uncorrelated input, as described in equation 4.15. (d) Left to right: probability of successfully subtracting a single photon, the first arriving photon, and the second arriving photon, respectively. The circle markers denote the numerical solutions obtained using the quantum trajectory method, averaged across 1,000 trajectories.

4.25 generate bunched and anti-bunched light, respectively, compared to the single-mode two-photon Fock state. The correlation between the output photons, in cases where no photon is subtracted by the photon subtractor, is shown in the subsequent columns of Figures 4.6.(a) and 4.6.(b), as well as in Figure 4.6.(c). As shown in this figure, bound states dominate the output in the strong interaction regime for both input states. Additionally, in the intermediate interaction regime ($\delta\gamma_g \sim 1$), the bunched input exhibits stronger anti-bunching. This occurs because, when photons arrive close together, the probability of only one photon interacting with the atom increases, while the other photon is directly

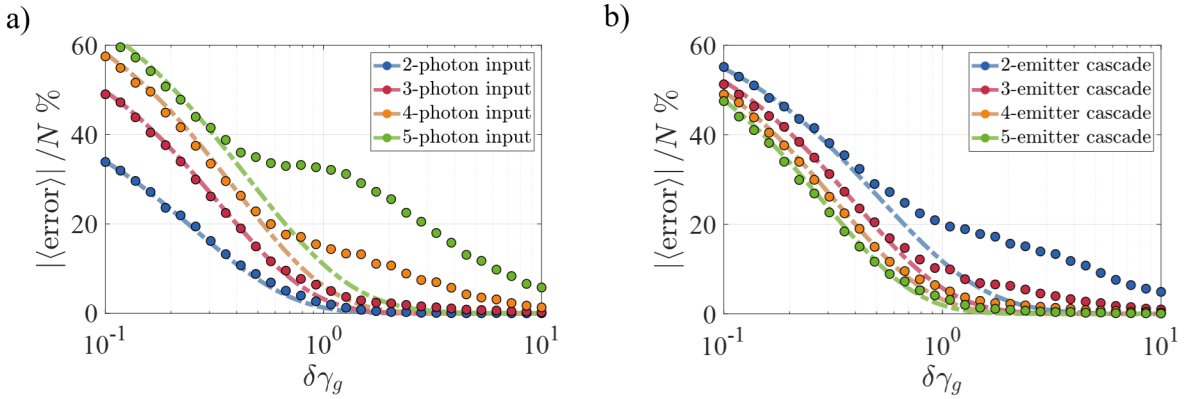


Figure 4.7: (a) Relative error of a PNR detector consisting of a cascade of $n = 4$ quantum emitters when subjected to Gaussian input pulses with different photon numbers. (b) Relative error of PNR detectors with cascades of $n = 2$ to $n = 5$ quantum emitters when subjected to Gaussian input pulses with $N = 3$ photons. The dash-dotted lines indicate the results from the linear analysis, while the dots represent nonlinear results calculated using the quantum trajectory method, averaged across 5,000 trajectories.

transmitted due to atomic saturation. In Figure 4.6.(d), the probabilities of subtracting no photon, the first photon, and the second photon are plotted for these input pulses. For the bunched input, there is a higher probability that the subtracted photon is detected after the transmitted photon due to the small arrival-time difference between the photons (see the rightmost plot). Additionally, the total success rate of subtraction is lower for both bunched and anti-bunched inputs compared to the single-mode Fock state input (see the leftmost plot). This occurs because, in the anti-bunched case, the effective interaction time of each photon with the emitter is shorter. In the bunched case, the reduction arises because the second photon arrives shortly after the first, decreasing its likelihood of interacting with the emitter due to saturation.

As we observed in the previous results, the stimulated emission effect in the nonlinear regime prevents single emitters from successfully subtracting photons by inducing the re-emission of the absorbed photon into the same waveguide mode. Additionally, it generates bound states that due to their bunching are more difficult to be re-routed by the next emitter in the cascade. Therefore, we expect the precision of a PNR detector to be lower than that predicted by the linear model (see Figure 4.2) in the region where these bound states are generated. However, increasing the number of photon subtractors in the cascade relative to the number of input photons can enhance this precision, leading to highly accurate detectors, particularly in the strong interaction regime. This is confirmed by

Figure 4.7, which shows the relative error of a detector with different number of emitters and input photons as predicted by both linear and nonlinear models.

4.3 Comparison with Conventional PNR Detection Scheme

To evaluate the photon-number-resolving performance of the proposed detector, we compare it against conventional PNR techniques that rely on linear optical splitting of the input pulse across multiple single-photon detectors. In these approaches, the photons are distributed across several detector pixels, with the ideal case being a uniform distribution. The total photon number is then estimated by counting the number of detectors that register a click. When the number of detector pixels significantly exceeds the number of incident photons, the probability of two photons arriving at the same detector becomes negligible, enabling accurate photon counting. Spatial demultiplexing of photons in these methods is typically achieved using balanced beamsplitter trees [103], cascaded polarizing beamsplitters and half-wave plates [130], multipixel sensor grids [48], or cascades of waveguide-coupled superconducting nanowire single-photon detectors (SNSPDs) [21]. Figure 4.8.(a) illustrates a typical setup consisting of a cascade of beamsplitters with reflectivities R_1 to R_n, where each beamsplitter reflects a portion of the incident light to a single-photon detector, and the final detector collects the fully transmitted light. The probability that an incoming photon is routed to the i-th detector in this setup is given by:

$$P_i = \begin{cases} R_i & i = 1 \\ R_i \prod_{j=1}^{i-1} (1 - R_j) & 1 < i < n+1 \\ \prod_{j=1}^{i-1} (1 - R_j) & i = n+1 \end{cases} \tag{4.26}$$

To describe the probability that k detectors out of $n+1$ register a click when N photons are sent into the input of the beamsplitter cascade, we model the system as a multinomial distribution over the $n+1$ detectors, where each detector i is associated with a photon-routing probability P_i. This leads to the following expression for the average number of clicks registered by the detectors:

$$\langle \text{clicks} \rangle = N! \sum_{k=0}^{\min(n+1,N)} \sum_{A_{n+1}^{N,k}} \left[\left(\prod_{i=1}^{n+1} P_i^{A_{n+1}^{N,k}(i)} \right) \Big/ \left(\prod_{i=1}^{n+1} A_{n+1}^{N,k}(i)! \right) \right] \tag{4.27}$$

where $A_{n+1}^{N,k}$ is an ordered set of $n+1$ non-negative integers whose sum is N, and exactly k of the elements are nonzero.

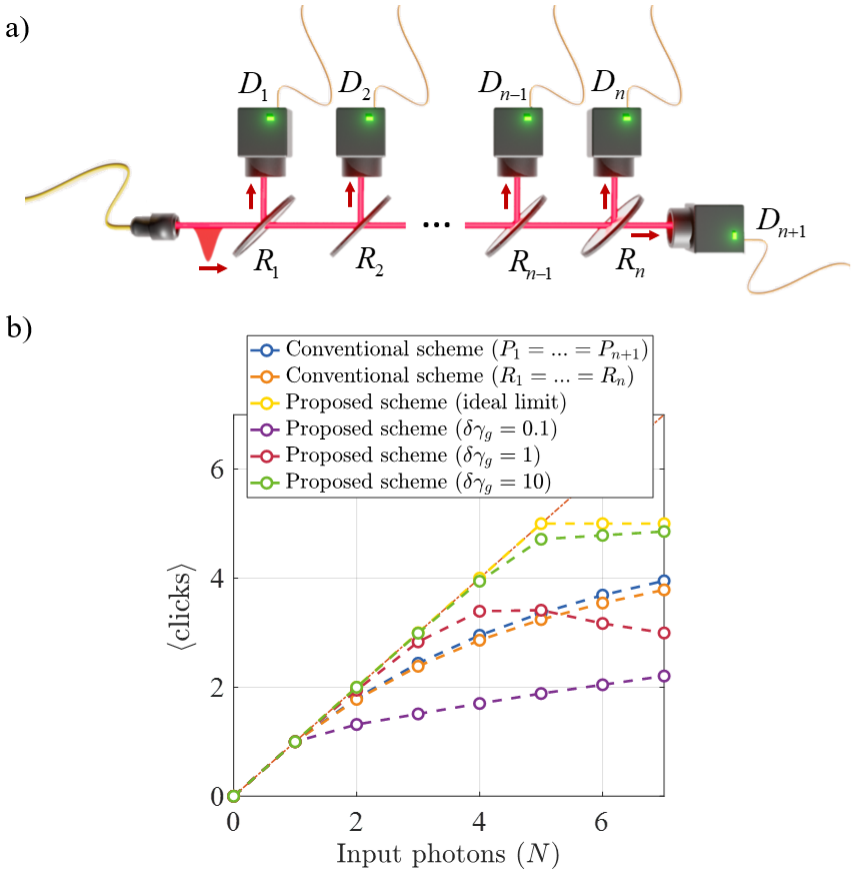


Figure 4.8: (a) Schematic of a conventional PNR detector, which spatially distributes input photons among multiple single-photon detectors using a cascade of beamsplitters. (b) Performance comparison between the conventional scheme achievable with $n = 4$ beamsplitters and the photon-subtraction-based scheme with a cascade of $n = 4$ quantum emitters, shown for different values of the parameter $\delta\gamma_g$. The results for the proposed scheme are calculated using the quantum trajectory method, averaged across 5,000 trajectories.

Figure 4.8.(b) shows the detector response curve, which plots the average number of detector clicks as a function of the number of incident photons for an input pulse prepared in a Fock state with photon number N. The blue curve represents the most accurate response achievable with the conventional scheme shown in Figure 4.8.(a). This optimal response is obtained when the beamsplitter reflectivities are configured such that photons are uniformly distributed among the detectors—that is, when $P_1 = P_2 = \ldots = P_{n+1}$, as in the case of a balanced beamsplitter tree. The orange curve corresponds to the response of

the same conventional scheme, but with beamsplitters of equal reflectivity—that is, when, $R_1 = R_2 = \ldots = R_n$, which is equivalent to the case of a PNR detector using a series of SNSPDs placed along a waveguide [21]. In this case, the reflectivity value is chosen to maximize the precision of the detector. The other curves correspond to the response of the proposed detector for various values of the parameter $\delta\gamma_g$. Both approaches are assumed to use the same number of single-photon detectors, i.e., five. As shown, the SPRINT-based detector proposed in this chapter outperforms the conventional scheme when $\delta\gamma_g$ reaches values on the order of approximately 10. Assuming an input pulse width of 10 ns - which corresponds to the typical dead time of currently available single-photon detectors based on avalanche photodiodes or SNSPDs - this condition is satisfied when the coupling rate γ_g reaches 1 GHz. At the same time, coupling rates of several gigahertz have been reported for solid-state emitters coupled to chiral photonic crystal waveguides [3, 126], which highlight the feasibility of implementing the proposed approach for high-precision PNR detection with currently available technologies.

Chapter 5

Two-Way Two-Emitter Cascade for Selective Single-Photon Subtraction

As mentioned before, one potential application of deterministic single-photon subtractors is in PNS attacks on QKD. While quantum cryptography schemes based on single photons as information carriers are theoretically proven to be unconditionally secure, in practice, their security might be compromised due to implementation non-idealities. One such nonideality involves using highly attenuated laser pulses instead of one-photon states [11]. In this case the adversary eavesdropper can gain partial access to the communicated data by splitting a single photon from the inadvertently-occurring multi-photon states without neither changing the signal rate at receiver's end nor leading to error in the sifted key. Previously, it was suggested that PNS needs to include a quantum non-demolition (QND) measurement to determine number of photons in each pulse to distinguish multi-photon states, which is experimentally demanding [67]. In this chapter, we propose a photon subtraction scheme consisting of two cascaded Λ-emitters coupled to a chiral waveguide [120] which selectively subtracts a single photon only from multiphoton states eliminating the need for the QND measurement. We theoretically model and numerically simulate our photon subtractor to evaluate its performance through analyzing photon number statistics at different output ports of the device.

5.1 Description of the Proposed Scheme

The proposed scheme based on a cascade of photon subtraction is shown in Figure 5.1. Two identical Λ-type quantum emitters are interacting with a chiral waveguide where each

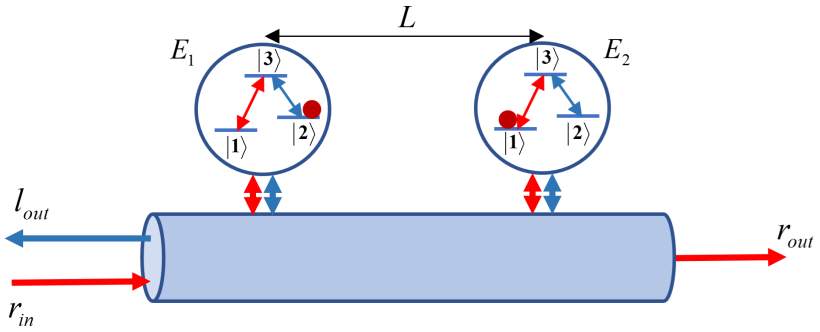


Figure 5.1: Diagram of the proposed photon subtraction system based on two identical three-level quantum emitters coupled to a chiral waveguide. The initial state of the two emitters is also shown.

counterpropagating mode of light is selectively coupled to only one of the two possible ground to excited state transitions i.e. $|1\rangle \rightarrow |3\rangle$ or $|2\rangle \rightarrow |3\rangle$ [77]. The corresponding transitions and propagation directions, which are coupled to each other, are indicated by arrows of the same color in this figure. Emitter E_1 is initially prepared at its second ground state $|2\rangle$ while E_2 is initially at $|1\rangle$. The separation length between the emitters is L and the input light, currently assumed to be a laser pulse containing an n-photon Fock state, is sent to the right propagating mode input r_{in}. According to the initial state of the emitters, since E_1 is initially transparent to the right propagating light, the input pulse first interacts with E_2. This interaction results in subtraction of a single photon which then propagates in left direction. This behavior was explained in section 1.1.2. According to that discussion, when the input light resonantly interacts with an emitter initially in one of its ground states (e.g., state $|1\rangle$ shown in the figure), a destructive interference occurs in the weak excitation limit between the input photon and the emitted radiation from the $|1\rangle - |3\rangle$ transition dipole. This interference prevents the emitter from decaying back to state $|1\rangle$ and transmitting the arriving photon. Consequently, the atom deterministically decays to its other ground state, resulting in the absorbed photon being diverted to the opposite direction and a ground state flip of the emitter [119].

The subtracted photon by E_2 is then reflected back into the right direction as it toggles the state of E_1 from $|2\rangle$ to $|1\rangle$. After this ground state flip, E_1 would be no more transparent to the input light. It will subtract a second photon from the input (if there is one), sending it to the left propagating mode to exit from l_{out} output mode, while E_1 goes back into state $|2\rangle$. This whole process leaves both emitters at state $|2\rangle$ and makes them transparent to the remaining photons from the input. Thus, an output pulse containing $n-1$ photons leaves the subtractor from the r_{out} output. The important feature of this proposed scheme

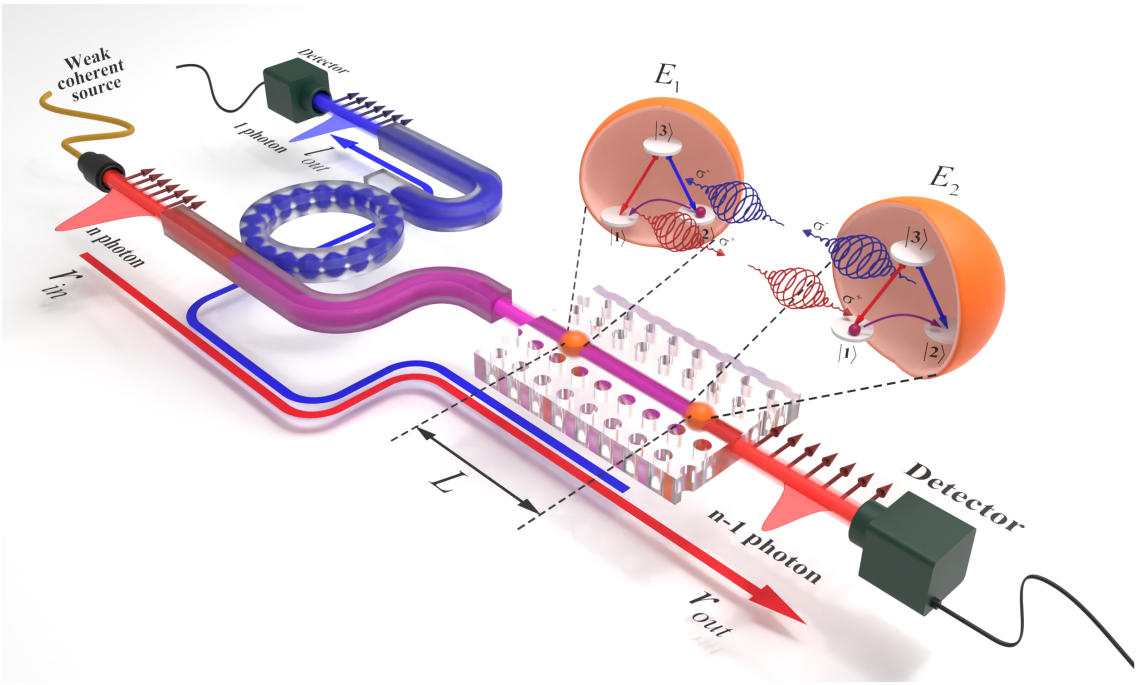


Figure 5.2: Conceptual diagram illustrating a potential implementation of the proposed device, integrating solid-state quantum emitters coupled to a nanophotonic chiral waveguide and a ring resonator drop filter, to subtract a single photon and divert it to a different pathway.

is that it selectively subtracts the second arriving photon. If the input pulse contains only one photon, no photon can be subtracted by E_1. This single input photon after two consecutive reflections by E_2 and E_1 exits from r_{out}. We refer to this configuration as a two-way cascade because, unlike the cascade described in Chapter 4, where only photons emitted into the right propagating mode could interact with downstream emitters (while those emitted into the left propagating mode were extracted by circulators), here photons emitted into both the right and left propagating modes can interact with emitters located to the right and left of the emitting atom, respectively. Figure 5.2 illustrates a potential realization of the proposed scheme featuring two solid-state quantum emitters coupled to a nanophotonic chiral waveguide. Additionally, a ring resonator drop filter [109] is used in the left input/output port of the waveguide enabling the redirection of the subtracted photon to a different pathway. This configuration requires the non-degeneracy of the ground energy levels of the emitter, ensuring that the subtracted photon possesses a different frequency compared to the input photons.

5.2 Theoretical Modeling

The above-described scheme can be modeled as an input-output quantum network, where each of the counterpropagating modes of light is represented by a cascaded quantum system as shown in the block diagram of Figure 5.3. In the context of QKD attack, the sender (Alice) sends light pulses to the input mode r_{in}, the subtracted photon goes to the eavesdropper (Eve) who employs detector D_2, and the remaining pulse is received by the receiver (Bob), where detector D_1 is utilized. Phase delay modules ϕ are inserted between the emitters to account for the finite propagation time along distance L. Denoting the speed of light in the waveguide and carrier frequency of the input pulse by v and ω, respectively, one can write the phase delay as $\phi = \omega L/v$. It should be noted that in general, free propagation of the field between two cascaded components of the network results in a non-Markovian dynamic of the composite system. However, when the propagation time is much smaller than other time scales of the system including emission time of the emitters to the channel and width of the light pulses, one can model the effect of free propagation on the field by simply applying a lag phase to it and derive an approximate Markovian model for the network [24, 45].

For the single wavepacket input pulse in our system, the interaction of the pulse with the quantum system can be studied by adding a single one-sided virtual cavity to the right propagating cascade, as shown in the figure [63]. In this approach, as described in section 1.2.2, the time-dependent transmissivity of the cavity mirror is chosen to match the temporal profile of the light pulse, and the cavity is initially prepared in a same quantum state as that of the wavepacket. Considering feedback loops which bring into account diverting of single photons between different modes during the photon subtraction process, the two cascaded models are then concatenated to find the Hamiltonian H and Lindblad operators L_i's for the whole system. Then the master equation as given in equation 3.15 can be solved to calculate the evolution of the system over time.

Following the SLH framework described in section 1.2.2, the SLH triples for the input cavity and phase delay module are $G_{cavity} = (I, g_u^* a, 0)$ and $G_{delay} = \left(e^{i\phi} I, 0, 0\right)$ where I is the identity matrix and a is the annihilation operator of the cavity mode. Given the temporal profile of the input pulse $u(t)$, the cavity coupling to the channel g_u is determined according to equation 1.12. Moreover, for the emitter $E_i (i = 1, 2)$ the SLH triple for the right and left propagating fields can be written as $G^{(i)}_{emitter\,(R)} = \left(I, \sqrt{\gamma_g}\sigma^{(i)}_{13}, H^{(i)}_{sys}\right)$ and $G^{(i)}_{emitter\,(L)} = \left(I, \sqrt{\gamma_g}\sigma^{(i)}_{23}, 0\right)$, respectively, where $H^{(i)}_{sys} = \omega_{13}\sigma^i_{33} + (\omega_{13} - \omega_{23})\,\sigma^i_{22}$ is the Hamiltonian of the emitter lumped into the right propagating mode and γ_g is the atomic emission rates to the guided modes. $\sigma^{(i)}_{jk} = |j\rangle\langle k|$ in these expressions is transition operator

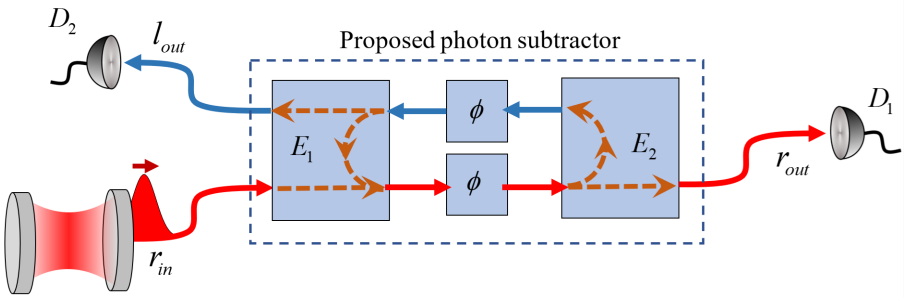


Figure 5.3: Quantum input-output network block diagram for the proposed scheme.

of emitter E_i and ω_{13} (ω_{23}) is transition frequency from ground state $|1\rangle$ ($|2\rangle$) to the excited state $|3\rangle$. The total SLH triple G_T then can be written by cascading of the subsystems in R and L modes i.e. G_R and G_L and concatenating of the derived triples:

$$\begin{aligned} G_R &= G^{(2)}_{emitter\,(R)} \lhd G_{delay} \lhd G^{(1)}_{emitter\,(R)} \lhd G_{cavity} \\ G_L &= G^{(1)}_{emitter\,(L)} \lhd G_{delay} \lhd G^{(2)}_{emitter\,(L)} \\ G_T &= G_R \boxplus G_L \end{aligned} \tag{5.1}$$

The above calculation results in the following effective Hamiltonian and Lindblad operators for the whole network:

$$\begin{aligned} H &= H^{(1)}_{sys} + H^{(2)}_{sys} + \tfrac{i}{2}\left(\gamma_g\left(\sigma^{(1)}_{31}\sigma^{(2)}_{13} + \sigma^{(1)}_{23}\sigma^{(2)}_{32}\right)e^{-i\phi} + \sqrt{\gamma_g}g_u\left(\sigma^{(1)}_{13}a^\dagger + a^\dagger\sigma^{(2)}_{13}e^{-i\phi}\right) - \text{H.c.}\right) \\ L_0(t) &= \sqrt{\gamma_g}\left(\sigma^{(2)}_{13} + \sigma^{(1)}_{13}e^{i\phi}\right) + g^*_u a e^{i\phi} \\ L_1(t) &= \sqrt{\gamma_g}\left(\sigma^{(1)}_{23} + \sigma^{(2)}_{23}e^{i\phi}\right) \end{aligned} \tag{5.2}$$

5.3 Simulation Results and Discussion

When solving the master equation, the operators $L_0(t)$ and $L_1(t)$ in the SLH representation of the network (equation 5.2), will be responsible for the system collapse when either of detectors D_1 or D_2 detect an output photon, respectively. Therefore, using the Monte-Carlo wave function method (MCWF) to solve the problem one would be able to find the photon number statistics at each output of the system by counting the number of collapses occurred according to each of these two collapse operators [88]. In addition to the

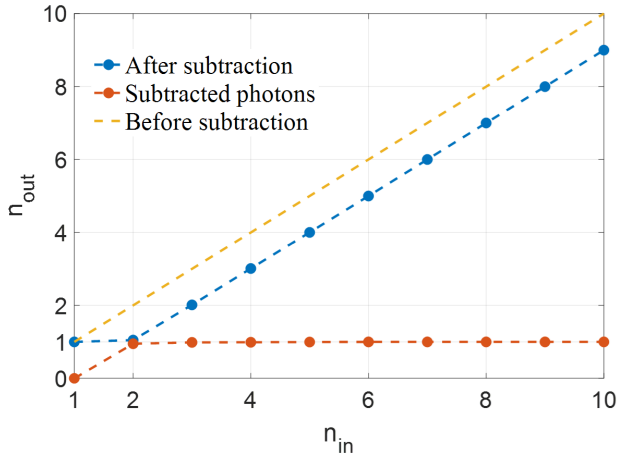


Figure 5.4: Photon subtraction from pulsed Fock state ($\tau = 100/\gamma_g$).

above Lindblad operators, one can consider four more collapse operators $L_2(t) = \sqrt{\gamma_{13}}\sigma_{13}^{(1)}$, $L_3(t) = \sqrt{\gamma_{23}}\sigma_{23}^{(1)}$, $L_4(t) = \sqrt{\gamma_{13}}\sigma_{13}^{(2)}$, and $L_5(t) = \sqrt{\gamma_{23}}\sigma_{23}^{(2)}$ to account for spontaneous emission of the emitters to the free space, where γ_{ij} is rate of atomic spontaneous decay from excited state $|j\rangle$ to ground state $|i\rangle$. Moreover, operators $L_6(t) = \sqrt{\gamma_{2\text{deph}}}\sigma_{22}^{(1)}$, $L_7(t) = \sqrt{\gamma_{3\text{deph}}}\sigma_{33}^{(1)}$, $L_8(t) = \sqrt{\gamma_{2\text{deph}}}\sigma_{22}^{(2)}$, and $L_9(t) = \sqrt{\gamma_{3\text{deph}}}\sigma_{33}^{(2)}$ can be used to bring into account the decoherence effect due to pure dephasing of levels $|2\rangle$ and $|3\rangle$ with respect to $|1\rangle$ with rates $\gamma_{2\text{deph}}$ and $\gamma_{3\text{deph}}$, respectively [38]. Here, we use QuTiP package in python to implement the MCWF method and examine the photon number statistics. The input pulse in our simulations is supposed to be of Gaussian shape with temporal envelope $u(t) = \exp\{2t^2/\tau^2\} \Big/ \sqrt[4]{\pi\tau^2/4}$.

To verify that the proposed design is functioning as intended, we initially consider the input light as a Fock state pulse with a varying number of photons n_{in}. Results are presented in Figure 5.4. The pulse duration τ is chosen to be much larger than the emission time to the waveguide mode $(1/\gamma_g)$. As depicted in this figure, in the case of a single-photon input pulse, no photon is extracted by the subtractor, as expected. Conversely, when there is more than one photon, exactly one photon is subtracted, and the remaining photons are transmitted. Running the simulation with different phase values ϕ reveals that the device's operation is independent of the phase delay and, consequently, the distance between the emitters L. Therefore, if the emitters are sufficiently close to each other to ensure that the propagation delay time between them is significantly smaller than the pulse width and emission time $1/\gamma_g$, we anticipate the proposed scheme to function effectively, regardless

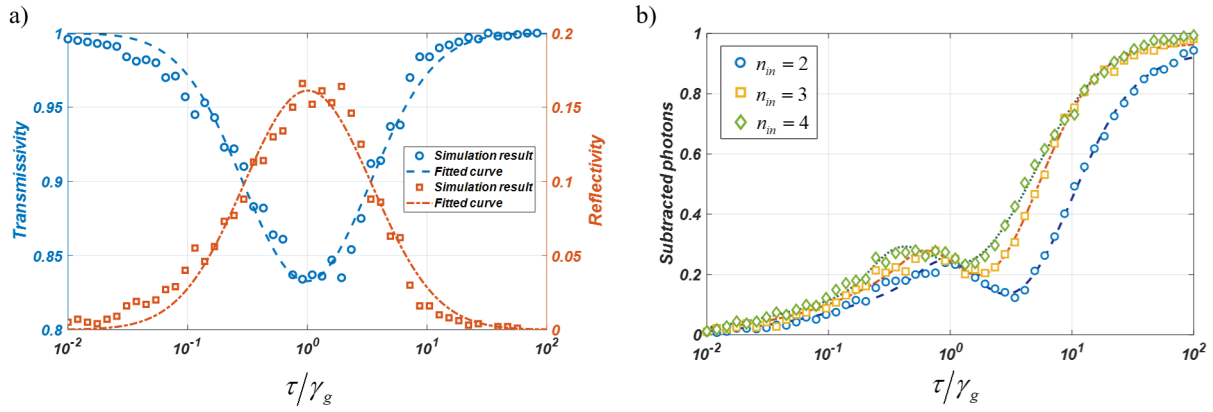


Figure 5.5: (a) Effect of pulse duration on transmissivity and reflectivity of the device for a single photon input. (b) Probability of successful photon subtraction from different multi-photon Fock states at the input.

of the distance L.

Next, we investigate how the device's performance is influenced by the duration of the input Gaussian pulse. In the above-described scenario, a single-photon Fock state pulse introduced to the right-propagating mode is expected to be directly transmitted to the output of the same mode, resulting in a transmissivity of unity. In Figure 5.5.(a), the transmissivity and reflectivity are plotted as functions of the pulse duration. For ultra-short pulses compared to the emission time ($1/\gamma_g$), the pulse does not interact with either of the atoms, and the photon is directly transmitted. Conversely, long pulses interact with both atoms sequentially, leading to two reflections and eventual transmission. However, for pulses with intermediate durations comparable to the emission time, there is a probability of 15-20% that the photon is subtracted and reflected to the left-propagating mode. This probability arises when photons, successfully reflected by the second emitter and diverted to the left-propagating mode, fail to interact with the first emitter and emerge from the left output.

In Figure 5.5.(b), we examine how the pulse duration influences the probability of successfully subtracting a single photon from multi-photon Fock state pulses. Given that the proposed design has only one emitter in state $|2\rangle$ and does not subtract more than one photon regardless of the number of input photons, this probability is also equal to the expected number of subtracted photons. As shown in this figure, the number of subtracted photons increases with the pulse duration, reaching unity for pulses as long as around one hundred times the emission time confirming the deterministic nature of the photon

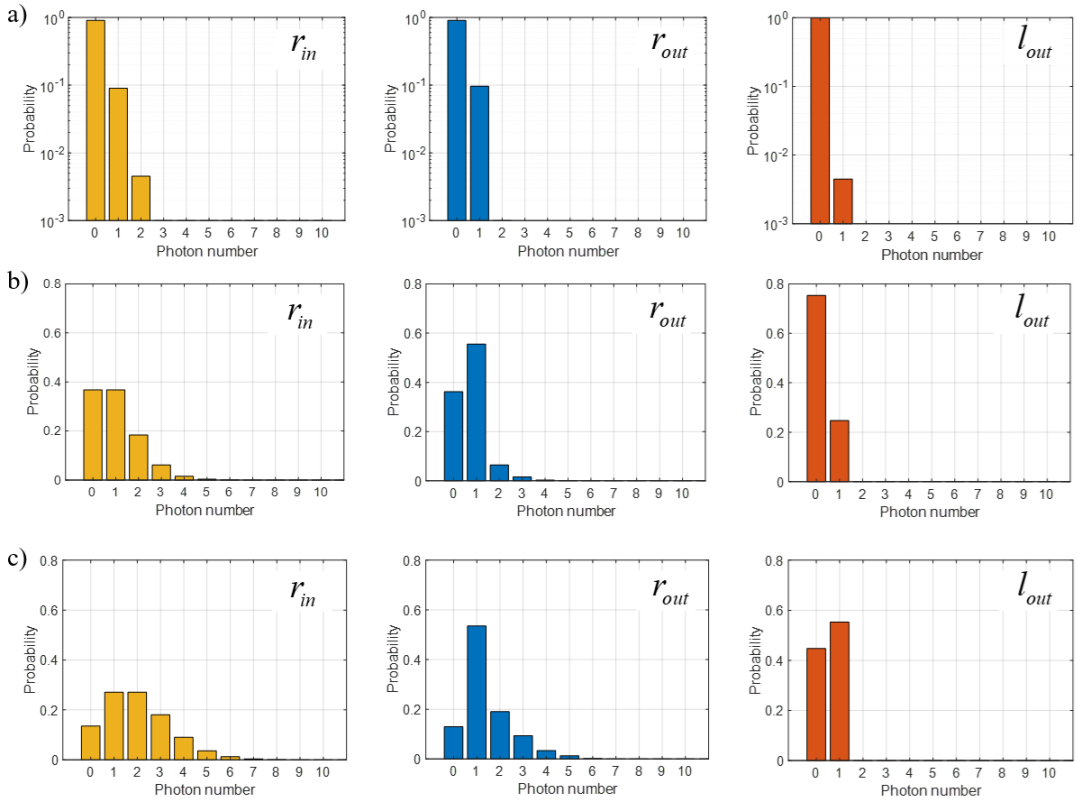


Figure 5.6: Photon subtraction from pulsed coherent state containing different mean number of photons. (a) $\bar{n}_{in} = 0.1$, (b) $\bar{n}_{in} = 1$, and (c) $\bar{n}_{in} = 2$ ($\tau = 100/\gamma_g$).

subtraction in the proposed device. Moreover, intermediate pulse durations exhibit a relative peak, similar to the one observed in the single-photon input case, which can be attributed to photons reflected by the second emitter without subsequent interaction with the first emitter.

Now, we examine the scenario where a highly attenuated coherent pulse is used as input, reflecting the conditions encountered in practical QKD applications. QKD schemes typically involve pulses with a mean number of photons around $\bar{n}_{in} = 0.1$ [32]. The photon statistics results presented in Figure 5.6 are displayed for this mean photon number as well as for two higher mean photon numbers, i.e. $\bar{n}_{in} = 1$ and $\bar{n}_{in} = 2$. Due to the small probability of non-vacuum states for $\bar{n}_{in} = 0.1$, a logarithmic scale is used for the y-axis in part (a) of this figure to represent the photon number probability distributions in this case more clearly. Comparing the photon number probability distribution at Alice's

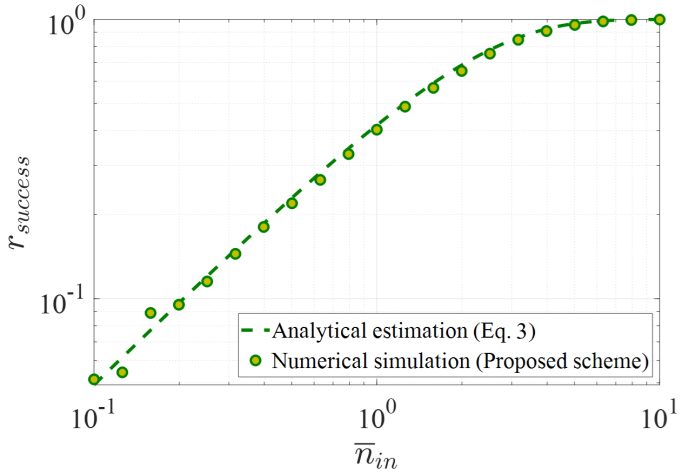


Figure 5.7: Ratio of communicated qubits successfully eavesdropped by Eve as a function of mean number of photons in the input coherent pulse ($\tau = 100/\gamma_g$).

and Bob's ends (i.e., what Alice sends versus what Bob receives shown in the first and second columns of this figure, respectively) shows an equal probability of vacuum at the corresponding network ports. This implies that no photons have been subtracted from the single-photon signals. Thus, as long as Bob utilizes a basic single-photon detector incapable of resolving the number of arriving photons, he won't be able to detect the presence of Eve. Additionally, depending on the number of photons in Alice's signal, Eve either receives one or no photon (see third column of the figure), with zero probability of receiving more than one photon, thus again confirming the deterministic behavior of the proposed subtractor. The ratio of the communicated bits successfully eavesdropped by Eve can be calculated from the following formula $r_{\text{success}} = P^{\text{Eve}}(1)/\left(1 - P^{Bob}(0)\right)$ where $P^{\text{A}}(j)$ is the probability of detecting j photons by person "A". According to the Poissonian probability distribution of the coherent state, the above expression for the case of ideal lossless photon subtractor for which $P^{\text{Eve}}(1) = 1 - P^{\text{Alice}}(0) - P^{\text{Alice}}(1)$ and $P^{\text{Bob}}(0) = P^{\text{Alice}}(0)$ can be expressed as:

$$r_{\text{success}} = 1 - \frac{P^{\text{Alice}}(1)}{1 - P^{\text{Alice}}(0)} = \frac{1 - [1 + \bar{n}_{in}]\exp(-\bar{n}_{in})}{1 - \exp(-\bar{n}_{in})} \tag{5.3}$$

Figure 5.7 shows the success probability as a function of the average number of photons contained in the coherent pulse sent by Alice $\bar{n}_{in}$. The figure includes both the success rate predicted for an ideal subtractor (equation 5.3) and the numerical simulation results for the proposed scheme. As can be seen in this figure, if Alice uses single photon coherent pulses instead of Fock states to send quantum information to Bob, photons from about

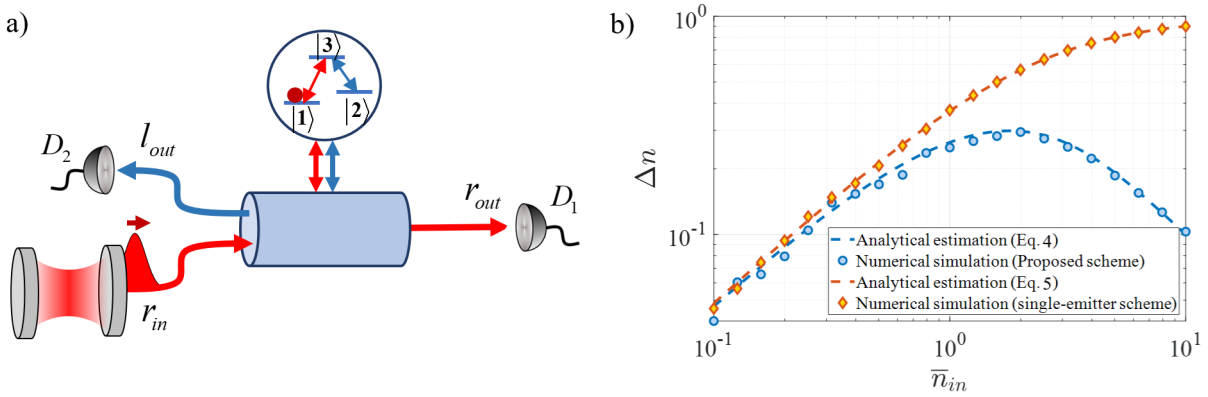


Figure 5.8: (a) Simpler scheme using a photon subtractor made of a single Λ-type emitter, and (b) relative change in average number of photons received by Bob for the two different schemes ($\tau = 100/\gamma_g$).

45% of the communicated pulses would be collected for further analysis by Eve using this photon subtractor. In practical applications, where coherent pulses with a lower number of photons (~ 0.1 photon) are utilized, Eve can block some single-photon pulses, thereby augmenting the percentage of communicated bits she can access. In such scenarios, if Eve substitutes the lossy channel used by Alice and Bob for communication with a lossless one, her attack can remain undetectable as it neither induces errors nor alters the detection rate at Bob's end [82].

To evaluate our proposed PNS scheme against a potential counter-measure, let's consider the scenario that Bob has a PNR detector and measures the average number of photons he receives at his end and by comparing it with the average photon number sent by Alice attempts to detect presence of potential eavesdroppers, as proposed in Ref. [40]. The sensitivity of this measurement depends on the efficiency of his detector. Hence, when the percentage of change in average photon number is lower than a limit, there will be a high chance that the photon subtraction process remains undetectable for Bob. The relative photon number change for an ideal lossless subtractor, is:

$$\Delta n = \frac{\bar{n}_{in} - \bar{n}_{out}}{\bar{n}_{in}} = \frac{P^{Eve}(1)}{\bar{n}_{in}} = \frac{1 - P^{\text{Alice}}(0) - P^{\text{Alice}}(1)}{\bar{n}_{in}} = \frac{1 - [1 + \bar{n}_{in}]\exp(-\bar{n}_{in})}{\bar{n}_{in}} \tag{5.4}$$

where $\bar{n}_{out}$ is the mean number of photons detected by Bob. We compare our system with a simplified implementation employing a simple single-photon subtractor, as illustrated in Figure 5.8.(a). In this configuration, the single-stage SPRINT-based subtractor extracts one photon from the input signal, directing it to Bob, who in this scheme employs detector

D_2, while routing the remaining photons to Eve, who utilizes detector D_1. For this scheme, in the ideal limit one has $\bar{n}_{out} = 1 - P^{\text{Alice}}(0)$, and therefore:

$$\Delta n = \frac{\bar{n}_{in} - \left[1 - P^{\text{Alice}}(0)\right]}{\bar{n}_{in}} = 1 - \frac{1 - \exp\left(-\bar{n}_{in}\right)}{\bar{n}_{in}} \tag{5.5}$$

Figure 5.8.(b) illustrates the outcomes derived from equations 5.4 and 5.5 together with the numerical simulation results for both schemes. The Hamiltonian and Lindblad operators employed in the simulations of the single-emitter subtractor shown in Figure 5.8.(a) are $H = H_{sys} + i/2 \times \left(\sqrt{\gamma_g} g_u \sigma_{13} a^\dagger - \text{H.c.}\right)$, $L_0(t) = \sqrt{\gamma_g}\sigma_{13} + g_u^* a$, and $L_1(t) = \sqrt{\gamma_g}\sigma_{23}$. As depicted in the figure, the proposed scheme exhibits a lower relative change in the number of photons received by Bob compared to the single-emitter approach, particularly in cases with a high mean number of photons. This implies that the communicating parties have a lower chance of detecting the eavesdropper in the case of the proposed scheme.

We recently became aware that a proposal and analysis using a single-stage SPRINT for a PNS attack was published in 2024 [4], around the same time as our paper on this topic [95]. In their study, the information gained by the eavesdropper and the resulting quantum bit error rate (QBER) are calculated. Their analysis relies on the simple single-emitter photon-extraction scheme shown in Fig. 5.8.(a) and assumes that Bob does not have access to a photon-number-resolving (PNR) detector. In contrast, as discussed above, our proposed approach is less vulnerable to PNR-based counterattacks since it induces a smaller change in the photon-number arrival rate at Bob's end.

Chapter 6

Multi-Photon Fock State Generation via a Generalized Selective Photon Subtractor

In the previous chapter, we introduced a photon subtraction scheme that leveraged the temporal entanglement generated by the SPRINT mechanism to enable a novel and useful feature. We showed that cascading two photon subtractors allows for the subtraction of a second photon after the first has been subtracted and re-added. This configuration enables selective photon subtraction from states containing more than one photon. In this chapter, we demonstrate how this concept can be extended to an n-emitter cascade, resulting in a photon subtractor capable of selectively removing photons based on their position in the arrival-time sequence of the incoming photons. Unlike the simple SPRINT-based subtractor, where the detection time of the subtracted photon serves as a lower bound for the transmitted photons, in the scheme proposed in this chapter, the subtracted photon acts as a time reference signal that can divide the input pulse into two parts. We show that this approach enables the splitting of n photons from the input light, generating a nearly single-mode n-photon Fock state.

One of the key applications of multi-photon Fock states is in quantum-optical metrology, where optical interferometers measure the phase difference between two modes of light [29]. This phase shift can reveal various physical quantities, such as displacement, temperature, gravity, and angular acceleration, and is utilized in different types of sensors across various fields of science and engineering [20, 100, 139]. The presence of quantum noise, as dictated by the Heisenberg uncertainty principle, limits the precision of interferometers [8]. When

classical light is used, the minimum achievable noise level is known as the standard quantum limit (SQL), where the uncertainty in the measured phase decreases as $1/\sqrt{N}$, with N representing the number of measurements. This precision can be enhanced if the coherent input is replaced with quantum states that possess finer structural features in their Wigner representation. This improvement is ultimately constrained by another minimum noise level, known as the Heisenberg limit (HL), where the uncertainty scales as $1/N$. It has been shown that a Mach-Zehnder interferometer (MZI) with a twin Fock state input can reach the Heisenberg limit precision with the intensity difference or parity detection schemes [52,55]. However, while various methods have been proposed in the literature for generating Fock states, the efficient generation of multi-photon Fock state pulses with high fidelity, high modal purity, and arbitrary photon numbers remains a significant challenge [75, 101, 142].

The structure of the present chapter is as follows: In section 6.1, we develop a comprehensive mathematical model for our selective photon subtractor concept including a variational approach to explore the modal structure of its output light. In section 6.2, we study the proposed cascaded QED scheme for practical implementation of the introduced concept. We adopt a quantum input-output perspective and discuss how a master equation can be extracted and solved for the resulting quantum network. Both analytical and numerical results are presented, compared, and discussed in section 6.3.

6.1 Photon Culling: Mathematical Modeling

Consider a four-port quantum optics device with one input and three output ports, as shown in Figure 6.1. We refer to this device as a selective photon subtractor or 'photon culler' because it is capable of sorting incoming photons based on their arrival times and selectively subtracting the photon arriving j-th in the sequence. The subtracted photon is routed to the purple output, while the remaining photons are distributed between the other two output ports. Photons arriving before the subtracted photon ($j-1$ photons) are sent to the red output port, while those arriving afterward are directed to the blue output port. Additionally, if the input pulse contains no more than $j-1$ photons, the entire pulse is routed to the red output. We use operators $\hat{g}^\dagger(t)$, $\hat{r}^\dagger(t)$, $\hat{p}^\dagger(t)$, and $\hat{b}^\dagger(t)$ to represent the creation of a single photon at time t in the green, red, purple, and blue modes, respectively. If a single spatiotemporal wavepacket is sent to the device as input, the state of the light in the system, prior to the interaction with the device, can be expressed in its most general

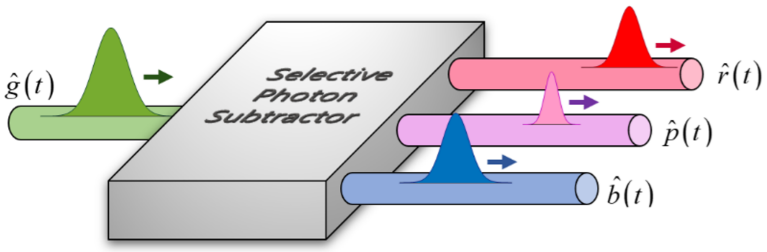


Figure 6.1: Schematic of a selective photon subtractor (photon culler), represented as a four-port quantum optics device with one input port and three output ports.

form (assuming the occupying quantum state to be pure), as follows:

$$|\psi\rangle = \sum_{n=0}^{\infty} \frac{c_n}{\sqrt{n!}} \left(\hat{g}_h^\dagger\right)^n |0\rangle \tag{6.1}$$

In the above equation, $\hat{g}_h^\dagger = \int_{-\infty}^{\infty} dt \exp\left(-i\omega t\right) h\left(t\right) \hat{g}^\dagger\left(t\right)$ represents the photon wavepacket creation operator in the green input mode, responsible for creating a photon in a wavepacket with carrier frequency ω and amplitude $h\left(t\right)$, which satisfies the normalization condition $\int_{-\infty}^{+\infty} dt |h\left(t\right)|^2 = 1$. Additionally, the coefficients c_n denote the amplitude of different Fock states in the quantum superposition.

An alternative way to describe the state of the light in the system is by numbering the photons according to their arrival times. However, since the photons in the pulse are indistinguishable, we must account for the number of permutations of the n photons. This introduces a combinatorial factor, so the expression for any n-photon state must be multiplied by the number of permutations, $n!$, leading to the following expression for $|\psi\rangle$:

$$|\psi\rangle = \sum_{n=0}^{\infty} c_n \sqrt{n!} \int_{\infty > t_n > \ldots > t_1} \left[\prod_{i=1}^{n} dt_i \exp\left(-i\omega t_i\right) h\left(t_i\right) \hat{g}^\dagger\left(t_i\right)\right] |0\rangle. \tag{6.2}$$

Here, t_1 to t_n represent the arrival times of the photons in an n-photon number state within the input pulse. Additionally, the n-fold integral used is defined as follows:

$$\int_{\alpha > t_n > \ldots > t_1} dt_n dt_{n-1} \ldots dt_1 := \int_{-\infty}^{\alpha} dt_n \int_{-\infty}^{t_n} dt_{n-1} \ldots \int_{-\infty}^{t_2} dt_1. \tag{6.3}$$

Based on the scenario described above regarding the distribution of input photons among the output ports, the quantum state of the output light, after the interaction of the

input pulse with the quantum system has been completed, can be expressed as follows:

$$\begin{aligned}|\psi\rangle = &\sum_{n=0}^{j-1} c_n\sqrt{n!}\int_{\infty>t_n>\ldots>t_1}\left[\prod_{i=1}^{n} dt_i h\left(t_i\right)\hat{r}^{\dagger}\left(t_i\right)\right]|0\rangle \\ &+c_j\sqrt{j!}\left[\int_{-\infty}^{+\infty} dt_j h\left(t_j\right)\hat{p}^{\dagger}\left(t_j\right)\int_{t_j>t_{j-1}>\ldots>t_1}\left[\prod_{i=1}^{j-1} dt_i h\left(t_i\right)\hat{r}^{\dagger}\left(t_i\right)\right]\right]|0\rangle \\ &+\sum_{n=j+1}^{\infty} c_n\sqrt{n!}\left[\int_{\infty>t_n>\ldots>t_{j+1}}\prod_{i=j+1}^{n}\left[\begin{array}{l} dt_i h\left(t_i\right)\hat{b}^{\dagger}\left(t_i\right)\times \\ \int_{-\infty}^{t_{j+1}} dt_j h\left(t_j\right)\hat{p}^{\dagger}\left(t_j\right)\int_{t_j>t_{j-1}>\ldots>t_1}\left[\prod_{i=1}^{j-1} dt_i h\left(t_i\right)\hat{r}^{\dagger}\left(t_i\right)\right]\end{array}\right]\right]|0\rangle.\end{aligned} \tag{6.4}$$

The above expression assumes that the entire quantum process occurring inside the device is fully coherent. Moreover, in this expression, we have omitted the term $\exp\left(-i\omega t_i\right)$ by moving to a frame rotating with frequency ω. Since the photon subtractor removes the j-th arriving photon, the timing of the photon propagating in the purple mode reflects the timing of photons in the red and blue modes, thereby creating temporal entanglement between different outputs. Therefore, without measuring the subtracted photon in the purple mode, the output pulses in either the red or blue ports cannot contain a pure single-mode quantum state. However, if we use a single-photon detector at the purple output to detect and time-tag the subtracted photon, the state of the red and blue outputs collapses to the following state vectors:

$$|\psi_r\rangle = \sqrt{\frac{1}{(j-1)!}}\left(\hat{r}_{h'}^{\dagger}\right)^{j-1}|0\rangle, \qquad |\psi_b\rangle = \left[\sum_{n=1}^{\infty}|c_n|^2\frac{n!\beta^{n-j}}{(n-j)!}\right]^{-1/2}\sum_{n=j}^{\infty} c_n\frac{\sqrt{n!\beta^{n-j}}}{(n-j)!}\left(\hat{b}_{h''}^{\dagger}\right)^{n-j}|0\rangle \tag{6.5}$$

In the above expression, $\beta = \int_{t_j}^{+\infty} d\tau h^2\left(\tau\right)$, where t_j is the detection time of the subtracted photon. According to this expression, $|\psi_r\rangle$ represents a single-mode $j-1$-photon Fock state pulse with wavepacket amplitude $h'_{t_j}\left(t\right)$. Additionally, if the input is a coherent pulse with amplitude α, where $c_n = \alpha^n\exp\left(-|\alpha|^2/2\right)\Big/\sqrt{n!}$ and the mean photon number $\bar{n} = \alpha^2$, it can be concluded that the blue output will also be a coherent state with a mean photon number of $\beta\bar{n}$ and wavepacket amplitude $h''_{t_j}\left(t\right)$. The amplitudes $h'_{t_j}\left(t\right)$ and $h''_{t_j}\left(t\right)$ are truncated versions of $h\left(t\right)$ as follows:

$$h'_{t_j}\left(t\right) = \frac{h\left(t\right)H(t_j - t)}{\sqrt{\int_{-\infty}^{t_j} dt h^2\left(t\right)}}, \qquad h''_{t_j}\left(t\right) = \frac{h\left(t\right)H(t - t_j)}{\sqrt{\int_{t_j}^{+\infty} dt h^2\left(t\right)}}, \tag{6.6}$$

where $H(x)$ is the Heaviside step function. Here, we assume $h\left(t\right)$ to be real without loss of generality.

While post-selecting the blue and red output states based on the detection time of the purple photon can increase the purity of the collected light, it should be noted that the probability of detecting the subtracted photon at a specific time t_j, which results in the generation of the pure states described in equation 6.5, approaches zero. Therefore, in practice, post-selection should be based on detecting the subtracted photon within a time interval instead. Suppose we post-select the outputs for which the photon is detected between $t_{\min}$ and $t_{\max}$. Projecting the density matrix onto the subspace corresponding to this measurement outcome and then tracing over the states of the light in the blue and purple outputs yields the density matrix of the light in the red output as follows:

$$\rho_r = \frac{1}{P}\sum_{n=j}^{\infty}\left[\begin{array}{l} |c_n|^2 n\,(j-1)!\left(\begin{array}{c} n-1 \\ j-1 \end{array}\right)\times \\ \int_{t_{\min}}^{t_{\max}} dt_j\left[\int_{t_j}^{+\infty} d\tau h^2(\tau)\right]^{n-j} h^2(t_j)\int_{\substack{t_j>x_{j-1}>\ldots>x_1 \\ t_j>y_{j-1}>\ldots>y_1}}\prod_{i=1}^{j-1}\prod_{k=1}^{j-1} h(x_i)\,h(y_k)\,dx_i dy_k \hat{r}^{\dagger}(x_i)\,|0\rangle\langle 0|\,\hat{r}(y_k) \end{array}\right] \tag{6.7}$$

where P is the probability of finding the j-th photon between $t_{\min}$ and $t_{\max}$:

$$P = \sum_{n=j}^{\infty}\int_{t_{\min}}^{t_{\max}} dt_j |c_n|^2 n\left(\begin{array}{c} n-1 \\ j-1 \end{array}\right)\left[\int_{t_j}^{+\infty} d\tau h^2(\tau)\right]^{n-j} h^2(t_j)\left[\int_{-\infty}^{t_j} d\tau h^2(\tau)\right]^{j-1}. \tag{6.8}$$

In several applications, including various quantum information and quantum metrology protocols, single-mode Fock states are preferred. Therefore, it is important to determine how closely the generated pulse approximates a single-mode pulse. This can be assessed by finding the maximum ratio of photons contained within a single wavepacket or mode. To achieve this, one needs to identify the mode amplitude $f_1(t)$ (with the index 1 denoting that the modes are sorted according to their mean photon number) that maximizes $\langle n_1\rangle = \mathrm{Tr}\left(\rho_r \hat{m}_1^{\dagger}\hat{m}_1\right)$, where the annihilation operator for the mode is $\hat{m}_1 = \int_{-\infty}^{\infty} dt f_1(t)\,\hat{r}(t)$. Using the density matrix provided in equation 6.7, the i-th moment of the photon number distribution can be expressed as the following functional:

$$\left\langle n_1^i\right\rangle = \frac{1}{P}\int_{t_{\min}}^{t_{\max}} dx \phi^{(i)}(L,x), \tag{6.9}$$

where:

$$\begin{aligned}\phi^{(i)}(L,x) = \sum_{n=j}^{\infty}\sum_{k=0}^{j-1}\sum_{m=0}^{j-k-1}(-1)^m |c_n|^2 k^i n\left(\begin{array}{c} n-1 \\ j-1 \end{array}\right)\left(\begin{array}{c} j-1 \\ k \end{array}\right)\left(\begin{array}{c} j-k-1 \\ m \end{array}\right) h^2(x) \\ \times\left(\int_{-\infty}^{x} d\tau h^2(\tau)\right)^{j-1}\left(\int_{x}^{+\infty} d\tau h^2(\tau)\right)^{n-j}\left(L(x)\,L^*(x)\right)^{k+m}\end{aligned} \tag{6.10}$$

$L(x)$ in the above expression denotes the projection of f_1 on h'_x:

$$L(x) = \langle f_1 \mid h'_x \rangle = \frac{\int_{-\infty}^{x} dt f^*(t) h(t)}{\sqrt{\int_{-\infty}^{x} dt h^2(t)}}. \tag{6.11}$$

Finding the normalized function f_1 that maximizes $\langle n_1 \rangle$ requires solving a constrained variational problem. To formulate this problem, we first expand f_1 over the function space spanned by the non-orthogonal set of functions h'_x with x varying between $t_{\min}$ and $t_{\max}$, as:

$$f_1(t) = \int_{t_{\min}}^{t_{\max}} dx \gamma(x) h'_x. \tag{6.12}$$

Substituting the above representation into the normalization condition $\langle f_1 \mid f_1 \rangle = 1$ yields the following constraint equation:

$$C = \int_{t_{\min}}^{t_{\max}} \int_{t_{\min}}^{t_{\max}} dx dy \gamma^*(x) \gamma(y) F(x,y) = 1, \tag{6.13}$$

where:

$$F(x,y) = \langle h'_y \mid h'_x \rangle = \sqrt{\frac{\int_{-\infty}^{\min(x,y)} d\tau h^2(\tau)}{\int_{-\infty}^{\max(x,y)} d\tau h^2(\tau)}}. \tag{6.14}$$

According to equations 6.11, 6.12, and 6.14, $L(x)$ is related to $\gamma(x)$ through $F(x,y)$ as $L(x) = \langle f_1 \mid h'_x \rangle = \int_{t_{\min}}^{t_{\max}} dy \gamma(y) F(x,y)$. By introducing the constraint from equation 6.13 through the Lagrange multiplier λ into the functional from equation 6.9, the following augmented functional is obtained for the first moment:

$$I = \frac{1}{P} \int_{t_{\min}}^{t_{\max}} dx \phi^{(1)}(L,x) + \lambda \int_{t_{\min}}^{t_{\max}} \int_{t_{\min}}^{t_{\max}} dz dy L^*(z) L(y) G(z,y), \tag{6.15}$$

where function $G(x,y)$ satisfies $\int_{t_{\min}}^{t_{\max}} dy G(x,y) F(y,x) = \delta(x)$. After setting $\delta I = 0$ and applying the calculus of variations, the following nonlinear integral equation is derived:

$$\frac{\partial \phi^{(1)}(L,x)}{\partial L} + \lambda \int_{t_{\min}}^{t_{\max}} dy L(z) G(z,y) = 0. \tag{6.16}$$

Solving the above equation gives the dominant mode shape of the output light. Once the main mode or any other higher order modes are determined, the fidelity of the quantum

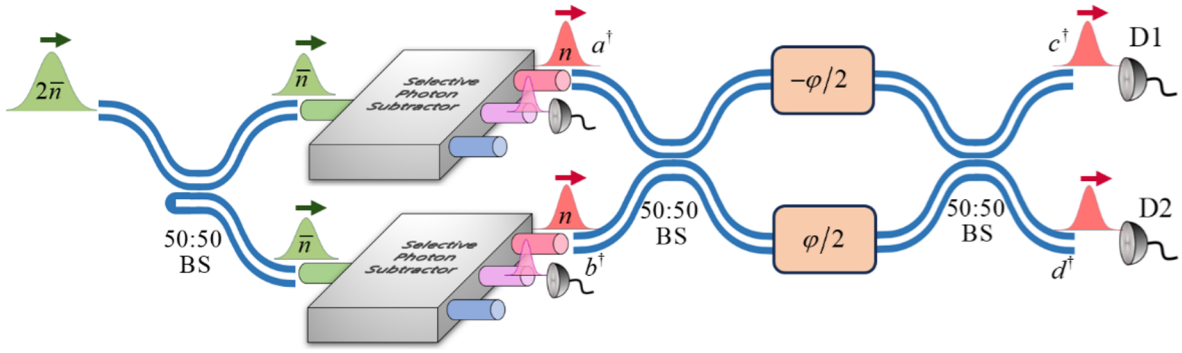


Figure 6.2: Two photon cullers integrated into a Mach-Zehnder interferometer (MZI) for phase measurement.

states occupying these modes with any desired state can be calculated. For the main mode, the fidelity with a $j-1$ photon Fock state can be obtained from the following expression:

$$\begin{aligned} F &= \langle j-1|\,\rho_m\,|j-1\rangle \\ &= \tfrac{1}{P}\int_{t_{\min}}^{t_{\max}} dx h^2(x)\left(\int_{-\infty}^{x} d\tau h^2(\tau)\right)^{j-1}\left(L(x)\,L^*(x)\right)^{j-1}\sum_{n=j}^{\infty}|c_n|^2 n\begin{pmatrix} n-1 \\ j-1\end{pmatrix}\left(\int_{x}^{+\infty} d\tau h^2(\tau)\right)^{n-j} \end{aligned} \tag{6.17}$$

As mentioned before, n-photon twin-Fock state $|n,n\rangle$ can be used for phase detection in interferometers, achieving precision at the Heisenberg limit. To evaluate the phase sensitivity of the multi-photon pulses generated by our selective photon subtractor, we consider feeding two such pulses into a Mach-Zehnder interferometer (MZI), as depicted in Figure 6.2. The photon subtractors are fed by a single coherent input pulse, which is split equally into two by a beamsplitter. The MZI consists of two 50:50 lossless beamsplitters, with phase shift elements of $\phi/2$ and $-\phi/2$ applied to different arms between the beamsplitters. The input-output relation for the interferometer can be found by multiplying the transformation matrices for the beamsplitters and the phase shift elements as follows:

$$\begin{bmatrix} c \\ d\end{bmatrix} = \left(\frac{1}{\sqrt{2}}\begin{bmatrix}1 & i\\ i & 1\end{bmatrix}\begin{bmatrix}e^{-i\phi/2} & 0\\ 0 & e^{i\phi/2}\end{bmatrix}\frac{1}{\sqrt{2}}\begin{bmatrix}1 & i\\ i & 1\end{bmatrix}\right)\begin{bmatrix} a \\ b\end{bmatrix} = \begin{bmatrix}-i\sin(\phi/2) & i\cos(\phi/2)\\ i\cos(\phi/2) & i\sin(\phi/2)\end{bmatrix}\begin{bmatrix} a \\ b\end{bmatrix}, \tag{6.18}$$

where a, b and c, d are annihilation operators of the input and output modes, respectively. If the input pulses to the MZI occupy the same temporal modes, the transformation described above can be used to calculate the output state for the input state $|n,m\rangle$ with n photons

sent to one input port and m photons to the other. The result is given by:

$$|\psi_{out}\rangle = \frac{1}{\sqrt{n!m!}} \left(\sum_{j=0}^{m} \sum_{i=0}^{n} \begin{array}{l} \sqrt{(i+j)!\,(m+n-i-j)!} \begin{pmatrix} n \\ i \end{pmatrix} \begin{pmatrix} m \\ j \end{pmatrix} \\ \times (-1)^i (\sin(\phi/2))^{m-j+i} (\cos(\phi/2))^{n-i+j} \end{array} \right) |i+j, m+n-i-j\rangle \tag{6.19}$$

However, the two input pulses of the interferometer shown in Figure 6.2 do not necessarily occupy the same temporal modes, meaning that they may correspond to different photon subtraction times in the photon subtractors. Denoting these detection times by x and y, the mode shape of the pulses would be h'_x and h'_y. Since both subtractors are fed by coherent states with the same pulse shape, the longer pulse can be expressed using a two-temporal-mode representation. For example, if $x > y$, the h'_x can be divided into two modes one with mode shape h'_y and the other one with mode shape $h'_x H(t-y) \Big/ \sqrt{\int_y^x dt h^2(t)}$. By doing so, the total input state of the interferometer would adopt a four-mode representation, with two input modes, each comprising two temporal modes as shown below:

$$|\psi_{in}\rangle = \begin{cases} \sum_{k=0}^{n} \alpha_k^{x,y} |k, n\rangle_{\text{mode1}} \otimes |n-k, 0\rangle_{\text{mode2}} & x > y \\ \sum_{k=0}^{n} \alpha_k^{x,y} |n, k\rangle_{\text{mode1}} \otimes |0, n-k\rangle_{\text{mode2}} & x < y \end{cases} . \tag{6.20}$$

The coefficients $\alpha_k^{x,y}$ satisfy $(\alpha_k^{x,y})^2 = {}_nC_k \langle h'_x \mid h'_y \rangle^{2k} \big(1 - \langle h'_x \mid h'_y \rangle^2\big)^{n-k}$ where ${}_nC_k$ represents the binomial coefficient, or the combination of k out of n. The temporal modes introduced above are orthogonal to each other and do not interfere. Hence, the result given in equation 6.19 can be used to calculate the output for each mode independently.

Here, we consider using the intensity difference measurement scheme, where the phase shift ϕ is estimated based on the difference in the number of photons counted by detectors placed at different output ports of the interferometer. When $\phi = 0$, the expected number of counts at each detector is n, leading to an expected count difference of zero due to symmetry. However, as ϕ deviates from zero, there will be an intensity difference between the outputs, which can be used to infer the phase shift and estimate its magnitude. Using this measurement scheme, the counts coming from the second mode in equation 6.20 doesn't contain any information about the phase ϕ. This is because the conditions $x > y$ and $x < y$ occur with equal probability leading to an expected count difference of zero irrespective of the phase shift. Therefore, we consider only the counts from the first mode, which means only the counts registered before either of the photon subtractors performs photon subtraction are accounted for. The probability distribution for observing a difference of

q between the detector measurements for a phase difference ϕ is given by the conditional probability, expressed as follows:

$$p^{x,y}(q|\,\phi) = \sum_{j=\max\left(\left\lceil\frac{n-q}{2}\right\rceil,-q\right)}^{\left\lfloor\frac{2n-q}{2}\right\rfloor} \left(\alpha^{x,y}_{2j+q-n}\right)^2 \frac{j!(j+q)!}{(2j+q-n)!n!} \times \left(\sum_{i=\max(0,j-n)}^{\min(j,2j+q-n)} \binom{2j+q-n}{i} \binom{n}{j-i} (-1)^i \times (\sin(\phi/2))^{n-j+2i} (\cos(\phi/2))^{3j+q-n-2i} \right)^2 \tag{6.21}$$

If the input state of the interferometer is prepared by post-selecting the subtractor outputs based on detecting both subtracted photons within the time interval between $t_{\min}$ and $t_{\max}$, the total probability $p(q|\,\phi)$ is obtained by replacing $(\alpha^{x,y}_k)^2$ by the following integral in equation 6.21, then adding the obtained $p(q|\,\phi)$ and $p(-q|\,\phi)$ to account for second half of cases where $x > y$:

$$\begin{aligned}\alpha_k^2 = \tfrac{1}{P^2} \sum_{j=n}^{\infty}\sum_{i=n}^{\infty} |c_j|^2|c_i|^2 \int_{t_{\min}}^{t_{\max}}\int_{t_{\min}}^{y} &\left[dyi \binom{i-1}{n-1} \left[\int_y^{+\infty} d\tau h^2(\tau)\right]^{i-n} h^2(y) \left[\int_{-\infty}^{y} d\tau h^2(\tau)\right]^{n-1}\right] \\ &\times \left[dxj \binom{j-1}{n-1} \left[\int_x^{+\infty} d\tau h^2(\tau)\right]^{j-n} h^2(x) \left[\int_{-\infty}^{x} d\tau h^2(\tau)\right]^{n-1}\right] \\ &\times \left[\binom{n-1}{k} \langle h'_x \mid h'_y\rangle^{2k} \left(1 - \langle h'_x \mid h'_y\rangle^2\right)^{n-1-k}\right]\end{aligned} \tag{6.22}$$

6.2 Proposed Scheme

6.2.1 Operational principle

In this section, we propose a practical scheme to implement the selective photon subtractor concept introduced and mathematically formulated in the ideal limit in the previous section. The proposed approach extends the two-emitter photon-subtraction scheme introduced in the previous chapter. Figure 3.6.(a) shows a schematic of the photon subtractor, consisting of n Λ-type three-level emitters coupled to a single chiral waveguide. All atoms are initially prepared in the ground state $|2\rangle$, except for the n-th atom (the rightmost one), which is initially in state $|1\rangle$. The input pulse is introduced into the right input mode, r_{in}. As we will explain below, when a stream of photons is sent to the right-propagating input modes of the waveguide, this system is capable of subtracting the n-th arriving photon in

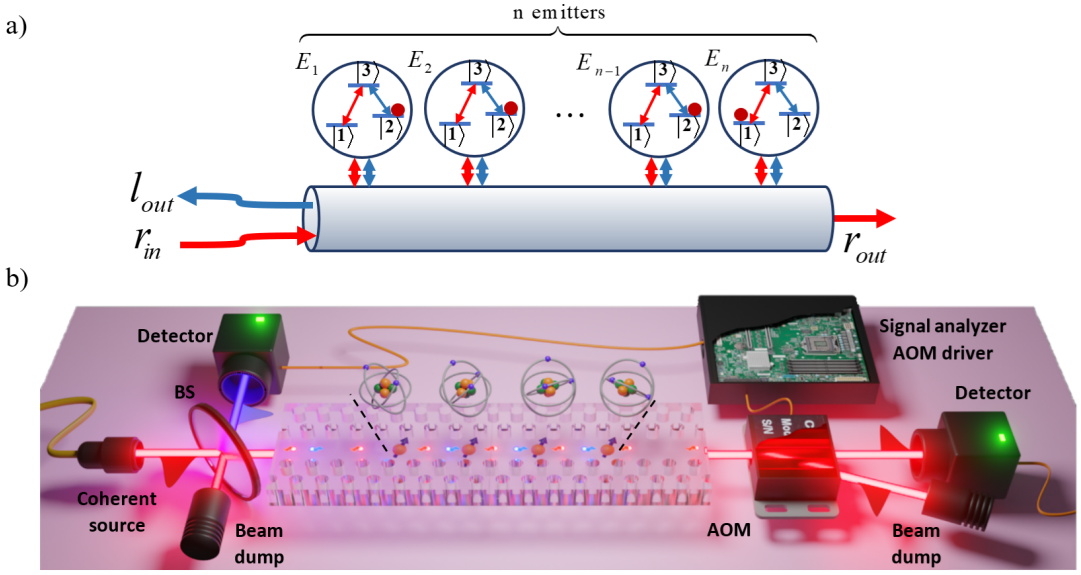


Figure 6.3: (a) The proposed scheme consisting of n three-level emitters coupled to a chiral waveguide, along with their initial states. (b) A potential realization of the scheme in part a, using a chiral photonic crystal waveguide with an acousto-optical switch at the output.

the stream, diverting it to the output of the counter-propagating mode, while allowing the other photons to be transmitted to the output port of the same initial mode.

According to the initial states of the atoms in the proposed scheme shown in the figure, the first photon introduced into the r_{in} input, after passing through the first $n-1$ atoms without interacting with them, interacts with the n-th atom, switching it to state $|1\rangle$ and getting reflected into the left-propagating mode. This photon is then reflected by the $n-1$-th atom, switches its state, and exits through the r_{out} output mode without interacting with the n-th atom a second time. After this, all atoms are in state $|2\rangle$, except the $n-1$-th atom. Consequently, the atom in state $|1\rangle$ has shifted one position to the left. This process is repeated for the next $n-2$ photons, with the atom in state $|2\rangle$ eventually shifting to the leftmost position. It then subtracts n-th photon and routes it to the l_{out} output port. After the subtraction process, all atoms are in state $|2\rangle$, and none interact with photons in the red mode, allowing subsequent photons to be transmitted.

In the scenario described, our photon subtractor divides an m-photon ($m > n$) input pulse into two temporally entangled output pulses: a single-photon pulse at the l_{out} output and an $m-1$ photon pulse at the r_{out} output mode. The temporal entanglement ensures that exactly $n-1$ photons of the latter pulse can exist in the portion of the pulse preceding

the detection of the photon in the single-photon pulse. Consequently, the subtracted photon pulse can serve as a trigger to temporally divide the r_{out} output pulse into two parts, with the first part being an $n-1$ photon pulse, regardless of the number of photons in the input pulse. This implementation is depicted in the setup shown in Figure 6.3.(b), where an acousto-optical modulator (AOM), controlled by the detection signal from a single-photon detector placed at the l_{out} output, is used to separate the $n-1$ photon pulse from the remaining photons at the r_{out} output. The setup employs a chiral photonic crystal waveguide [77], with three-level emitters coupled to it. Alternatively, nanofibers can serve as chiral waveguides [102], with emitters positioned adjacent to them and evanescently coupled to the waveguide field. Coherent laser pulses are introduced, and a high-reflectivity beam splitter at the input separates the subtracted photon, directing it to the detector.

6.2.2 Input-output formulation

In section 6.1, we demonstrated that the selective photon subtractor concept can generate highly pure, nearly single-mode Fock state pulses. Now, we need to assess whether the proposed scheme in section 6.2.1 can effectively implement the described photon culling process. To do this, we perform two different types of simulations. First, we use the dominant mode shape derived earlier to calculate the quantum state of the output light in our scheme occupying this mode. Second, we assess the performance of the proposed scheme within the measurement setup depicted in Figure 6.2. In the first part of our simulations, since the input pulse is assumed to be single-mode and our focus is on the quantum state in the primary mode of the output light, a single cavity is used at both the left input port and the output port (after the switch). The coupling of these cavities to the waveguide is described by equation 1.12, where $u(t)$ and $v(t)$ are amplitude functions of the input and output modes, respectively.

To derive the effective total Hamiltonian and Lindblad operators required in the master equation, we employ the SLH framework, described in section 1.2.2. In a frame rotating with the carrier frequencies of the input and output light, the SLH representation of the emitters, the input cavity, and the output cavity are as $\left(\mathbf{I}, \sqrt{\gamma}[\ \sigma_{13}^{(i)} \quad \sigma_{23}^{(i)}\ ]^{\mathrm{T}}, \Delta_1\sigma_{11}^{(i)} + \Delta_2\sigma_{22}^{(i)}\right)$, $\left(\mathbf{I}, g_u^*[\ a_u \quad 0\ ]^{\mathrm{T}}, 0\right)$, and $\left(\mathbf{I}, g_v^*[\ a_v \quad 0\ ]^{\mathrm{T}}, 0\right)$, respectively. In these expressions, a_u and a_v are photon annihilation operators of the input and output cavities and $\sigma_{mn}^{(i)} = |m\rangle_{(i)}\langle n|_{(i)}$ is the transition operator of the i-th emitter. Moreover, γ, Δ_1, and Δ_2 are photon emission rate of the atoms to the waveguide modes and detuning of the atomic transition with respect to the input and output light frequencies, respectively. This leads to the following

effective Hamiltonian:

$$H_{eff} = \left[\sum_{i=1}^{n} H^{(i)}\right] + \frac{1}{2i}\left[\left[\begin{array}{l} g_u^* g_v a_v^\dagger a_u + \left[\sqrt{\gamma} g_v \sum_{i=1}^{n} a_v^\dagger \sigma_{13}^{(i)}\right] + \left[\sqrt{\gamma} g_u^* \sum_{j=1}^{n} \sigma_{31}^{(j)} a_u\right] \\ + \left[\gamma \sum_{j=2}^{n} \left(\sigma_{31}^{(j)} \sum_{i=1}^{j-1} \sigma_{13}^{(i)} + \sigma_{32}^{(j)} \sum_{i=n_e}^{j+1} \sigma_{23}^{(i)}\right)\right] \end{array}\right] - \text{H.c.}\right] \tag{6.23}$$

where H.c. stands for Hermitian conjugate terms. The Lindblad operators of the network responsible for the system collapse when an output photon falls outside the dominant mode (L_0) or the subtracted photon is detected by the detector (L_1) are:

$$L_0 = g_u^* a_u + g_v^* a_v + \sqrt{\gamma} \sum_{i=1}^{n} \sigma_{13}^{(i)}, \qquad L_1 = \sqrt{\gamma} \sum_{i=1}^{n} \sigma_{23}^{(i)}. \tag{6.24}$$

It should be noted that the model provided above assumes that each component operates as a Markovian system, which holds in the weak coupling regime [16,121]. Additionally, the propagation delay between the atoms is assumed to be much smaller than the response time of the atoms. While finite propagation delays in quantum networks can introduce non-Markovian effects, in the limit where these delays vanish, they can be modeled as phase lags and the system's dynamics can be approximated as evolution under a Markovian Hamiltonian as demonstrated by Gough and James [45]. Since these phase lags do not affect the photon statistics at the output of the cascade, as discussed in the previous chapter, they have been set to zero in this analysis.

In the second part of our analysis, we simulate the quantum-optical phase measurement scheme outlined in the previous section, utilizing the photon subtractor implementation proposed here. Following the approach described above, we treat the measurement setup depicted in Figure 6.2 as a quantum network with a vacuum input by introducing a virtual cavity with a coherent state at the input of the leftmost beamsplitter. The SLH triple for a lossless beamsplitter is $G_1 = \left(\mathbf{U}, \begin{bmatrix} 0 & 0 \end{bmatrix}^T, 0\right)$ where $\mathbf{U}$ is the unitary input-output transformation matrix, as given in equation 6.18 for a 50:50 beamsplitter. Combining the SLH representations of the components yields the following Hamiltonian, which can be

used to analyze the network dynamics by solving the governing master equation:

$$H_{eff} = \left[\sum_{i=1}^{n} H^{(1,i)} + H^{(2,i)}\right] + \frac{1}{2i}\left[\begin{array}{l} \sqrt{\frac{\gamma}{2}} g_u^* \left[\sum_{j=1}^{n} \sigma_{31}^{(1,j)} + i \sum_{j=1}^{n} \sigma_{31}^{(2,j)}\right] a_u \\ +\gamma \left[\begin{array}{l} \sum_{j=2}^{n} \left(\sigma_{31}^{(1,j)} \sum_{i=1}^{j-1} \sigma_{13}^{(1,i)} + \sigma_{31}^{(2,j)} \sum_{i=1}^{j-1} \sigma_{13}^{(2,i)}\right) \\ + \sum_{j=1}^{n-1} \left(\sigma_{32}^{(1,j)} \sum_{i=n}^{j+1} \sigma_{23}^{(1,i)} + \sigma_{32}^{(2,j)} \sum_{i=n}^{j+1} \sigma_{23}^{(2,i)}\right) \end{array}\right] - \text{H.c.} \end{array}\right] \tag{6.25}$$

Additionally, the Lindblad operators L_{D1} and L_{D2}, described below, represent photon detection in detectors D1 and D2, respectively, at the output of the interferometer:

$$\begin{aligned} L_{D1} &= -\sqrt{\gamma} \sum_{i=1}^{n} \sigma_{13}^{(1,i)} \sin(\phi/2) + \sqrt{\gamma} \sum_{i=1}^{n} \sigma_{13}^{(2,i)} \cos(\phi/2) + i\frac{\sqrt{2}}{2} g_u^* a_u e^{i\phi/2} \\ L_{D2} &= \sqrt{\gamma} \sum_{i=1}^{n} \sigma_{13}^{(1,i)} \cos(\phi/2) + \sqrt{\gamma} \sum_{i=1}^{n} \sigma_{13}^{(2,i)} \sin(\phi/2) + \frac{\sqrt{2}}{2} g_u^* a_u e^{i\phi/2} \end{aligned} . \tag{6.26}$$

The first index number in the superscript of the Hamiltonian and atomic transition operators indicates the photon subtractor to which they belong. The subtractor at the top input of the interferometer is indexed by 1, while the bottom subtractor is indexed by 2.

6.3 Simulation Results and Discussion

In this section, first we use the analytical model developed in Section 6.1 for the selective photon subtractor, introduced earlier, to evaluate its performance in generating multi-photon Fock states with varying photon numbers. As discussed, the temporal entanglement created during the deterministic photon subtraction process causes the output photons from the photon culler to occupy multiple temporal modes. Post-selection of the generated pulses, based on the detection time of the subtracted photon, can enhance the modal purity at the device's output. While this improves purity, it comes at the cost of reducing the generation rate of Fock states. However, since the device can work with coherent pulses at the input and such pulses can be generated at a high rate, it is still possible to efficiently produce highly pure Fock states. To determine the set of temporal modes that contain the majority of photons, we solve the optimization problem described by equation 6.16. This equation can be discretized and solved using an iterative method. To do so, first an initial solution $L_0(x)$ is guessed (for example, a reasonable choice could be the corresponding

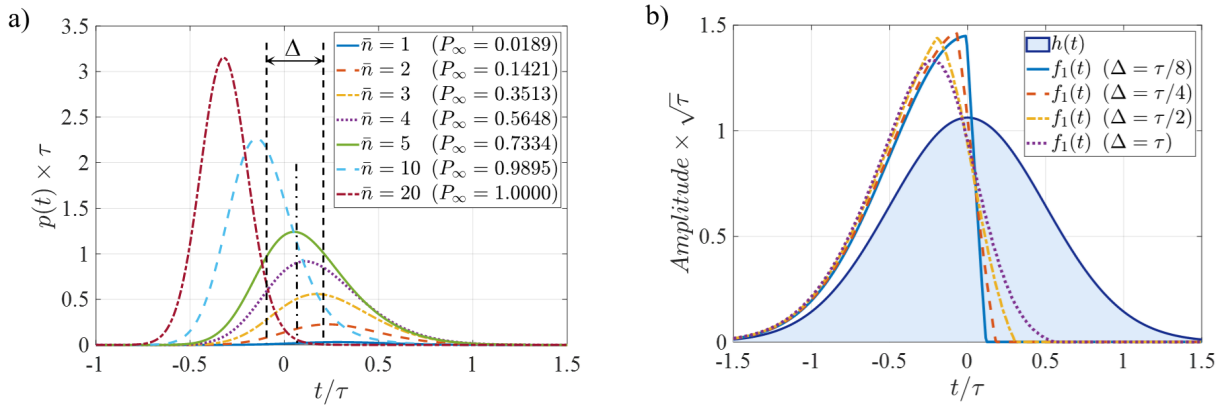


Figure 6.4: (a) Pulse shape of the subtracted photon in a selective photon subtractor subtracting the 4^{th} arriving photon, for Gaussian coherent inputs with different mean photon numbers $\bar{n}$. (b) Dominant mode shape of the output 3-photon pulse for different values of the time interval width Δ ($\bar{n} = 5$).

$L(x)$ for $f_1 = h'_{(t_{\min}+t_{\max})/2}$). Next, using equation 6.10, $\phi^{(1)}(L, x)$ is computed, and by substituting it into equation 6.16 and solving the resulting linear equation, a new function $L_1(x)$ is obtained. In this step, λ is used to adjust $L_1(x)$ and ensure that the constraint in equation 6.13 is satisfied. This process is repeated until convergence is achieved. Finally, f_1 is calculated using $\gamma(x) = \int_{t_{\min}}^{t_{\max}} dy L(y) G(x, y)$ and equation 6.12. The same method can be applied sequentially to find higher-order modes of the output light. The only difference is that when determining the n-th mode, additional constraints beyond the one in equation 6.13 must be introduced. These additional constraints ensure that the calculated mode is orthogonal to the previous $n-1$ modes.

The modal purity obtained from solving the above optimization problem clearly depends on the width of the time interval $[t_{\min}, t_{\max}]$ used for the post-selection process. A wider interval results in a higher pulse generation rate, while narrower intervals enhance purity. To achieve highly pure output pulses at a reasonable rate, we select the interval to be centered around the peak of the subtracted photon's pulse shape. This pulse shape corresponds to the probability distribution of the subtracted photon's detection time, as given by the integrand in equation 6.8.

Figure 6.4.(a) depicts the probability distribution corresponding to a device subtracting the fourth arriving photon (used to generate a 3-photon Fock state output) for input coherent pulses with varying mean photon numbers $\bar{n}$. For this result, as well as all other simulations in this section, we consider an input with a Gaussian amplitude of width τ,

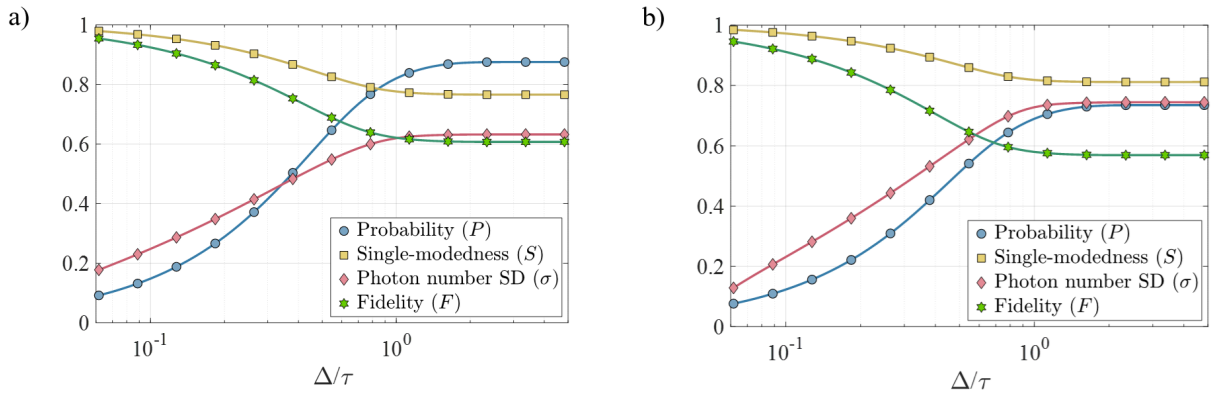


Figure 6.5: Probability of successful Fock state generation (P), Single-modedness of the generated pulse (S), Photon number standard deviation of the first mode (σ), and Fidelity of the quantum state contained in the first mode with an n-photon Fock state (F) for (a) 2-photon Fock state, and (b) 3-photon Fock state.

described by the amplitude function $h(t) = \sqrt{2/(\tau\sqrt{\pi})}\exp(-2t^2/\tau^2)$. The probability P_∞ indicated in the figure legend represents the likelihood that one photon is subtracted. For an ideal deterministic photon subtractor, this equals the probability that the input pulse contains at least four photons. In Figure 6.4.(b), the calculated dominant mode shape containing the maximum number of photons is shown for different values of the time interval width Δ.

In Figure 6.5, the impact of the post-selection parameter Δ on the characteristics of the generated multi-photon state by a selective photon subtractor is illustrated. Parts (a) and (b) of the figure examine the generation of $n = 2$ and $n = 3$ photon Fock states, respectively, from a coherent input containing $\bar{n} = 5$ photons. The first parameter studied is the probability P, representing the likelihood that a single photon is successfully subtracted and falls within the acceptable time interval $[t_{\min}, t_{\max}]$. The modal purity of the output light is represented by the parameter $S = \langle n_1\rangle/n$, which quantifies the fraction of the output photon population contained in a single mode, indicating the level of single-modedness of the output light. Photon number standard deviation $\sigma = \sqrt{\langle n_1^2\rangle - \langle n_1\rangle^2}$ is used to measure the consistency in the calculated average single-modedness S. Finally, F represents the fidelity of the quantum state in the dominant output mode compared to an ideal n-photon Fock state. As expected, increasing Δ leads to an enhancement in the probability P, which saturates at a maximum level corresponding to the likelihood that the input coherent state contains at least n photons. This increase in probability, however, is accompanied by a degradation in the other three parameters—modal purity S, photon number standard

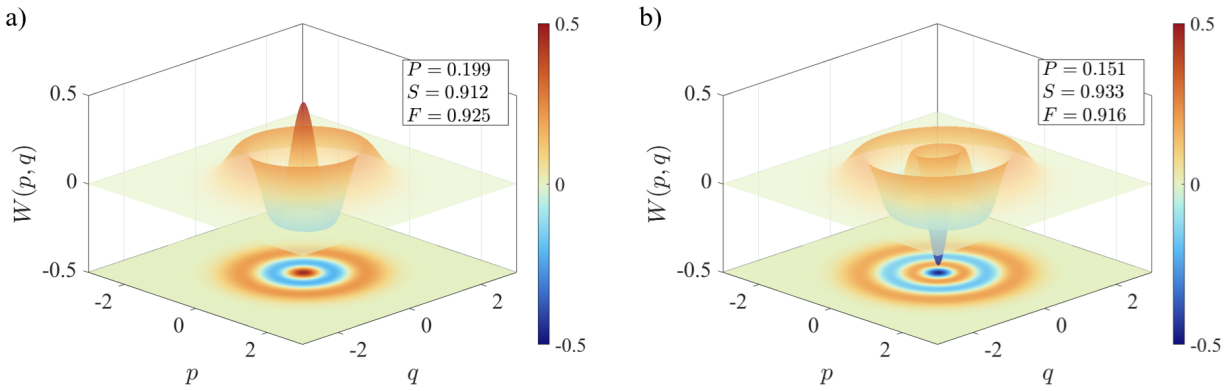


Figure 6.6: Wigner functions of the generated (a) 2-photon, and (b) 3-photon Fock states using the cascaded QED scheme shown in Figure 6.3. The generation probability (P), single-mode purity (S), and fidelity (F) of the produced states are indicated in the plot ($\bar{n} = 5$, $\Delta = \tau/8$, $\gamma\tau = 10^3$)

deviation σ, and fidelity F—as Δ becomes larger. Nevertheless, the results suggest that as long as the photon subtractor is supplied with a high rate of coherent pulses, it is possible to generate Fock states at a high rate, with fidelity and modal purity approaching unity, by selecting small values of Δ.

After demonstrating the capability of the photon culling approach in successfully generating Fock states, we now investigate the performance of our proposed scheme. Using the modal structure obtained by solving equation 6.16, we simulate the quantum network described by equations 6.23 and 6.24 to extract the exact quantum state within the dominant output mode of the cascaded QED system. This is achieved by using the stochastic quantum trajectory method, implemented with the QuTiP package in Python, to evolve the network in time by solving its governing master equation. The results are presented in Figure 6.6, where the Wigner functions of the generated 2- and 3-photon Fock states are plotted. The calculated fidelities exceed 90% for $\Delta = \tau/8$ and can be further improved, approaching unity, by reducing Δ.

To evaluate how the multi-photon pulses generated by the photon culling process outperform classical light in quantum metrology, we consider a quantum-optical interferometry-based phase measurement scheme, as illustrated in Figure 6.2. As mentioned before, the goal is to estimate the phase ϕ by measuring the difference q in photon counts registered by detectors D1 and D2, positioned at different outputs of the interferometer. Using the probability distribution from equation 6.21, the Fisher information can be calculated as a measure of the average information that can be inferred about the phase ϕ from a single

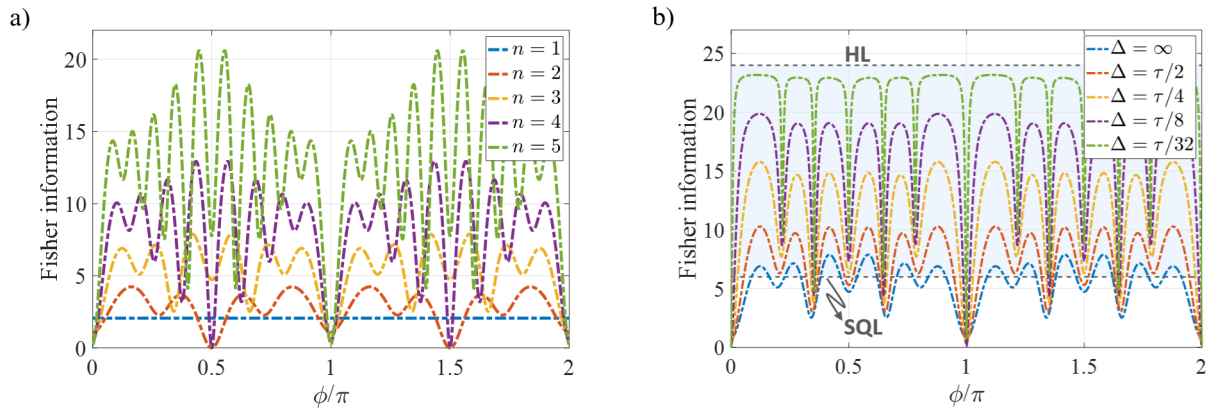


Figure 6.7: Effect of (a) photon number n, and (b) post-selection interval Δ, on the Fisher information content of the output light of the interferometer for 3-photon input pulses generated via selective photon subtraction.

measurement. This is given by the following summation over all possible outcomes q:

$$F(\varphi) = \sum_{q=-2n}^{2n} \frac{1}{p(q|\varphi)} \left(\frac{\partial p(q|\varphi)}{\partial \varphi} \right)^2. \tag{6.27}$$

The significance of Fisher information lies in the fact that, according to the Cramer-Rao bound, the precision of an unbiased estimator in a measurement is fundamentally limited to $1/F(\varphi)$ [150]. This sets the lower bound on the variance of any estimator, meaning that higher Fisher information leads to more precise estimates. In classical interferometry with coherent light, the Fisher information equals the total number of photons used at the input of the interferometer [8]. However, it can be shown that when coherent light is replaced by n-photon Fock states, the Fisher information increases to $2n(1+n)$ which scales with the square of n, consistent with the Heisenberg limit [101].

Figure 6.7.(a) illustrates the Fisher information for generated multiphoton states with varying photon numbers when no post-selection is applied to the output ($\Delta \to \infty$). As observed, for photon numbers greater than 1, the Fisher information becomes dependent on ϕ, exceeding the classical limit in certain regions of the ϕ domain. Notably, as n increases, the peaks of the curves rise beyond linear behavior, indicating that the Fisher information moves further away from the classical limit and approaches the Heisenberg limit. In Figure 6.7.(b), we observe the enhancement of Fisher information through post-selection. The results are presented for a 3-photon pulse, demonstrating that if the selected width Δ for

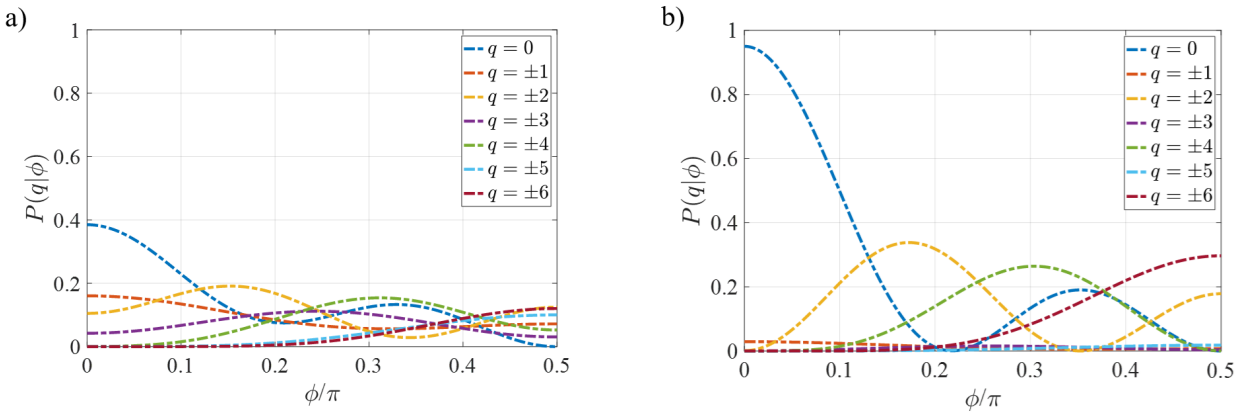


Figure 6.8: Conditional probability $P(q|\phi)$ vs. phase shift ϕ for 3-photon Fock state inputs when (a) No post-selection applied ($\Delta \to \infty$), and (b) post selection applied with $\Delta = \tau/32$.

the post-selection interval is sufficiently small, it is possible to approach the Heisenberg limit for pure Fock states of the same photon number. The dips in the curve are attributed to the high probability of measuring odd q values, which convey less information at specific phases. It is important to note that for pure Fock state inputs, only even q values can occur.

In Figure 6.8, the conditional probability $P(q|\phi)$ is plotted for different values of q. In part (a), where no post-selection is applied, the curves exhibit broader peaks and lower sensitivity to changes in ϕ. However, after applying post-selection with a relatively small Δ, the curves for odd values of q disappear, leaving sharper peaks for the remaining curves. In the specific case of single-photon inputs, the only possible measurement with an odd q is $q = \pm1$, which occurs when there is only one photon at the common mode of the two inputs. This single photon will be detected at one of the detectors regardless of the phase ϕ. Consequently, the Fisher information curve for this specific case is independent of ϕ, as observed in Figure 6.7.(a).

Figure 6.9 shows the precision of a single measurement of the phase as a function of the number of photons in the multi-photon states used. As observed, when no post-selection is applied, measurements with low-photon-number Fock states can yield precisions higher than the classical limit achieved with coherent inputs. However, as the photon number increases, the situation improves, and the precision surpasses the classical limit across all values of ϕ. When post-selected input states from the photon culler are used as input to the interferometer, the precision is significantly enhanced, closely following the Heisenberg

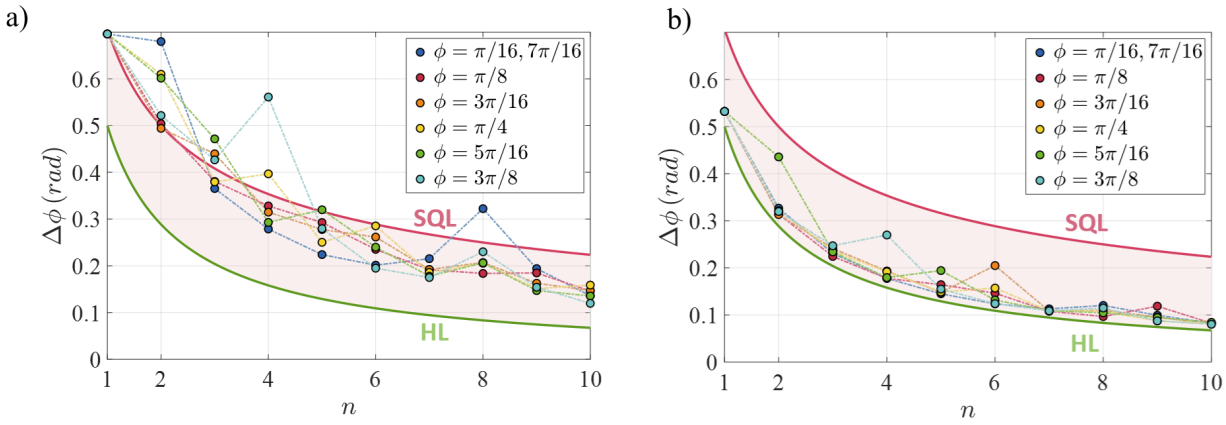


Figure 6.9: Phase measurement precision against the number of photons in multi-photon state inputs to the interferometer. (a) No post-selection applied ($\Delta \to \infty$), and (b) post-selection applied with $\Delta = \tau/8$.

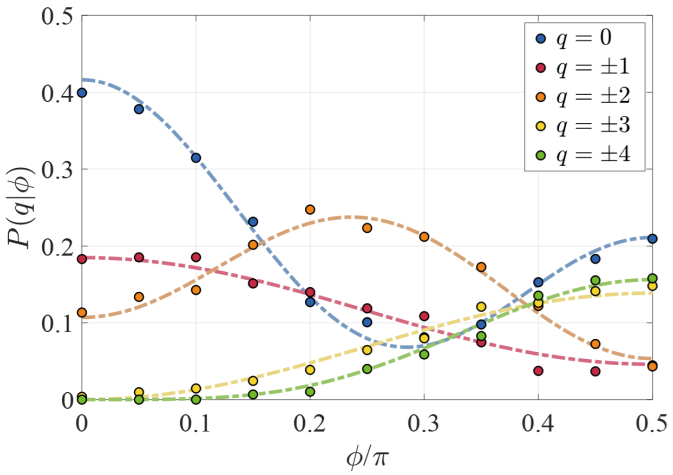


Figure 6.10: Conditional probability $P\,(q|\,\phi)$ vs. phase shift ϕ for 2-photon Fock state inputs and no post-selection ($\Delta \to \infty$). Dotted lines are analytical results for the ideal photon culler, circle markers are Monte-Carlo simulation results for the proposed emitter cascade scheme.

limit curve, particularly at higher photon numbers. Overall, as demonstrated by these results, the Fock states generated through the selective photon subtractor concept can be efficiently applied to quantum phase estimation. The next step is to determine whether the

proposed cascaded scheme can achieve the same results. To do this, we use the quantum network model developed in the previous section, as formulated in equations 6.25 and 6.26. We apply the quantum trajectory method to solve the governing master equation and analyze the statistics of the detector clicks registered at the output of the MZI. The results, shown in Figure 6.10, illustrate the conditional probability distribution for twin 2-photon Fock states generated by two 3-emitter cascades. As observed, the results align with the analytical predictions, indicating that the desired measurement precision can be realized using the proposed multi-emitter scheme.

Chapter 7

Conclusions

This thesis explored how the manipulation of light pulses at the single-photon level can unlock a wide range of possibilities, with applications across various areas of quantum information technology. Photon subtraction was employed as the primary tool to achieve this goal. Among the various photon subtraction techniques currently available and experimentally demonstrated, we focused on the one based on the single-photon Raman interaction (SPRINT). This approach not only enables deterministic photon subtraction due to its self-terminating nature, but also allows the subtracted photon to be routed to a distinct optical mode. This capability opens up additional opportunities for applications that rely on either measurements performed on the subtracted photon or its use as a trigger for a secondary process. We explored and discussed the feasibility of experimentally implementing the proposed schemes based on the current state of the art, and the parameters used in the simulations were chosen to reflect values that are technologically achievable according to the literature.

To evaluate the performance of the SPRINT mechanism for deterministic single-photon subtraction, we began with a comprehensive analysis of single-photon transport in bimodal waveguide-cavity systems coupled to three-level Λ-type quantum emitters. Combining analytical techniques based on the input-output formalism with numerical simulations using the Monte Carlo wave function (MCWF) method, we investigated the influence of various parameters including input pulse shape, duration, carrier frequency, and quantum state content, as well as atom-cavity coupling strength, cavity decay rate, and atomic lifetime on the device's behavior. Our findings highlight the potential of utilizing insights from single-photon transport analysis to guide the design of efficient photon subtractors capable of extracting photons from input pulses with varying photon counts, achieving success probabilities approaching unity. We evaluated the success rate of our photon

subtractor within current QED systems involving multiple cavity modes interacting with a single quantum emitter, demonstrating that success rates approaching unity are achievable, particularly with cold atoms trapped in crossed optical fiber cavities.

Motivated by recent advances in the fabrication of highly chiral nanophotonic waveguides and the successful direct coupling of solid-state quantum emitters to them, we next analyzed the photon subtractor in a configuration where the incoming light and the subtracted photon propagate in counterpropagating modes of a chiral waveguide. We demonstrated that deterministic photon subtraction in this scheme can effectively transform squeezed and coherent states of light into non-Gaussian states. We employed an input-output formalism with squeezed vacuum, coherent, and Fock state input pulses to calculate the temporal modes of the output light through eigen decomposition of first-order autocorrelation matrices. Subsequently, we determined the quantum state content of different modes by cascading virtual cavities at various outputs of the subtractor and evolving the obtained quantum network in time using quantum trajectory method. Our results revealed that the proposed method not only can achieve higher success probabilities for generating kitten states from squeezed vacuum compared to traditional beam-splitter-based methods but also has the capability to generate non-Gaussian states, including kitten states, directly from coherent laser pulses. The calculated fidelities are above 99% for both cases of squeezed vacuum and coherent states.

In the next step, we explored cascading single-photon subtractors in one-way and two-way configurations, aiming to achieve multi-photon subtraction and selective photon subtraction, respectively. For the one-way cascade, we proposed and thoroughly investigated a photon-number-resolving (PNR) detector based on a series of Λ-type emitters coupled to a chiral waveguide. In this potential application of SPRINT-based deterministic photon subtraction, the cascade of waveguide-coupled Λ-type atoms enables deterministic demultiplexing of input photons across multiple single-photon detectors. Based on a photon transport analysis in the time domain, we calculated the success rate of photon subtraction for input pulses with varying photon numbers, considering single-mode pulses, as well as both fully or partially overlapping multi-mode pulses. We further evaluated the total number of photons subtracted by the cascade and determined the achievable resolution precision as a function of the number of emitters and their coupling strength to the waveguide. Our results showed that the proposed detector, with technologically feasible coupling rates, can outperform conventional spatial demultiplexing PNR schemes using the same number of single-photon detectors.

Subsequently, we turned to two-way cascades over chiral waveguides and, by leveraging the temporal entanglement of the output photons in a deterministic photon subtractor, demonstrated the possibility of selective photon subtraction. The selectivity arises from

the photon subtractor's ability to choose which photon to subtract based on its position in the time arrival sequence, a capability we referred to as photon culling. For the specific case of two-emitter cascade, our results demonstrated the proposed scheme's ability to deterministically extract single photons from pulses with more than one photon while allowing the transmission of pulses with only one photon. Our findings suggest tantalizing potential for successful photon-number-splitting (PNS) attacks on quantum key distribution (QKD) schemes implemented with weak coherent pulses and motivate future efforts to implement this scheme experimentally. By extending the two-emitter scheme to a multi-emitter configuration, we demonstrated that this specialized photon subtractor can be used to directly generate multi-photon Fock states with high fidelity and modal purity from a coherent input. An input-output analysis of this system revealed that the generated multi-photon states could significantly enhance phase measurement precision in quantum-optical interferometry—a potential application of this technique. This enhancement can be further improved, approaching the Heisenberg limit, by post-selecting the generated states based on the detection time of the subtracted photon. Since the process is based on coherent laser pulses, high-rate Fock state generation remains feasible, even with stringent post-selection conditions.

7.1 Future Directions and Outlook

The range of possible applications explored in this thesis for deterministic photon subtraction arises from two main mechanisms by which this operation manipulates light: altering the photon number distribution and generating temporal entanglement between the output photons. We demonstrated how the combination of these two mechanisms enables the direct generation of non-Gaussian states of light, including Schrödinger's kitten states and multi-photon Fock states, from an input Gaussian state. Moreover, in contrast to traditional photon subtraction schemes, which are inherently probabilistic and suffer from low success rates that limit their effectiveness for multi-photon subtraction, the deterministic approach investigated in this thesis supports high-fidelity number-resolved multi-photon subtraction. These capabilities pave the way for photon subtraction schemes that could significantly expand the range of accessible nonclassical states and enhance their generation rates.

Regarding the PNR detection capability, one can further explore how this approach compares to conventional demultiplexing-based PNR detection as the number of detectors increases beyond the few-photon case studies presented here, particularly for the detection of more complex nonclassical states. Notably, our PNR detector exhibits several

unique features, such as the emergence of correlations in the nonlinear regime and the generation of intermittent entanglement between photons during the detection process. These features are absent in conventional demultiplexing schemes and open new avenues for both foundational research and practical applications. Beyond high-precision multi-photon detection, this PNR scheme may also enable novel forms of quantum tomography and the generation of exotic photon states by combining its photon-number-resolving and entanglement-generating capabilities.

Implementing the photon subtraction mechanism described in this thesis using a solid-state platform instead of cold atoms can offer several advantages, including the capability of on-chip integration with electronics, increased scalability, and potential for miniaturization. Solid-state emitters exhibiting Λ-type transitions can be found among point defects in wide-bandgap semiconductors, such as diamond [137] and silicon carbide [128], as well as in quantum dots [31]. Among the different potential candidates, the combination of large optical oscillator strength and long coherence time [6, 49, 117], makes NV and SiV centers in diamond particularly well-suited for this application.

References

[1] Ulrik L Andersen, Tobias Gehring, Christoph Marquardt, and Gerd Leuchs. 30 years of squeezed light generation. *Physica Scripta*, 91(5):053001, 2016.

[2] Vahid Ansari, John M Donohue, Markus Allgaier, Linda Sansoni, Benjamin Brecht, Jonathan Roslund, Nicolas Treps, Georg Harder, and Christine Silberhorn. Tomography and purification of the temporal-mode structure of quantum light. *Physical review letters*, 120(21):213601, 2018.

[3] Marta Arcari, Immo Söllner, Alisa Javadi, S Lindskov Hansen, Sahand Mahmoodian, Jin Liu, Henri Thyrrestrup, Eun Hye Lee, Jin Dong Song, and Søren Stobbe. Near-unity coupling efficiency of a quantum emitter to a photonic crystal waveguide. *Physical review letters*, 113(9):093603, 2014.

[4] Ariel Ashkenazy, Yuval Idan, Dor Korn, Dror Fixler, Barak Dayan, and Eliahu Cohen. Photon number splitting attack–proposal and analysis of an experimental scheme. *Advanced Quantum Technologies*, 7(7):2300437, 2024.

[5] Michal Bajcsy and Arka Majumdar. Arithmetic with photons. *Nature Photonics*, 10(1):4–6, 2016.

[6] Gopalakrishnan Balasubramanian, Philipp Neumann, Daniel Twitchen, Matthew Markham, Roman Kolesov, Norikazu Mizuochi, Junichi Isoya, Jocelyn Achard, Johannes Beck, and Julia Tissler. Ultralong spin coherence time in isotopically engineered diamond. *Nature materials*, 8(5):383–387, 2009.

[7] Ben Q. Baragiola, Robert L. Cook, Agata M. Brańczyk, and Joshua Combes. n-photon wave packets interacting with an arbitrary quantum system. *Physical Review A*, 86(1):013811, 2012. PRA.

[8] Marco Barbieri. Optical quantum metrology. *PRX Quantum*, 3(1):010202, 2022.

[9] Stephen M Barnett, Gergely Ferenczi, Claire R Gilson, and Fiona C Speirits. Statistics of photon-subtracted and photon-added states. *Physical Review A*, 98(1):013809, 2018.

[10] Erwan Bimbard, Nitin Jain, Andrew MacRae, and AI Lvovsky. Quantum-optical state engineering up to the two-photon level. *Nature Photonics*, 4(4):243–247, 2010.

[11] Gilles Brassard, Norbert Lütkenhaus, Tal Mor, and Barry C Sanders. Limitations on practical quantum cryptography. *Physical review letters*, 85(6):1330, 2000.

[12] Samuel L Braunstein and Peter Van Loock. Quantum information with continuous variables. *Reviews of modern physics*, 77(2):513, 2005.

[13] Benjamin Brecht, Andreas Eckstein, Raimund Ricken, Viktor Quiring, Hubertus Suche, Linda Sansoni, and Christine Silberhorn. Demonstration of coherent time-frequency schmidt mode selection using dispersion-engineered frequency conversion. *Physical Review A*, 90(3):030302, 2014.

[14] Benjamin Brecht, Dileep V Reddy, Christine Silberhorn, and Michael G Raymer. Photon temporal modes: a complete framework for quantum information science. *Physical Review X*, 5(4):041017, 2015.

[15] Manuel Brekenfeld, Dominik Niemietz, Joseph Dale Christesen, and Gerhard Rempe. A quantum network node with crossed optical fibre cavities. *Nature Physics*, 16(6):647–651, 2020.

[16] Heinz-Peter Breuer, Elsi-Mari Laine, Jyrki Piilo, and Bassano Vacchini. Colloquium: Non-markovian dynamics in open quantum systems. *Reviews of Modern Physics*, 88(2):021002, 2016. RMP.

[17] Heinz-Peter Breuer and Francesco Petruccione. *The theory of open quantum systems*. Oxford University Press, USA, 2002.

[18] Claudio Bruschini, Harald Homulle, Ivan Michel Antolovic, Samuel Burri, and Edoardo Charbon. Single-photon avalanche diode imagers in biophotonics: review and outlook. *Light: Science & Applications*, 8(1):87, 2019.

[19] DE Chang, JS Douglas, Alejandro González-Tudela, C-L Hung, and HJ Kimble. Colloquium: Quantum matter built from nanoscopic lattices of atoms and photons. *Reviews of Modern Physics*, 90(3):031002, 2018.

[20] SY Chen and TC Ralph. Estimation of gravitational acceleration with quantum optical interferometers. *Physical Review A*, 99(2):023803, 2019.

[21] Risheng Cheng, Yiyu Zhou, Sihao Wang, Mohan Shen, Towsif Taher, and Hong X Tang. A 100-pixel photon-number-resolving detector unveiling photon statistics. *Nature Photonics*, 17(1):112–119, 2023.

[22] Sophie Choe. Quantum computing overview: discrete vs. continuous variable models. *arXiv preprint arXiv:2206.07246*, 2022.

[23] RJ Coles, N Prtljaga, B Royall, Isaac John Luxmoore, AM Fox, and MS Skolnick. Waveguide-coupled photonic crystal cavity for quantum dot spin readout. *Optics express*, 22(3):2376–2385, 2014.

[24] Joshua Combes, Joseph Kerckhoff, and Mohan Sarovar. The slh framework for modeling quantum input-output networks. *Advances in Physics: X*, 2(3):784–888, 2017.

[25] Christophe Couteau, Stefanie Barz, Thomas Durt, Thomas Gerrits, Jan Huwer, Robert Prevedel, John Rarity, Andrew Shields, and Gregor Weihs. Applications of single photons in quantum metrology, biology and the foundations of quantum physics. *Nature Reviews Physics*, 5(6):354–363, 2023.

[26] Christophe Couteau, Stefanie Barz, Thomas Durt, Thomas Gerrits, Jan Huwer, Robert Prevedel, John Rarity, Andrew Shields, and Gregor Weihs. Applications of single photons to quantum communication and computing. *Nature Reviews Physics*, 5(6):326–338, 2023.

[27] M Dakna, J Clausen, L Knöll, and D-G Welsch. Generation of arbitrary quantum states of traveling fields. *Physical Review A*, 59(2):1658, 1999.

[28] Mohammed Dakna, Tiemo Anhut, T Opatrný, Ludwig Knöll, and D-G Welsch. Generating schrödinger-cat-like states by means of conditional measurements on a beam splitter. *Physical Review A*, 55(4):3184, 1997.

[29] Xiaowei Deng, Sai Li, Zi-Jie Chen, Zhongchu Ni, Yanyan Cai, Jiasheng Mai, Libo Zhang, Pan Zheng, Haifeng Yu, and Chang-Ling Zou. Quantum-enhanced metrology with large fock states. *Nature Physics*, pages 1–7, 2024.

[30] James S Douglas, Tommaso Caneva, and Darrick E Chang. Photon molecules in atomic gases trapped near photonic crystal waveguides. *Physical Review X*, 6(3):031017, 2016.

[31] Jinjin Du, Wenfang Li, and Michal Bajcsy. Deterministic single-photon subtraction based on a coupled single quantum dot-cavity system. *Optics Express*, 28(5):6835–6845, 2020.

[32] JF Dynes, M Lucamarini, KA Patel, AW Sharpe, MB Ward, ZL Yuan, and AJ Shields. Testing the photon-number statistics of a quantum key distribution light source. *Optics Express*, 26(18):22733–22749, 2018.

[33] Jens Eisert, Stefan Scheel, and Martin B Plenio. Distilling gaussian states with gaussian operations is impossible. *Physical review letters*, 89(13):137903, 2002.

[34] Longfei Fan and M Suhail Zubairy. Quantum illumination using non-gaussian states generated by photon subtraction and photon addition. *Physical Review A*, 98(1):012319, 2018.

[35] Shanhui Fan, Şükrü Ekin Kocabaş, and Jung-Tsung Shen. Input-output formalism for few-photon transport in one-dimensional nanophotonic waveguides coupled to a qubit. *Physical Review A*, 82(6):063821, 2010.

[36] Giovanni Ferioli, Antoine Glicenstein, Igor Ferrier-Barbut, and Antoine Browaeys. A non-equilibrium superradiant phase transition in free space. *Nature Physics*, 19(9):1345–1349, 2023.

[37] Jaromír Fiurášek, Raúl García-Patrón, and Nicolas J Cerf. Conditional generation of arbitrary single-mode quantum states of light by repeated photon subtractions. *Physical Review A*, 72(3):033822, 2005.

[38] Michael Fleischhauer, Atac Imamoglu, and Jonathan P Marangos. Electromagnetically induced transparency: Optics in coherent media. *Reviews of modern physics*, 77(2):633, 2005.

[39] Kosuke Fukui, Rafael N Alexander, and Peter van Loock. All-optical long-distance quantum communication with gottesman-kitaev-preskill qubits. *Physical Review Research*, 3(3):033118, 2021.

[40] AA Gaidash, VI Egorov, and AV Gleim. Revealing of photon-number splitting attack on quantum key distribution system by photon-number resolving devices. In *Journal of Physics: Conference Series*, volume 735, page 012072. IOP Publishing.

[41] Crispin W Gardiner and Matthew J Collett. Input and output in damped quantum systems: Quantum stochastic differential equations and the master equation. *Physical Review A*, 31(6):3761, 1985.

[42] Alexei Gilchrist, Kae Nemoto, William J Munro, Timothy C Ralph, Scott Glancy, Samuel L Braunstein, and Gerard J Milburn. Schrödinger cats and their power for quantum information processing. *Journal of Optics B: Quantum and Semiclassical Optics*, 6(8):S828, 2004.

[43] Roman Goncharov, Alexei D Kiselev, ES Moiseev, E Samsonov, SA Moiseev, F Kiselev, and Vladimir Egorov. Quantum repeaters and teleportation via entangled phase-modulated multimode coherent states. *Physical Review Applied*, 20(4):044030, 2023.

[44] Alexey V Gorshkov, Rejish Nath, and Thomas Pohl. Dissipative many-body quantum optics in rydberg media. *Physical review letters*, 110(15):153601, 2013.

[45] JJMR Gough and Matthew R James. Quantum feedback networks: Hamiltonian formulation. *Communications in Mathematical Physics*, 287:1109–1132, 2009.

[46] John Gough and Matthew R James. The series product and its application to quantum feedforward and feedback networks. *IEEE Transactions on Automatic Control*, 54(11):2530–2544, 2009.

[47] John E. Gough and Guofeng Zhang. Generating nonclassical quantum input field states with modulating filters. *EPJ Quantum Technology*, 2(1):15, 2015.

[48] Hao Hao, Qing-Yuan Zhao, Yang-Hui Huang, Jie Deng, Fan Yang, Sai-Ying Ru, Zhen Liu, Chao Wan, Hao Liu, Zhi-Jian Li, et al. A compact multi-pixel superconducting nanowire single-photon detector array supporting gigabit space-to-ground communications. *Light: Science & Applications*, 13(1):25, 2024.

[49] PR Hemmer, AV Turukhin, MS Shahriar, and JA Musser. Raman-excited spin coherences in nitrogen-vacancy color centers in diamond. *Optics Letters*, 26(6):361–363, 2001.

[50] Anaelle Hertz and Stephan De Bièvre. Decoherence and nonclassicality of photon-added/subtracted multi-mode gaussian states. *arXiv preprint arXiv:2204.06358*, 2022.

[51] Jakob Hinney, Adarsh S Prasad, Sahand Mahmoodian, Klemens Hammerer, Arno Rauschenbeutel, Philipp Schneeweiss, Jürgen Volz, and Max Schemmer. Unraveling two-photon entanglement via the squeezing spectrum of light traveling through nanofiber-coupled atoms. *Physical Review Letters*, 127(12):123602, 2021.

[52] Murray J Holland and Keith Burnett. Interferometric detection of optical phase shifts at the heisenberg limit. *Physical review letters*, 71(9):1355, 1993.

[53] Jens Honer, Robert Löw, Hendrik Weimer, Tilman Pfau, and Hans Peter Büchler. Artificial atoms can do more than atoms: deterministic single photon subtraction from arbitrary light fields. *Physical Review Letters*, 107(9):093601, 2011.

[54] Jonathan D Hood, Akihisa Goban, Ana Asenjo-Garcia, Mingwu Lu, Su-Peng Yu, Darrick E Chang, and HJ Kimble. Atom–atom interactions around the band edge of a photonic crystal waveguide. *Proceedings of the National Academy of Sciences*, 113(38):10507–10512, 2016.

[55] Li-Yun Hu, Chao-Ping Wei, Jie-Hui Huang, and Cun-Jin Liu. Quantum metrology with fock and even coherent states: Parity detection approaches to the heisenberg limit. *Optics Communications*, 323:68–76, 2014.

[56] David L. Hurst and Pieter Kok. Analytic few-photon scattering in waveguide qed. *Physical Review A*, 97(4):043850, 2018. PRA.

[57] Denis Ilin and Alexander V Poshakinskiy. Many-photon scattering and entangling in a waveguide with a λ-type atom. *Physical Review A*, 109(3):033710, 2024.

[58] Ole A. Iversen and Thomas Pohl. Strongly correlated states of light and repulsive photons in chiral chains of three-level quantum emitters. *Physical Review Letters*, 126(8):083605, 2021. PRL.

[59] Ole A. Iversen and Thomas Pohl. Self-ordering of individual photons in waveguide qed and rydberg-atom arrays. *Physical Review Research*, 4(2):023002, 2022. PRRESEARCH.

[60] Dirk Jalas, Alexander Petrov, Manfred Eich, Wolfgang Freude, Shanhui Fan, Zongfu Yu, Roel Baets, Miloš Popović, Andrea Melloni, John D. Joannopoulos, Mathias Vanwolleghem, Christopher R. Doerr, and Hagen Renner. What is — and what is not — an optical isolator. *Nature Photonics*, 7(8):579–582, 2013.

[61] Hyunseok Jeong, Alessandro Zavatta, Minsu Kang, Seung-Woo Lee, Luca S Costanzo, Samuele Grandi, Timothy C Ralph, and Marco Bellini. Generation of hybrid entanglement of light. *Nature Photonics*, 8(7):564–569, 2014.

[62] Christian Junge, Danny O'shea, Jürgen Volz, and Arno Rauschenbeutel. Strong coupling between single atoms and nontransversal photons. *Physical review letters*, 110(21):213604, 2013.

[63] Alexander Holm Kiilerich and Klaus Mølmer. Input-output theory with quantum pulses. *Physical review letters*, 123(12):123604, 2019.

[64] Hyochul Kim, Ranojoy Bose, Thomas C Shen, Glenn S Solomon, and Edo Waks. A quantum logic gate between a solid-state quantum bit and a photon. *Nature Photonics*, 7(5):373–377, 2013.

[65] Michael K Koch, Michael Hoese, Vibhav Bharadwaj, Johannes Lang, John P Hadden, Roberta Ramponi, Fedor Jelezko, Shane M Eaton, and Alexander Kubanek. On-chip single-photon subtraction by individual silicon vacancy centers in a laser-written diamond waveguide. *arXiv preprint arXiv:2111.01699*, 2021.

[66] Marina Kudra, Tahereh Abad, Mikael Kervinen, Axel M Eriksson, Fernando Quijandría, Per Delsing, and Simone Gasparinetti. Experimental realization of deterministic and selective photon addition in a bosonic mode assisted by an ancillary qubit. *arXiv preprint arXiv:2212.12079*, 2022.

[67] SP Kulik, KS Kravtsov, and SN Molotkov. Experimental resources needed to implement photon number splitting attack in quantum cryptography. *Laser Physics Letters*, 19(2):025203, 2022.

[68] R Kumar, E Barrios, C Kupchak, and AI Lvovsky. Experimental characterization of bosonic creation and annihilation operators. *Physical Review Letters*, 110(13):130403, 2013.

[69] Kazuhiro Kuruma, Yasutomo Ota, Masahiro Kakuda, Satoshi Iwamoto, and Yasuhiko Arakawa. Strong coupling between a single quantum dot and an l4/3 photonic crystal nanocavity. *Applied Physics Express*, 13(8):082009, 2020.

[70] Hanna Le Jeannic, Tomás Ramos, Signe F Simonsen, Tommaso Pregnolato, Zhe Liu, Rüdiger Schott, Andreas D Wieck, Arne Ludwig, Nir Rotenberg, and Juan José García-Ripoll. Experimental reconstruction of the few-photon nonlinear scattering matrix from a single quantum dot in a nanophotonic waveguide. *Physical Review Letters*, 126(2):023603, 2021.

[71] Changhyoup Lee, Changsuk Noh, Nikolaos Schetakis, and Dimitris G Angelakis. Few-photon transport in many-body photonic systems: A scattering approach. *Physical Review A*, 92(6):063817, 2015.

[72] Zeyang Liao, Yunning Lu, and M. Suhail Zubairy. Multiphoton pulses interacting with multiple emitters in a one-dimensional waveguide. *Physical Review A*, 102(5):053702, 2020. PRA.

[73] Zeyang Liao, Xiaodong Zeng, Hyunchul Nha, and M Suhail Zubairy. Photon transport in a one-dimensional nanophotonic waveguide qed system. *Physica Scripta*, 91(6):063004, 2016.

[74] Christian Liedl, Felix Tebbenjohanns, Constanze Bach, Sebastian Pucher, Arno Rauschenbeutel, and Philipp Schneeweiss. Observation of superradiant bursts in a cascaded quantum system. *Physical Review X*, 14(1):011020, 2024.

[75] Qihang Liu and Jung-Tsung Shen. Photonic fock state generation using superradiance. *Optics Letters*, 47(17):4576–4579, 2022.

[76] Shikai Liu, Oliver August Dall'Alba Sandberg, Ming Lai Chan, Björn Schrinski, Yiouli Anyfantaki, Rasmus B Nielsen, Robert G Larsen, Andrei Skalkin, Ying Wang, and Leonardo Midolo. Violation of bell inequality by photon scattering on a two-level emitter. *Nature Physics*, pages 1–5, 2024.

[77] Peter Lodahl, Sahand Mahmoodian, Søren Stobbe, Arno Rauschenbeutel, Philipp Schneeweiss, Jürgen Volz, Hannes Pichler, and Peter Zoller. Chiral quantum optics. *Nature*, 541(7638):473–480, 2017.

[78] Rodney Loudon. *The quantum theory of light*. OUP Oxford, 2000.

[79] Austin P Lund, Timothy C Ralph, and Henry L Haselgrove. Fault-tolerant linear optical quantum computing with small-amplitude coherent states. *Physical review letters*, 100(3):030503, 2008.

[80] AI Lvovsky, Philippe Grangier, Alexei Ourjoumtsev, Valentina Parigi, Masahide Sasaki, and Rosa Tualle-Brouri. Production and applications of non-gaussian quantum states of light. *arXiv preprint arXiv:2006.16985*, 2020.

[81] Sahand Mahmoodian, Giuseppe Calajó, Darrick E. Chang, Klemens Hammerer, and Anders S. Sørensen. Dynamics of many-body photon bound states in chiral waveguide qed. *Physical Review X*, 10(3):031011, 2020. PRX.

[82] Logan O Mailloux, Douglas D Hodson, Michael R Grimaila, Ryan D Engle, Colin V Mclaughlin, and Gerald B Baumgartner. Using modeling and simulation to study photon number splitting attacks. *IEEE Access*, 4:2188–2197, 2016.

[83] Bellini Marco and Zavatta Alessandro. *Manipulating light states by single-photon addition and subtraction*, volume 55, pages 41–83. Elsevier, 2010.

[84] Luke Masters, Xin-Xin Hu, Martin Cordier, Gabriele Maron, Lucas Pache, Arno Rauschenbeutel, Max Schemmer, and Jürgen Volz. On the simultaneous scattering of two photons by a single two-level atom. *Nature Photonics*, 17(11):972–976, 2023.

[85] Rudolf Mitsch, Clément Sayrin, Bernhard Albrecht, Philipp Schneeweiss, and Arno Rauschenbeutel. Quantum state-controlled directional spontaneous emission of photons into a nanophotonic waveguide. *Nature communications*, 5(1):5713, 2014.

[86] Sreraman Muralidharan, Linshu Li, Jungsang Kim, Norbert Lütkenhaus, Mikhail D Lukin, and Liang Jiang. Optimal architectures for long distance quantum communication. *Scientific reports*, 6(1):20463, 2016.

[87] C Sánchez Muñoz, E Del Valle, A González Tudela, K Müller, S Lichtmannecker, M Kaniber, C Tejedor, JJ Finley, and FP Laussy. Emitters of n-photon bundles. *Nature photonics*, 8(7):550–555, 2014.

[88] Klaus Mølmer, Yvan Castin, and Jean Dalibard. Monte carlo wave-function method in quantum optics. *JOSA B*, 10(3):524–538, 1993.

[89] Julien Niset, Jaromír Fiurášek, and Nicolas J Cerf. No-go theorem for gaussian quantum error correction. *Physical review letters*, 102(12):120501, 2009.

[90] H. I. Nurdin, M. R. James, and N. Yamamoto. Perfect single device absorber of arbitrary traveling single photon fields with a tunable coupling parameter: A qsde approach. In *2016 IEEE 55th Conference on Decision and Control (CDC)*, pages 2513–2518.

[91] Yasutomo Ota, Daisaku Takamiya, Ryuichi Ohta, Hiroyuki Takagi, Naoto Kumagai, Satoshi Iwamoto, and Yasuhiko Arakawa. Large vacuum rabi splitting between a single quantum dot and an h0 photonic crystal nanocavity. *Applied Physics Letters*, 112(9), 2018.

[92] Alexei Ourjoumtsev, Aurelien Dantan, Rosa Tualle-Brouri, and Philippe Grangier. Increasing entanglement between gaussian states by coherent photon subtraction. *Physical review letters*, 98(3):030502, 2007.

[93] Alexei Ourjoumtsev, Rosa Tualle-Brouri, Julien Laurat, and Philippe Grangier. Generating optical schrodinger kittens for quantum information processing. *Science*, 312(5770):83–86, 2006.

[94] Valentina Parigi, Alessandro Zavatta, Myungshik Kim, and Marco Bellini. Probing quantum commutation rules by addition and subtraction of single photons to/from a light field. *Science*, 317(5846):1890–1893, 2007.

[95] Abdolreza Pasharavesh and Michal Bajcsy. Deterministic single photon subtraction with a cascade of waveguide-coupled atoms. *Optics Express*, 32(15):26740–26750, 2024.

[96] Abdolreza Pasharavesh and Michal Bajcsy. Generation of non-gaussian states of light using deterministic photon subtraction. *New Journal of Physics*, 26(11):113022, 2024.

[97] Abdolreza Pasharavesh and Michal Bajcsy. Multi-photon fock state generation via selective single photon subtraction in a cascaded waveguide qed system. *Advanced Quantum Technologies*, 8(9):2400616, 2025.

[98] Abdolreza Pasharavesh and Michal Bajcsy. Photon transport in bimodal atom-cavity systems with waveguide coupling: Application to deterministic photon subtraction. *Physical Review Research*, 7(1):013018, 2025.

[99] Abdolreza Pasharavesh, Sai Sreesh Venuturumilli, and Michal Bajcsy. Photon-number-resolving detector based on a cascade of waveguide-coupled quantum emitters. *arXiv preprint arXiv:2507.09034*, 2025.

[100] Yun Peng, Sen Qin, Siqi Zhang, and Yong Zhao. Optical fiber quantum temperature sensing based on single photon interferometer. *Optics and Lasers in Engineering*, 167:107611, 2023.

[101] Martí Perarnau-Llobet, A González-Tudela, and J Ignacio Cirac. Multimode fock states with large photon number: effective descriptions and applications in quantum metrology. *Quantum Science and Technology*, 5(2):025003, 2020.

[102] Jan Petersen, Jürgen Volz, and Arno Rauschenbeutel. Chiral nanophotonic waveguide interface based on spin-orbit interaction of light. *Science*, 346(6205):67–71, 2014.

[103] Fabrizio Piacentini, MP Levi, Alessio Avella, M López, S Kück, SV Polyakov, Ivo P Degiovanni, Giorgio Brida, and Marco Genovese. Positive operator-valued measure reconstruction of a beam-splitter tree-based photon-number-resolving detector. *Optics letters*, 40(7):1548–1551, 2015.

[104] Kiryl Piasotski and Mikhail Pletyukhov. Diagrammatic approach to scattering of multiphoton states in waveguide qed. *Physical Review A*, 104(2):023709, 2021.

[105] Dorothea Pinotsi and Atac Imamoglu. Single photon absorption by a single quantum emitter. *Physical review letters*, 100(9):093603, 2008.

[106] Adarsh S Prasad, Jakob Hinney, Sahand Mahmoodian, Klemens Hammerer, Samuel Rind, Philipp Schneeweiss, Anders S Sørensen, Jürgen Volz, and Arno Rauschenbeutel. Correlating photons using the collective nonlinear response of atoms weakly coupled to an optical mode. *Nature Photonics*, 14(12):719–722, 2020.

[107] Yi-Dan Qu, Yuan Zhang, Peinan Ni, Chongxin Shan, Hunger David, and Klaus Mølmer. Superradiance from nitrogen vacancy centers coupled to an ultranarrow optical cavity. *arXiv preprint arXiv:2407.09755*, 2024.

[108] Young-Sik Ra, Clément Jacquard, Adrien Dufour, Claude Fabre, and Nicolas Treps. Tomography of a mode-tunable coherent single-photon subtractor. *Physical Review X*, 7(3):031012, 2017.

[109] Dominik Gerhard Rabus, Cinzia Sada, Dominik Gerhard Rabus, and Cinzia Sada. Ring resonators: Theory and modeling. *Integrated Ring Resonators: A Compendium*, pages 3–46, 2020.

[110] Michael G Raymer and Ian A Walmsley. Temporal modes in quantum optics: then and now. *Physica Scripta*, 95(6):064002, 2020.

[111] Dileep V Reddy and Michael G Raymer. High-selectivity quantum pulse gating of photonic temporal modes using all-optical ramsey interferometry. *Optica*, 5(4):423–428, 2018.

[112] Dileep V Reddy, Michael G Raymer, and Colin J McKinstrie. Efficient sorting of quantum-optical wave packets by temporal-mode interferometry. *Optics letters*, 39(10):2924–2927, 2014.

[113] Thorsten Reichert, Stefan Lichtmannecker, Günther Reithmaier, Martin Zeitlmair, Julia Wembacher, Andreas Rauscher, Max Bichler, Kai Müller, Michael Kaniber, and Jonathan James Finley. Highly directed emission from self-assembled quantum dots into guided modes in disordered photonic-crystal waveguides. *Physical Review B*, 90(11):115310, 2014.

[114] Andreas Reiserer and Gerhard Rempe. Cavity-based quantum networks with single atoms and optical photons. *Reviews of Modern Physics*, 87(4):1379–1418, 2015.

[115] Eden Rephaeli and Shanhui Fan. Few-photon single-atom cavity qed with input-output formalism in fock space. *IEEE Journal of Selected Topics in Quantum Electronics*, 18(6):1754–1762, 2012.

[116] Kelley Rivoire, Sonia Buckley, and Jelena Vučković. Multiply resonant photonic crystal nanocavities for nonlinear frequency conversion. *Optics express*, 19(22):22198–22207, 2011.

[117] Brendon C Rose, Ding Huang, Zi-Huai Zhang, Paul Stevenson, Alexei M Tyryshkin, Sorawis Sangtawesin, Srikanth Srinivasan, Lorne Loudin, Matthew L Markham, Andrew M Edmonds, et al. Observation of an environmentally insensitive solid-state spin defect in diamond. *Science*, 361(6397):60–63, 2018.

[118] Serge Rosenblum, Orel Bechler, Itay Shomroni, Yulia Lovsky, Gabriel Guendelman, and Barak Dayan. Extraction of a single photon from an optical pulse. *Nature Photonics*, 10(1):19–22, 2016.

[119] Serge Rosenblum, Adrien Borne, and Barak Dayan. Analysis of photonic quantum nodes based on single photon raman interaction. *arXiv preprint arXiv:1412.0604*, 2014.

[120] Supratik Sarkar. *Creating and shaping light at single photon level*. Thesis, 2021.

[121] H. Z. Shen, Cheng Shang, Y. H. Zhou, and X. X. Yi. Unconventional single-photon blockade in non-markovian systems. *Physical Review A*, 98(2):023856, 2018. PRA.

[122] Jung-Tsung Shen and Shanhui Fan. Strongly correlated two-photon transport in a one-dimensional waveguide coupled¡? format?¿ to a two-level system. *Physical review letters*, 98(15):153003, 2007.

[123] Yuecheng Shen and Jung-Tsung Shen. Photonic-fock-state scattering in a waveguide-qed system and their correlation functions. *Physical Review A*, 92(3):033803, 2015. PRA.

[124] Tao Shi, Darrick E. Chang, and J. Ignacio Cirac. Multiphoton-scattering theory and generalized master equations. *Physical Review A*, 92(5):053834, 2015. PRA.

[125] Itay Shomroni, Serge Rosenblum, Yulia Lovsky, Orel Bechler, Gabriel Guendelman, and Barak Dayan. All-optical routing of single photons by a one-atom switch controlled by a single photon. *Science*, 345(6199):903–906, 2014.

[126] Hamidreza Siampour, Christopher O'Rourke, Alistair J Brash, Maxim N Makhonin, René Dost, Dominic J Hallett, Edmund Clarke, Pallavi K Patil, Maurice S Skolnick, and A Mark Fox. Observation of large spontaneous emission rate enhancement of quantum dots in a broken-symmetry slow-light waveguide. *npj Quantum Information*, 9(1):15, 2023.

[127] Sergei Slussarenko and Geoff J Pryde. Photonic quantum information processing: A concise review. *Applied Physics Reviews*, 6(4), 2019.

[128] ÖO Soykal, Pratibha Dev, and Sophia E Economou. Silicon vacancy center in 4 h-sic: Electronic structure and spin-photon interfaces. *Physical Review B*, 93(8):081207, 2016.

[129] Nina Stiesdal, Hannes Busche, Kevin Kleinbeck, Jan Kumlin, Mikkel G. Hansen, Hans Peter Büchler, and Sebastian Hofferberth. Controlled multi-photon subtraction with cascaded rydberg superatoms as single-photon absorbers. *Nature Communications*, 12(1):4328, 2021.

[130] Ivo Straka, Lukáš Lachman, Josef Hloušek, Martina Miková, Michal Mičuda, Miroslav Ježek, and Radim Filip. Quantum non-gaussian multiphoton light. *npj Quantum Information*, 4(1):4, 2018.

[131] XueJian Sun, WenXiao Liu, Hao Chen, ChengYuan Wang, HuiZhong Ma, and HongRong Li. Single-photon transport in a waveguide-cavity-emitter system. *International Journal of Theoretical Physics*, 61(8):216, 2022.

[132] Immo Söllner, Sahand Mahmoodian, Sofie Lindskov Hansen, Leonardo Midolo, Alisa Javadi, Gabija Kiršanskė, Tommaso Pregnolato, Haitham El-Ella, Eun Hye Lee, and Jin Dong Song. Deterministic photon–emitter coupling in chiral photonic circuits. *Nature nanotechnology*, 10(9):775–778, 2015.

[133] Hiroki Takahashi, Jonas S Neergaard-Nielsen, Makoto Takeuchi, Masahiro Takeoka, Kazuhiro Hayasaka, Akira Furusawa, and Masahide Sasaki. Entanglement distillation from gaussian input states. *Nature photonics*, 4(3):178–181, 2010.

[134] Naoto Takanashi, Wataru Inokuchi, Takahiro Serikawa, and Akira Furusawa. Generation and measurement of a squeezed vacuum up to 100 mhz at 1550 nm with a

semi-monolithic optical parametric oscillator designed towards direct coupling with waveguide modules. *Optics Express*, 27(13):18900–18909, 2019.

[135] Shuntaro Takeda and Akira Furusawa. Toward large-scale fault-tolerant universal photonic quantum computing. *APL Photonics*, 4(6), 2019.

[136] Malte C Tichy. Sampling of partially distinguishable bosons and the relation to the multidimensional permanent. *Physical Review A*, 91(2):022316, 2015.

[137] Emre Togan, Yiwen Chu, Alexei S Trifonov, Liang Jiang, Jeronimo Maze, Lilian Childress, MV Gurudev Dutt, Anders Søndberg Sørensen, Phillip R Hemmer, and Alexander S Zibrov. Quantum entanglement between an optical photon and a solid-state spin qubit. *Nature*, 466(7307):730–734, 2010.

[138] Christoph Tresp, Christian Zimmer, Ivan Mirgorodskiy, Hannes Gorniaczyk, Asaf Paris-Mandoki, and Sebastian Hofferberth. Single-photon absorber based on strongly interacting rydberg atoms. *Physical Review Letters*, 117(22):223001, 2016.

[139] Patrick Tritschler, Torsten Ohms, André Zimmermann, Fabian Zschocke, Thomas Strohm, and Peter Degenfeld-Schonburg. Optical interferometer using two-mode squeezed light for enhanced chip-integrated quantum metrology. *Physical Review A*, 110(1):012621, 2024.

[140] Rahul Trivedi, Kevin Fischer, Shanshan Xu, Shanhui Fan, and Jelena Vuckovic. Few-photon scattering and emission from low-dimensional quantum systems. *Physical Review B*, 98(14):144112, 2018. PRB.

[141] Mark Um, Junhua Zhang, Dingshun Lv, Yao Lu, Shuoming An, Jing-Ning Zhang, Hyunchul Nha, MS Kim, and Kihwan Kim. Phonon arithmetic in a trapped ion system. *Nature communications*, 7(1):11410, 2016.

[142] Manuel Uria, P Solano, and Carla Hermann-Avigliano. Deterministic generation of large fock states. *Physical Review Letters*, 125(9):093603, 2020.

[143] DF Walls and Gerard J Milburn. Input–output formulation of optical cavities. *Quantum optics*, pages 127–141, 2008.

[144] Mattia Walschaers. Non-gaussian quantum states and where to find them. *PRX quantum*, 2(3):030204, 2021.

[145] Hao-Cheng Weng and Chih-Sung Chuu. Implementation of shor's algorithm with a single photon in 32 dimensions. *Physical Review Applied*, 22(3):034003, 2024.

[146] Jérôme Wenger, Rosa Tualle-Brouri, and Philippe Grangier. Non-gaussian statistics from individual pulses of squeezed light. *Physical review letters*, 92(15):153601, 2004.

[147] Feihu Xu, Marcos Curty, Bing Qi, Li Qian, and Hoi-Kwong Lo. Discrete and continuous variables for measurement-device-independent quantum cryptography. *Nature Photonics*, 9(12):772–773, 2015.

[148] Shanshan Xu and Shanhui Fan. Input-output formalism for few-photon transport: A systematic treatment beyond two photons. *Physical Review A*, 91(4):043845, 2015. PRA.

[149] Cong-Hua Yan, Wen-Zhi Jia, and Lian-Fu Wei. Controlling single-photon transport with three-level quantum dots in photonic crystals. *Physical Review A*, 89(3):033819, 2014.

[150] Min Yu, Yu Liu, Pengcheng Yang, Musang Gong, Qingyun Cao, Shaoliang Zhang, Haibin Liu, Markus Heyl, Tomoki Ozawa, and Nathan Goldman. Quantum fisher information measurement and verification of the quantum cramér–rao bound in a solid-state qubit. *npj Quantum Information*, 8(1):56, 2022.

[151] A Zavatta, V Parigi, MS Kim, and M Bellini. Subtracting photons from arbitrary light fields: experimental test of coherent state invariance by single-photon annihilation. *New Journal of Physics*, 10(12):123006, 2008.

[152] Alessandro Zavatta, Silvia Viciani, and Marco Bellini. Quantum-to-classical transition with single-photon-added coherent states of light. *science*, 306(5696):660–662, 2004.

[153] Kun Zhang, Jietai Jing, Nicolas Treps, and Mattia Walschaers. Maximal entanglement increase with single-photon subtraction. *Quantum*, 6:704, 2022.

[154] Zheshen Zhang and Quntao Zhuang. Distributed quantum sensing. *Quantum Science and Technology*, 6(4):043001, 2021.

APPENDICES

Appendix A

Derivation of the Optical Bloch Equations

To find the set of governing Bloch equations given in equation 3.1, one must initially derive the total Hamiltonian of the system, which is the summation of the waveguide's Hamiltonian H_{wg}, emitter's Hamiltonian H_{e}, and their interaction Hamiltonian H_{int}:

$$H_{\text{tot}} = H_{\text{wg}} + H_{\text{e}} + H_{\text{int}} \tag{A.1}$$

where the different terms can be expressed as follows:

$$\begin{aligned} H_{\text{wg}} &= \int_{-\infty}^{+\infty} \left(r_\omega^\dagger r_\omega - l_\omega^\dagger l_\omega\right) \omega d\omega \\ H_{\text{e}} &= \omega_1 \sigma_{33} + (\omega_1 - \omega_2)\, \sigma_{22} \\ H_{\text{int}} &= iV_R \int_{-\infty}^{+\infty} \left(r_\omega^\dagger \sigma_{13} - \sigma_{31} r_\omega\right) d\omega + iV_L \int_{-\infty}^{+\infty} \left(l_\omega^\dagger \sigma_{23} - \sigma_{32} l_\omega\right) d\omega \end{aligned} \tag{A.2}$$

In the above equation, $\sigma_{ij} = |i\rangle \langle j|$ is the atomic transition operator, ω_i is the transition frequency from the excited state to the ground state $|i\rangle$, $r_\omega(l_\omega)$ is the annihilation operator for a right (left) propagating mode of frequency ω, and $V_R(V_L)$ is the coupling strength between the light propagating in right (left) direction with the corresponding atomic transition.

Heisenberg equation of motion can be used to obtain time derivatives of any arbitrary operator $A(t)$ in the Heisenberg picture ($\hbar = 1$):

$$\frac{dA(t)}{dt} = i\left[H_{\text{tot}}, A(t)\right] \tag{A.3}$$

This, after substituting in equations A.1 and A.2, results in the following set of ordinary differential equations governing time evolution of different atomic transition operators:

$$\begin{aligned}
\dot{\sigma}_{11} &= V_R \int_{-\infty}^{+\infty} \left(\sigma_{31} r_\omega + r_\omega^\dagger \sigma_{13}\right) d\omega \\
\dot{\sigma}_{22} &= V_L \int_{-\infty}^{+\infty} \left(\sigma_{32} l_\omega + l_\omega^\dagger \sigma_{23}\right) d\omega \\
\dot{\sigma}_{33} &= -V_R \int_{-\infty}^{+\infty} \left(r_\omega^\dagger \sigma_{13} + \sigma_{31} r_\omega\right) d\omega - V_L \int_{-\infty}^{+\infty} \left(l_\omega^\dagger \sigma_{23} + \sigma_{32} l_\omega\right) d\omega \\
\dot{\sigma}_{13} &= -i\omega_1 \sigma_{13} + V_R \int_{-\infty}^{+\infty} \left(\left(\sigma_{33} - \sigma_{11}\right) r_\omega\right) d\omega - V_L \int_{-\infty}^{+\infty} \left(\sigma_{12} l_\omega\right) d\omega \\
\dot{\sigma}_{23} &= -i\omega_2 \sigma_{23} + V_L \int_{-\infty}^{+\infty} \left(\left(\sigma_{33} - \sigma_{22}\right) l_\omega\right) d\omega - V_R \int_{-\infty}^{+\infty} \left(\sigma_{21} r_\omega\right) d\omega \\
\dot{\sigma}_{12} &= -i\left(\omega_1 - \omega_2\right) \sigma_{12} + V_R \int_{-\infty}^{+\infty} \left(\sigma_{32} r_\omega\right) d\omega + V_L \int_{-\infty}^{+\infty} \left(l_\omega^\dagger \sigma_{13}\right) d\omega
\end{aligned} \tag{A.4}$$

Also, for the right and left propagating field operators, one obtains:

$$\dot{r}_\omega = -i\omega r_\omega + V_R \sigma_{13} \qquad \dot{l}_\omega = i\omega l_\omega + V_L \sigma_{23} \tag{A.5}$$

which after integration gives:

$$r_\omega = r_\omega|_{t=t_0} e^{-i\omega(t-t_0)} + V_R \int_{t_0}^{t} \sigma_{13} e^{-i\omega(t-t')} dt' \qquad l_\omega = l_\omega|_{t=t_0} e^{i\omega(t-t_0)} + V_L \int_{t_0}^{t} \sigma_{23} e^{-i\omega(t-t')} dt' \tag{A.6}$$

Substituting equation A.6 into A.4 results in the set of optical Bloch equations given in equation 3.1, where input operators r_{in} and l_{in} are defined as Fourier transform of the bath operators r_ω and l_ω at time $t = t_0$, before the light starts interacting with the emitter:

$$r_{in}(t) := \frac{1}{\sqrt{2\pi}} \int_{-\infty}^{+\infty} d\omega' r_{\omega'}(t_0) e^{-i\omega'(t-t_0)} \qquad l_{in}(t) := \frac{1}{\sqrt{2\pi}} \int_{-\infty}^{+\infty} d\omega' l_{\omega'}(t_0) e^{i\omega'(t-t_0)} \tag{A.7}$$

In deriving equation 3.1, we assume that the coupling strengths V_R and V_L are equal and express them in terms of the emission rate γ_g of the atom to the guided modes of the waveguide as $V_R = V_L = \sqrt{\gamma_g / 2\pi}$. Using a similar approach to equation A.7, one can

define the output operators r_{out} and l_{out} to keep track of the output light from the system at time $t = t_1$, which is after the interaction ends:

$$r_{out}(t) = \frac{1}{\sqrt{2\pi}} \int_{-\infty}^{+\infty} d\omega' r_{\omega'}(t_1) e^{-i\omega'(t-t_1)} \qquad l_{out}(t) = \frac{1}{\sqrt{2\pi}} \int_{-\infty}^{+\infty} d\omega' l_{\omega'}(t_1) e^{i\omega'(t-t_1)} \quad \text{(A.8)}$$

Integrating equation A.6 over all frequencies, and then substituting equations A.7 and A.8, yields the input-output relations for the system as given in equation 3.2.

Appendix B

Derivation of First Autocorrelation Matrix

B.1 Squeezed vacuum input

When the input is in the squeezed vacuum state $|\zeta\rangle_0 = \hat{S}(\zeta)|0\rangle$ with the complex squeeze parameter $\zeta = se^{i\theta}$, we can define the state obtained by annihilating n photons from the original vacuum state as $|\zeta\rangle_n = a^n|\zeta\rangle_0$ where a is the annihilation operator of the corresponding mode. Then, using the notation ${}_i\langle\sigma_{ab}\rangle_j = {}_i\langle\zeta|\sigma_{ab}|\zeta\rangle_j$, we express the equations set 3.11 and 3.12 as follows:

$$\begin{aligned}
\partial_t\langle\sigma_{11}\rangle &= \sqrt{\gamma_g}\left({}_n\langle\sigma_{31}\rangle_{n+1}\alpha(t) + \alpha^*(t)\,{}_{n+1}\langle\sigma_{13}\rangle_n\right) + \gamma_g\langle\sigma_{33}\rangle \\
\partial_t\langle\sigma_{33}\rangle &= -\sqrt{\gamma_g}\left({}_n\langle\sigma_{31}\rangle_{n+1}\alpha(t) + \alpha^*(t){}_{n+1}\langle\sigma_{13}\rangle_n\right) - 2\gamma_g\langle\sigma_{33}\rangle \\
\partial_t\langle\sigma_{13}\rangle &= \sqrt{\gamma_g}\left({}_n\langle\sigma_{33}\rangle_{n+1} - {}_n\langle\sigma_{11}\rangle_{n+1}\right)\alpha(t) - \gamma_g\langle\sigma_{13}\rangle \\
\partial_t\langle\sigma_{31}\rangle &= \sqrt{\gamma_g}\left({}_{n+1}\langle\sigma_{33}\rangle_n - {}_{n+1}\langle\sigma_{11}\rangle_n\right)\alpha^*(t) - \gamma_g\langle\sigma_{31}\rangle \\
\partial_t\langle\sigma_{32}\rangle &= -\sqrt{\gamma_g}{}_{n+1}\langle\sigma_{12}\rangle_n\alpha^*(t) - \gamma_g\langle\sigma_{32}\rangle \\
\partial_t\langle\sigma_{12}\rangle &= \sqrt{\gamma_g}{}_n\langle\sigma_{32}\rangle_{n+1}\alpha(t)
\end{aligned} \tag{B.1}$$

and:

$$\begin{aligned}
\partial_{t_2}\langle\sigma_{11}(t_2)\sigma_{13}(t_1)\rangle &= \sqrt{\gamma_g}\left({}_n\langle\sigma_{31}(t_2)\sigma_{13}(t_1)\rangle_{n+1}\alpha(t_2) + \alpha^*(t_2)\,{}_{n+1}\langle\sigma_{13}(t_2)\sigma_{13}(t_1)\rangle_n\right) + \gamma_g\langle\sigma_{33}(t_2)\sigma_{13}(t_1)\rangle \\
\partial_{t_2}\langle\sigma_{33}(t_2)\sigma_{13}(t_1)\rangle &= -\sqrt{\gamma_g}\left({}_n\langle\sigma_{31}(t_2)\sigma_{13}(t_1)\rangle_{n+1}\alpha(t_2) + \alpha^*(t_2){}_{n+1}\langle\sigma_{13}(t_2)\sigma_{13}(t_1)\rangle_n\right) - 2\gamma_g\langle\sigma_{33}(t_2)\sigma_{13}(t_1)\rangle \\
\partial_{t_2}\langle\sigma_{13}(t_2)\sigma_{13}(t_1)\rangle &= \sqrt{\gamma_g}\left({}_n\langle\sigma_{33}(t_2)\sigma_{13}(t_1)\rangle_{n+1} - {}_n\langle\sigma_{11}(t_2)\sigma_{13}(t_1)\rangle_{n+1}\right)\alpha(t_2) - \gamma_g\langle\sigma_{13}(t_2)\sigma_{13}(t_1)\rangle \\
\partial_{t_2}\langle\sigma_{31}(t_2)\sigma_{13}(t_1)\rangle &= \sqrt{\gamma_g}\left({}_{n+1}\langle\sigma_{33}(t_2)\sigma_{13}(t_1)\rangle_n - {}_{n+1}\langle\sigma_{11}(t_2)\sigma_{13}(t_1)\rangle_n\right)\alpha^*(t_2) - \gamma_g\langle\sigma_{31}(t_2)\sigma_{13}(t_1)\rangle \\
\partial_{t_2}\langle\sigma_{32}(t_2)\sigma_{23}(t_1)\rangle &= -\sqrt{\gamma_g}{}_{n+1}\langle\sigma_{12}(t_2)\sigma_{23}(t_1)\rangle_n\alpha^*(t_2) - \gamma_g\langle\sigma_{32}(t_2)\sigma_{23}(t_1)\rangle \\
\partial_{t_2}\langle\sigma_{12}(t_2)\sigma_{23}(t_1)\rangle &= \sqrt{\gamma_g}{}_n\langle\sigma_{32}(t_2)\sigma_{23}(t_1)\rangle_{n+1}\alpha(t_2)
\end{aligned} \tag{B.2}$$

Both equations B.1 and B.2 represent sets of recurrence equations, similar to the case of Fock state input. As n increases, $|\zeta\rangle_n$ tends toward zero, allowing for truncation at a sufficiently large n, after which the equations can be solved. The initial conditions for equation B.2 are analogous to those provided in equation 3.13. Furthermore, in accordance with the photon number distribution of the squeezed vacuum state, which is as follows:

$$|\zeta\rangle = \sum_n \frac{\left(-e^{i\theta}\tanh s\right)^n}{\sqrt{\cosh s}} \frac{(2n!)^{\frac{1}{2}}}{2^n n!} |2n\rangle \tag{B.3}$$

the nonzero initial conditions for equation B.1 will be:

$$\begin{aligned}
{}_i\langle\sigma_{11}\rangle_j &= \sum_n \frac{\left(-e^{i\theta}\tanh s\right)^{2n+\frac{i+j}{2}+1}}{\cosh s} \left[\frac{\left(2\left(n+\frac{i+1}{2}\right)!\right)\left(2\left(n+\frac{j+1}{2}\right)!\right)}{2^{2n+\frac{i+j}{2}+1}\left(n+\frac{i+1}{2}\right)!\left(n+\frac{j+1}{2}\right)!(2n+1)!}\right] \qquad i \text{ and } j \text{ are both odd} \\
{}_i\langle\sigma_{11}\rangle_j &= \sum_n \frac{\left(-e^{i\theta}\tanh s\right)^{2n+\frac{i+j}{2}}}{\cosh s} \left[\frac{((2n+i)!)((2n+j)!)}{2^{2n+\frac{i+j}{2}}\left(n+\frac{i}{2}\right)!\left(n+\frac{j}{2}\right)!(2n)!}\right] \qquad i \text{ and } j \text{ are both even}
\end{aligned} \tag{B.4}$$

Solving equation B.2 gives the first correlation terms appearing on the right-hand side of equation 3.8. For the other three correlation terms appeared in equation 3.8, one can write:

$$\begin{aligned}
\left\langle {r_{in}}^\dagger(t_2)\, r_{in}(t_1)\right\rangle &= \left(\sum_n \frac{\left(-e^{i\theta}\tanh s\right)^{2n+2}}{\cosh s}\left[\frac{(2(n+1)!)^2}{2^{2n+2}((n+1)!)^2(2n+1)!}\right]\right)\alpha^*(t_2)\,\alpha(t_1) \\
\left\langle {r_{in}}^\dagger(t_2)\,\sigma_{13}(t_1)\right\rangle &= \alpha^*(t_2)\,{}_1\langle\sigma_{13}(t_1)\rangle_0 \\
\left\langle \sigma_{31}(t_2)\, r_{in}(t_1)\right\rangle &= {}_0\langle\sigma_{31}(t_2)\rangle_1\alpha(t_1)
\end{aligned} \tag{B.5}$$

B.2 Coherent input

For the case where the input pulse is in a coherent state $|\alpha\rangle$, one has $r_{in}(t)|\alpha\rangle = \alpha(t)|\alpha\rangle$. Taking the expectation values of both sides of equation 3.1 yields:

$$\begin{aligned}
\partial_t\langle\sigma_{11}\rangle &= \sqrt{\gamma_g}\left(\langle\sigma_{31}\rangle\alpha(t) + \alpha^*(t)\langle\sigma_{13}\rangle\right) + \gamma_g\langle\sigma_{33}\rangle \\
\partial_t\langle\sigma_{33}\rangle &= -\sqrt{\gamma_g}\left(\langle\sigma_{31}\rangle\alpha(t) + \alpha^*(t)\langle\sigma_{13}\rangle\right) - 2\gamma_g\langle\sigma_{33}\rangle \\
\partial_t\langle\sigma_{13}\rangle &= \sqrt{\gamma_g}\left(\langle\sigma_{33}\rangle - \langle\sigma_{11}\rangle\right)\alpha(t) - \gamma_g\langle\sigma_{13}\rangle \\
\partial_t\langle\sigma_{31}\rangle &= \sqrt{\gamma_g}\alpha^*(t)\left(\langle\sigma_{33}\rangle - \langle\sigma_{11}\rangle\right) - \gamma_g\langle\sigma_{31}\rangle \\
\partial_t\langle\sigma_{32}\rangle &= -\sqrt{\gamma_g}\alpha^*(t)\langle\sigma_{12}\rangle - \gamma_g\langle\sigma_{32}\rangle \\
\partial_t\langle\sigma_{12}\rangle &= \sqrt{\gamma_g}\langle\sigma_{32}\rangle\alpha(t)
\end{aligned} \tag{B.6}$$

which needs to be solved according to the initial condition of $\langle\sigma_{11}\rangle = 1$. Equation 3.12 in this case changes to the following form:

$$\begin{aligned}
\partial_{t_2}\langle\sigma_{11}(t_2)\,\sigma_{13}(t_1)\rangle &= \sqrt{\gamma_g}\left(\langle\sigma_{31}(t_2)\,\sigma_{13}(t_1)\rangle\,\alpha(t_2) + \alpha^*(t_2)\,\langle\sigma_{13}(t_2)\,\sigma_{13}(t_1)\rangle\right) + \gamma_g\langle\sigma_{33}(t_2)\,\sigma_{13}(t_1)\rangle \\
\partial_{t_2}\langle\sigma_{33}(t_2)\,\sigma_{13}(t_1)\rangle &= -\sqrt{\gamma_g}\left(\langle\sigma_{31}(t_2)\,\sigma_{13}(t_1)\rangle\,\alpha(t_2) + \alpha^*(t_2)\,\langle\sigma_{13}(t_2)\,\sigma_{13}(t_1)\rangle\right) - 2\gamma_g\langle\sigma_{33}(t_2)\,\sigma_{13}(t_1)\rangle \\
\partial_{t_2}\langle\sigma_{13}(t_2)\,\sigma_{13}(t_1)\rangle &= \sqrt{\gamma_g}\left(\langle\sigma_{33}(t_2)\,\sigma_{13}(t_1)\rangle\,\alpha(t_2) - \alpha^*(t_2)\,\langle\sigma_{11}(t_2)\,\sigma_{13}(t_1)\rangle\right) - \gamma_g\langle\sigma_{13}(t_2)\,\sigma_{13}(t_1)\rangle \\
\partial_{t_2}\langle\sigma_{31}(t_2)\,\sigma_{13}(t_1)\rangle &= \sqrt{\gamma_g}\left(\langle\sigma_{33}(t_2)\,\sigma_{13}(t_1)\rangle - \langle\sigma_{11}(t_2)\,\sigma_{13}(t_1)\rangle\right)\alpha^*(t_2) - \gamma_g\langle\sigma_{31}(t_2)\,\sigma_{13}(t_1)\rangle \\
\partial_{t_2}\langle\sigma_{32}(t_2)\,\sigma_{23}(t_1)\rangle &= -\sqrt{\gamma_g}\,\langle\sigma_{12}(t_2)\,\sigma_{23}(t_1)\rangle\,\alpha^*(t_2) - \gamma_g\langle\sigma_{32}(t_2)\,\sigma_{23}(t_1)\rangle \\
\partial_{t_2}\langle\sigma_{12}(t_2)\,\sigma_{23}(t_1)\rangle &= \sqrt{\gamma_g}\,\langle\sigma_{32}(t_2)\,\sigma_{23}(t_1)\rangle\,\alpha(t_2)
\end{aligned} \tag{B.7}$$

The initial conditions will be as follows:

$$\begin{aligned}
\langle\sigma_{32}(t_2)\,\sigma_{23}(t_1)\rangle\big|_{t_2=t_1} &= \langle\sigma_{31}(t_2)\,\sigma_{13}(t_1)\rangle\big|_{t_2=t_1} = \langle\sigma_{33}(t_1)\rangle \\
\langle\sigma_{12}(t_2)\,\sigma_{23}(t_1)\rangle\big|_{t_2=t_1} &= \langle\sigma_{11}(t_2)\,\sigma_{13}(t_1)\rangle\big|_{t_2=t_1} = \langle\sigma_{13}(t_1)\rangle
\end{aligned} \tag{B.8}$$

Solving equation B.7 with the initial conditions given in equation B.8 gives the first correlation terms appearing on the right-hand side of equation 3.8. Also, the other correlation terms appearing in equation 3.8 will be:

$$\begin{aligned}
\left\langle {r_{in}}^{\dagger}(t_2)\,r_{in}(t_1)\right\rangle &= \alpha^*(t_2)\,\alpha(t_1) \\
\left\langle {r_{in}}^{\dagger}(t_2)\,\sigma_{13}(t_1)\right\rangle &= \alpha^*(t_2)\,\langle\sigma_{13}(t_1)\rangle \\
\langle\sigma_{31}(t_2)\,r_{in}(t_1)\rangle &= \langle\sigma_{31}(t_2)\rangle\,\alpha(t_1)
\end{aligned} \tag{B.9}$$

Appendix C

Scattering Matrices for Two and Three Photon Inputs

Using equations 4.9 and 4.10, the scattering matrix elements for the two cases of two- and three-photon inputs can be written as follows:

$$\Sigma_1^2(t_1,t_2;t'_1,t'_2) = \Sigma_1^1(t'_1-t_1)\,\delta(t_2-t'_2)$$
$$\Sigma_2^2(t_1,t_2;t'_1,t'_2) = \Sigma_0^1(t'_1-t_1)\,\Sigma_1^1(t'_2-t_2) - \gamma_g\delta(t_2-t'_1)\exp(\gamma_g(t_1-t'_2))$$
$$\Sigma_0^2(t_1,t_2;t'_1,t'_2) = \Sigma_0^1(t'_1-t_1)\,\Sigma_0^1(t'_2-t_2) - \gamma_g\delta(t_2-t'_1)\exp(\gamma_g(t_1-t'_2))$$
$$\Sigma_1^3(t_1,t_2,t_3;t'_1,t'_2,t'_3) = \Sigma_1^1(t'_1-t_1)\,\delta(t_2-t'_2)\,\delta(t_3-t'_3)$$
$$\Sigma_2^3(t_1,t_2,t_3;t'_1,t'_2,t'_3) = \Sigma_0^1(t'_1-t_1)\,\Sigma_1^1(t'_2-t_2)\,\delta(t_3-t'_3) - \gamma_g\delta(t_2-t'_1)\,\delta(t_3-t'_3)\exp(\gamma_g(t_1-t'_2))$$
$$\begin{aligned}\Sigma_3^3(t_1,t_2,t_3;t'_1,t'_2,t'_3) = {}& \Sigma_0^1(t'_1-t_1)\,\Sigma_0^1(t'_2-t_2)\,\Sigma_1^1(t'_3-t_3) - \gamma_g\delta(t_2-t'_1)\,\Sigma_1^1(t'_3-t_3)\exp(\gamma_g(t_1-t'_2)) \\ & -\gamma_g\Sigma_0^1(t'_1-t_1)\,\delta(t_3-t'_2)\exp(\gamma_g(t_2-t'_3)) - \gamma_g\delta(t_2-t'_1)\,\delta(t_3-t'_2)\exp(\gamma_g(t_1-t'_3))\end{aligned}$$
$$\begin{aligned}\Sigma_0^3(t_1,t_2,t_3;t'_1,t'_2,t'_3) = {}& \Sigma_0^1(t'_1-t_1)\,\Sigma_0^1(t'_2-t_2)\,\Sigma_0^1(t'_3-t_3) - \gamma_g\delta(t_2-t'_1)\,\Sigma_0^1(t'_3-t_3)\exp(\gamma_g(t_1-t'_2)) \\ & -\gamma_g\Sigma_0^1(t'_1-t_1)\,\delta(t_3-t'_2)\exp(\gamma_g(t_2-t'_3)) - \gamma_g\delta(t_2-t'_1)\,\delta(t_3-t'_2)\exp(\gamma_g(t_1-t'_3))\end{aligned}$$